Stability Analysis of a Rapid Mechanical Lifting System for the Vertical Transportation of Polymetallic Nodules

WILLEMIJN MES

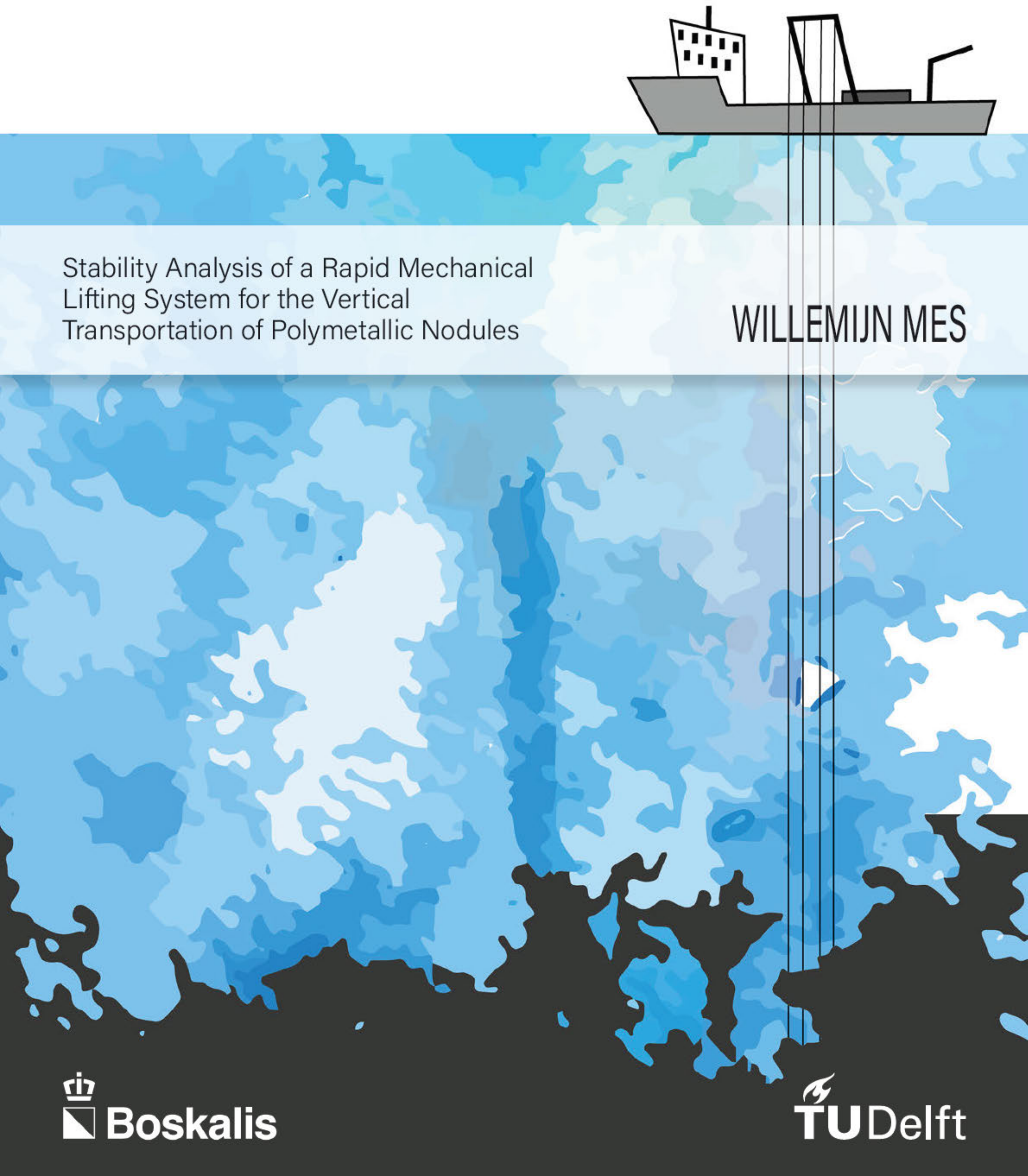

Boskalis

TU Delft

Deep Sea Mining

Stability Analysis of a Rapid Mechanical Lifting System for the Vertical Transportation of Polymetallic Nodules

by Willemijn Mes

to obtain the degree of Master of Science
at the Delft University of Technology

December 3, 2022

Student number:	4470257	
Thesis committee:	Dr. Ir. Rudy Helmons,	TU Delft
	Dr. Ir. Peter Naaijen,	TU Delft
	Dr. Ir. Hayo Hendrikse,	TU Delft
	Prof. Dr. Ir. Cees van Rhee,	TU Delft
	Ir. Remmelt van der Wal,	Royal Boskalis N.V.

Preface

With this thesis ten months of hard work have finished, with only a few moments where I didn't enjoy it. That was partly due to my enthusiasm about the offshore world, but also definitely due to the variation of work throughout my thesis. I started by looking through videos, websites and papers, continued in the hydrolab at Boskalis performing experiments and topped it off by struggling with OpenFOAM. Therefore, a huge thanks to Remmelt and Gertjan, for allowing me to do basically anything during this process. Although the first fifteen minutes of our weekly meetings mostly consisted of discussing last nights news, our discussions really guided me through.

Rudy, I would like to thank you for your guidance and critical mindset, even from 1400 kilometres away. During these months, there were numerous moments where I had no idea where I stood and was in need of some serious feedback. Besides, even on late nights I could count on you emailing me back within minutes.

A special shout out to Florien for designing the cover page and finally, a thank you for myself for my enthusiasm and hard work these months. It is time for a new adventure!

Willemijn Mes
Rotterdam, December 2022

Abstract

Due to urbanisation, improved living standards and electrification, approximately five times more raw minerals are necessary in 2050 compared to 2018. In deep oceans, the seafloor contains these minerals in the form of polymetallic nodules. Nodules are about the size of golf balls that grow throughout the ocean at depths between 3500 m and 6000 m. They contain a wide variety of metals, such as manganese, copper, nickel, cobalt. Nowadays, for large-scale applications, hydraulic lifting is almost exclusively considered for vertical transportation through the water column. However, there is little research available about using other techniques instead. To tackle this knowledge gap, this thesis studies the feasibility of transporting the nodules using a concept of mechanical lifting. The concept used in this thesis consists of two alternating containers that are lowered and hoisted by lifting and guidance wires. Due to the conditions, such as the large depth, the environmental characteristics and the positioning and heading of the vehicles, there are technical uncertainties regarding mechanical lifting. Risks include the yaw rotation of the container, which might result in rope entanglement and wearing of the ropes. This thesis presents a study into the yawing stability of the concept of mechanical lifting for the vertical transportation of polymetallic nodules, which is a crucial factor to operate reliably.

The research question is answered by performing an experimental test and a CFD analysis. The experimental tests include the dynamics of the system while testing various configurations and is validated by an analytical integration in time and a CFD simulation at model scale. The CFD analysis takes away the uncertainties and unknowns: the drag force, the yawing moment and the fluctuation magnitudes and frequencies. The CFD analysis is performed using the open-source software OpenFOAM and simulates multiple configurations. The results of the simulations are compared to the restoring moment by the guidance wires, by transforming the excitation moments into static and dynamic responses of the system. The CFD model is validated by testing the model with a 2D cylinder and 3D sphere, and by performing a mesh convergence study. The CFD simulations are validated by literature.

From the results, it can be concluded that mechanical lifting has high potential. The system can stably be transported at 2 m/s, as the static and dynamic responses are well within the safety limits. The largest response occurs in the middle of the water column, as the rotational stiffness is the smallest at that location. The dynamic response is smaller compared to the static response, as the high frequent fluctuations ($f > 0.075$ Hz) are damped. Rope entanglement will not occur during normal operation at 2 m/s. However, critical situations due to incidental events can arise, including a winch failure, friction or a sudden high current. This has not been evaluated in this research and therefore stability cannot be guaranteed. As lowering at 3 m/s with an inclined system and including the current results in a static maximum yaw rotation larger than the safety limit, the stability cannot be guaranteed for operating at 3 m/s.

Contents

1 Introduction

Research shows that in 2050 about five times more raw minerals are necessary compared to 2018 [1]. This is an enormous increase and that is due to a couple of reasons. The first one is urbanisation, as the global population is and has been rising. Studies show that the population might even rise to 10 billion at its peak in 2060 and thereby the world's building stock might even double [2]. Secondly, the living standards are improving and thus for each person more materials are needed. And finally, the energy transition is a crucial contributor to the demand of raw metals. Every day more transport, households, factories and data centres are moving away from fossil fuels to renewable energy. Manufacturing new lithium-ion batteries, for instance, needs specific metals like nickel and cobalt, and for part of these metals, no recovery or recycling is possible [3]. A second example is the manufacturing of electrical equipment, where copper is an important component. Nowadays, these metals are found in mines in mostly Africa, Indonesia and Australia. The working conditions are terribly rough, as they have to dig deeper and deeper. Besides, the production costs of mining in those areas is increasing.

There is an opportunity. In deep oceans, the seafloor contains these minerals in the form of polymetallic nodules. Nodules are about the size of a golf ball that grow throughout the ocean at depths between 3500 and 6000 m and contain a wide variety of metals, such as manganese, copper, nickel, cobalt [4]. The growth rate of the nodules is low, about the order of millimetres to tenths of millimetres per million years [5]. Its existence has already been known since the 1860s [4]. However, exploitation was more difficult than imagined and thus it was not given any serious attention until the 1960s [4]. By then an American geologist, named John L. Mero, published a book where he explained that the seabed can bring a major supply of minerals [6]. However, shortly after, the metal prices collapsed and the interest decreased [4]. Nowadays, due to the drivers mentioned above, the interest in commercial exploitation of the nodules has renewed. The nodules sit on the surface of the seabed, as buried nodules are rare [7]. An overview of the locations of the nodules is presented in Figure 1.1. The areas with most commercial interest are the Clarion Clipperton Zone and the Penrhyn Basin in the Pacific, due to their high abundance.

As a presentation by GSR [2] pointed out, there is a paradox. Nowadays, due to climate change, biodiversity loss is an important topic of many discussions. The step the world is taking against climate change is electrification and thus deep sea mining might become essential. However, the deep seas are one of the few areas still untouched by humankind and thus an objection to deep sea mining exists. That objection is biodiversity loss, which is exactly what we are trying to avoid. This shows that to be able to make deep sea mining commercial, the uncertainties in the environmental impact must be proven to be low enough. This needs to be done to the International Seabed Authority, which is a UN organisation that holds the regulations and procedures in international waters. That is a challenge.

Technical uncertainties are present as well. The first one has to do with the location. Deep sea mining of polymetallic nodules happens at depths of 3500 m to 6000 m. The depth causes differences in environmental characteristics, such as hydrostatic pressure, temperature, density and salinity. Likewise, the

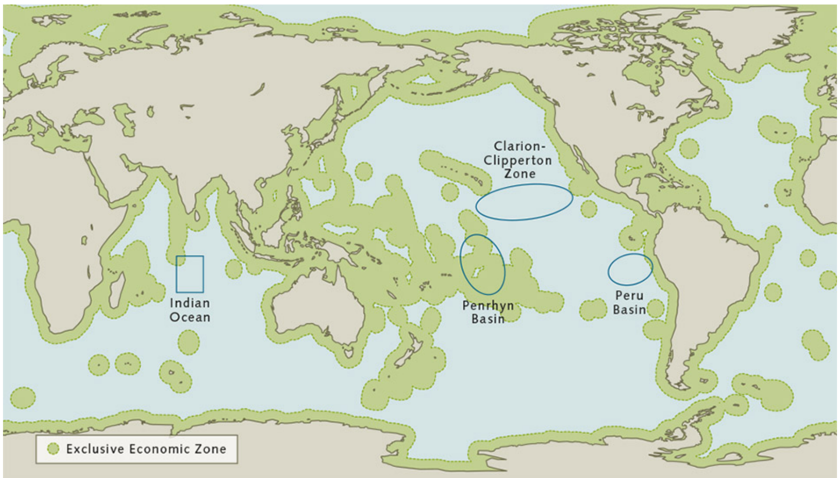

Figure 1.1: Locations of polymetallic nodule fields [8].

seabed is different. At such large depths the seabed is extremely soft, which is crucial in the design of the underwater collector vehicle. Also, the positioning and heading of the vehicle become difficult and challenges arise considering the vertical transport system. The nodules have to be transported through the water column over a distance of six kilometres. How do you know what the vehicle is doing at 6000 m underwater? What if there is a failure and you are not able to hoist the vehicle? Therefore, designing on robustness and reliability becomes highly important and knowing exactly what the system is capable of, is a must.

Various companies and organisations are researching possibilities for a concept and some are already executing tests and exploration missions. For large-scale applications, hydraulic transport is almost exclusively considered nowadays for the vertical transportation of the nodules. However, hydraulic lifting has a lot of technical difficulties and uncertainties and there is limited research available about using other techniques instead. Therefore, more research needs to be done to understand what technique is most reliable. This thesis is a feasibility study of transporting the nodules using mechanical lifting.

1.1. Concept introduction

[redacted]

- Reliability/Robustness: In mechanical lifting most power components are located at the vessel, causing for more easy repairs and maintenance work. Besides, the underwater system can be more easily hoisted to the vessel in the case of failure. If a repair must be performed underwater, a mining operation could be put on hold for days, maybe even weeks.

- Environmental impact: Commercial deep sea mining can only take place if the environmental impact is proven to be low enough. Lowering the impact is done by reducing spillage and the sediment plumes as much as possible. Mechanical lifting, compared to for instance hydraulic lifting, could reduce the returning sediment plume and decrease the underwater noise.

- Proven concepts: An integrated system that is based on proven concepts has a higher chance of succeeding. Technologies and developments from the dredging and salvage industry are used in the concept of mechanical lifting, which is the expertise of Boskalis.

[redacted]

[redacted]

[redacted]

Due to the conditions in which deep sea mining takes place, there are some major technical uncertainties regarding mechanical lifting. The risk of the transportation system is rotation of the container, which might result in rope entanglement and wearing of the rope. Boskalis introduced a cursor frame attached to the container to guide all ropes during transportation. A schematic overview of what the container with cursor frame looks like is given in Figure 1.3. Red indicates the guidance wires and blue indicates the lifting wires. The cursor frame is open on one side, as shown in Figure 1.3a, as this is required by the design of the docking unit to fill the container with nodules.

1.2. Research questions

This research will focus on the stability and excitation of the vertical transportation system, which is a crucial factor in the system to operate reliably. The research question and sub-questions for this thesis are presented below.

Can the combined system of the container and the cursor frame, for the vertical transportation of poly-metallic nodules by means of mechanical lifting, stably be transported?

1. What are the geometrical parameters and hydrodynamic characteristics of the system?
2. Using the site's specifications, what are the phenomena that are deemed most critical during transportation, due to the lifting system and the environment at the sites?

3. Based on the state of the art, what modelling techniques are available and which is/are most suitable for this research?

4. What are the forces and moments on the system during hoisting and lowering and how are they fluctuating?

5. Can the stability of the combined system during vertical transportation be assured, meaning without rope entanglement or extensive yawing of the container?

[redacted]

Figure 1.3: Schematic overview of the top view (a) and the side view (b) of the concept with the guidance wires in red and the lifting wires in blue.

1.3. Approach

An overview of the structure of this thesis is shown in Figure 1.4, where each box signifies a chapter. A blue box indicates an analysis and the arrows indicate what the chapter is based on. The first two sub-questions of this research are answered in the concept introduction in Chapter 2 and in the analytical analysis in Chapter 3. The concept introduction presents a detailed description of the concept of the vertical transport system used in this thesis. Besides, it includes the site's specifications, and the scope of this thesis. The analytical analysis gives an overview of the phenomena, in which first the restoring moment due to the guidance wires is discussed and further on the yawing moment due to the external forces, divided into a mean yawing moment and fluctuations. Thereafter, the methodology is presented in Chapter 4. The methodology answers sub-question three. It describes the modelling techniques most suitable for this research. Defining the methodology is based on the uncertainties and unknowns found in the analytical analysis and on public research on similar research problems.

The fourth sub-question is answered by two separate analyses that can be placed in parallel: The experimental test in Chapter 5 and the computational fluid dynamics (CFD) analysis in Chapter 6. The two analyses combined make the results of this thesis. In Chapter 5, the experimental test, the scaling effects are discussed and the parameters are defined. Various configurations are tested and the results with validation are presented. Chapter 6 on the CFD analysis presents the structure and details of the CFD model and the result of various simulations. The analytical analysis is used to validate the result of the CFD analysis. Thereafter, the discussion is presented in Chapter 7, including a CFD simulation of the experimental test, an overview of the static and dynamic response of the system and a calculation into the energy consumption of the vertical transport system. The conclusion is presented in Chapter 8, where the final research question is answered. The recommendations for future research are stated in Chapter 9.

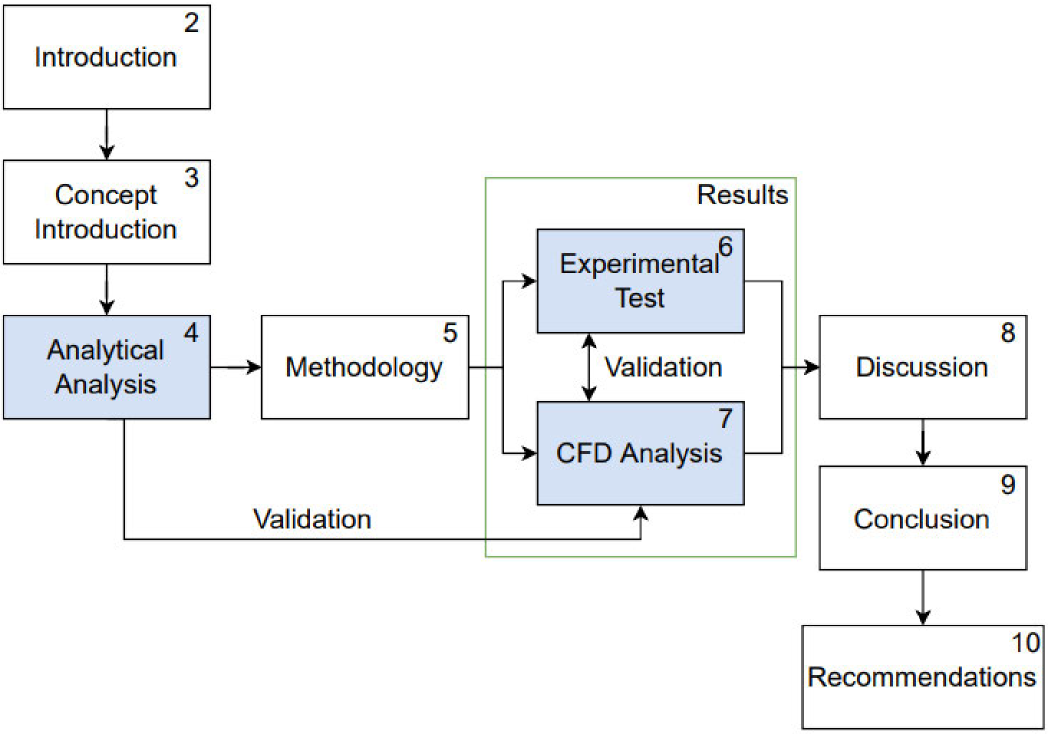

Figure 1.4: Flow chart of the structure in this thesis.

2
Concept introduction

2.1. Concept description

As shown in Figure 1.2a, the concept can be divided into three systems: The seafloor production tool, which is located at the seafloor and collects the nodules, the vertical transport system, which transports the nodules from the seafloor to the sea surface, and the production support vessel, which takes in the nodules and from where all sub-sea operations are run.

[redacted]

[redacted]

[redacted]

[redacted]

[redacted]

[redacted]

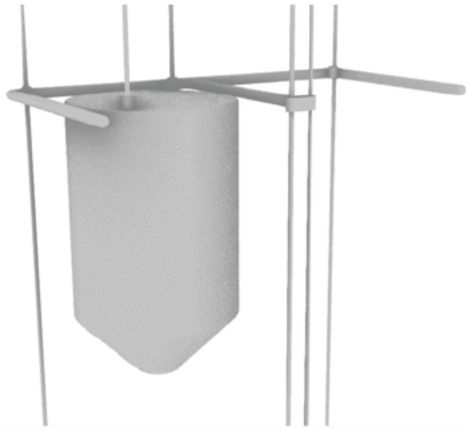

[redacted]

[redacted]

[redacted]

[redacted]

[redacted]

[redacted]

2.2. Site specifications

This research focuses on two locations for mining polymetallic nodules: The Penrhyn Basin and the Clarion Clipperton Zone (CCZ). As presented in Figure 1.1, the CCZ is located between Mexico and Hawaii and the Penrhyn Basin is located in the exclusive economical zone of the Cook Islands. These locations have most commercial interest, as the high abundance of nodules is high and sea floor flat [7]. An overview of the abundance variability is given in Figure 2.4.

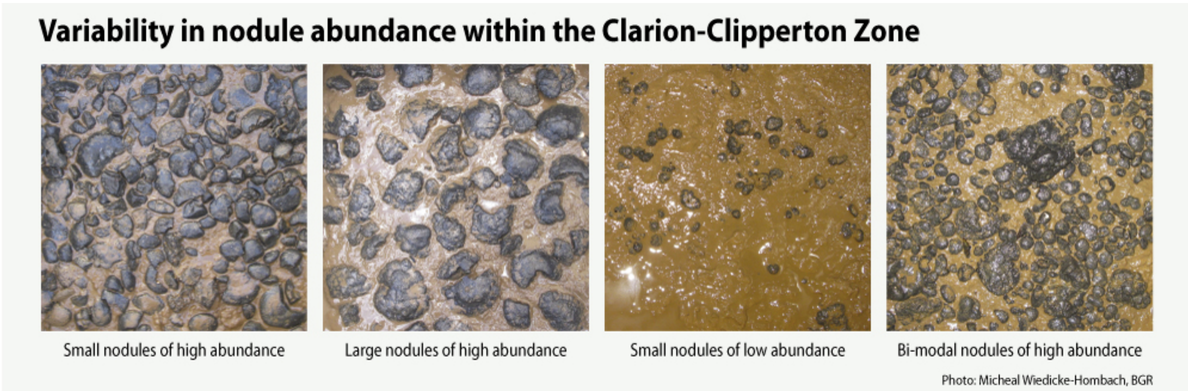

Figure 2.4: Overview of the variety of nodule abundances [11].

The CCZ is a region of about 6 million km^2 in the Pacific Ocean with depths between 4000 and 5500 m. The Penrhyn Basin lies within the 200 nautical miles of the exclusive economical zone of the Cook Islands. More than half is ultra-deepwater, 4500 to 5500 m, with polymetallic nodules on the seabed [7]. The cobalt content in the Penrhyn Basin is approximately 0.43 %, high for polymetallic nodules [7]. The specifications of the sites are listed in Table 2.2, with their references in Appendix C.

Table 2.2: Summary site specifications for the CCZ and the Penrhyn Basin.

	CCZ	Penrhyn Basin	Ref. Appendix C
Temperature at d* = -2750 m	1.6 °C	1.6 °C	Figure C.1a
Temperature at d = -5500 m	1.1 - 1.2 °C	0.95 °C	Figure C.1b
Salinity at d = -2750 m	34.7 g/kg	34.7 g/kg	Figure C.2
Density	1025 kg/m^3	1025 kg/m^3	Figure C.3a
Kinematic viscosity	$1.76E^{-6}$ m^2/s	$1.76E^{-6}$ m^2/s	Figure C.3b
Current at -5500 < d < -1000 m	0.1 m/s	0.1 m/s	Figure C.4 and C.6
Current at d = -200 m	0.2 m/s	0.2 m/s	Figure C.4 and C.6
Current direction	all	all	Figure C.5 and C.7

*d is the depth [m]

As noted in Chapter 1, the environmental impact is crucial to commercialise deep sea mining. Biodiversity loss and habitat destruction are a serious showstopper as the sediment plume is predicted to spread several kilometres beyond the mining area [12]. However, there are other impacts present as well, in the form of temperature changes, noise, vibrations and light [13], emissions (surface en bulk carrier vessels) [13], oxidation reactions forming sulphuric acid [13], compaction of the seabed [12] and biodiversity loss and habitat destruction [12].

2.3. Scope

The scope of this research is defined by the following elements:

1. **Container and cursor frame:** The yawing stability of the container and cursor frame is investigated for transporting with a velocity of 2 and 3 m/s. During lowering, the container is empty and thus the system is more sensitive to forces and moments compared to full, due to the lower tension in the lifting wires, higher pitch and roll angles and lower inertia. However, the full container is investigated as well, as the shape of the system is different.

2. [redacted]

3. **Stability limit:** As a limit, the system is considered safe when yaw rotations larger than 45° do not occur.

Left out of the scope of this research are the following elements:

1. **Positioning:** The vessel is assumed to be located directly above the docking unit due to the dynamic positioning system. However, it could be beneficial to change the location of the vessel to more forwards or backwards. This is something further to investigate, which is not part of this research. The positioning of the docking unit can be maintained due to thrusters and automatic tension adjustment systems that are placed at the docking unit.

2. **Splash Zone:** In scope of this thesis, the system is hoisted and lowered in the region below the splash zone. Therefore, forces due to the splash zone and lifting the system above sea level are not considered.

3. **Fatigue and wearing:** This research is a feasibility study for the use of mechanical lifting. Fatigue and wearing are considered important components in the developments. However, in this study the fatigue and wearing are assumed to be low enough to remain in the elastic regime for the hardware and are therefore not included in the scope.

4. **Control engineering and surveying:** Control engineering is not part of this research and is assumed to be available and operable. This includes measuring the location of the docking unit and the container, measuring and adjusting the tension in the lifting and guidance wires, measuring and adjusting the heading of the docking unit and vessel, and more. The umbilical acts differently compared to the lifting and guidance wires as there is no pretension. Yaw rotations of the container combined with swaying of the umbilical can lead to rope entanglement and is therefore a serious risk. However, the behaviour of the umbilical is not included in the scope of this thesis.

2.4. Coordinate system

For the translations and rotations, a vessels coordinate system is used. This is shown in Figure 2.5, where the arrows indicate the positive directions. All angles are defined clockwise.

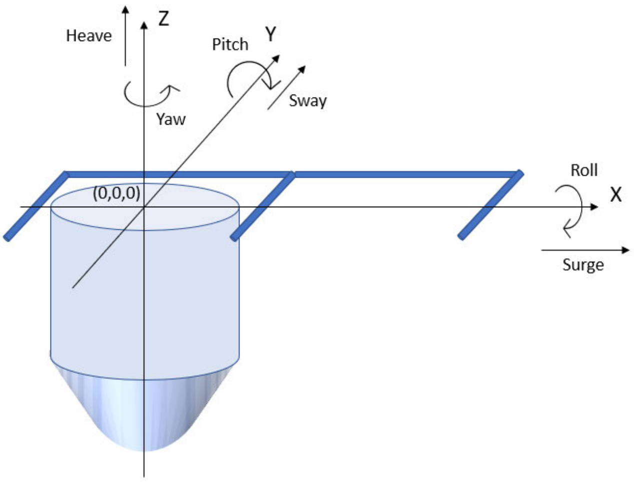

Figure 2.5: Coordinate system.

3
Analytical analysis

The first step to determine and understand the phenomena and get an estimation of the forces and moments acting on the container and cursor frame, is to perform an analytical analysis. The analysis is divided into two parts: the restoring moment due to the ropes and the yawing moment due to the external forces acting on the system. The restoring moment is induced by the guidance and lifting wires, which is dependent on the depth and the yaw rotation. The yawing moment is split into the mean yawing moment and fluctuations. The mean yawing moment is induced by drag, the current and torsion in the lifting wires. The self-weight of the container and cursor frame have an effect on the drag and current, as it can tilt the system. The fluctuations in the yawing moment are caused by vortex shedding. In addition incidental events are discussed. An overview of the analytical analysis is summarised in Figure 3.1. The blue blocks are discussed in the next sections.

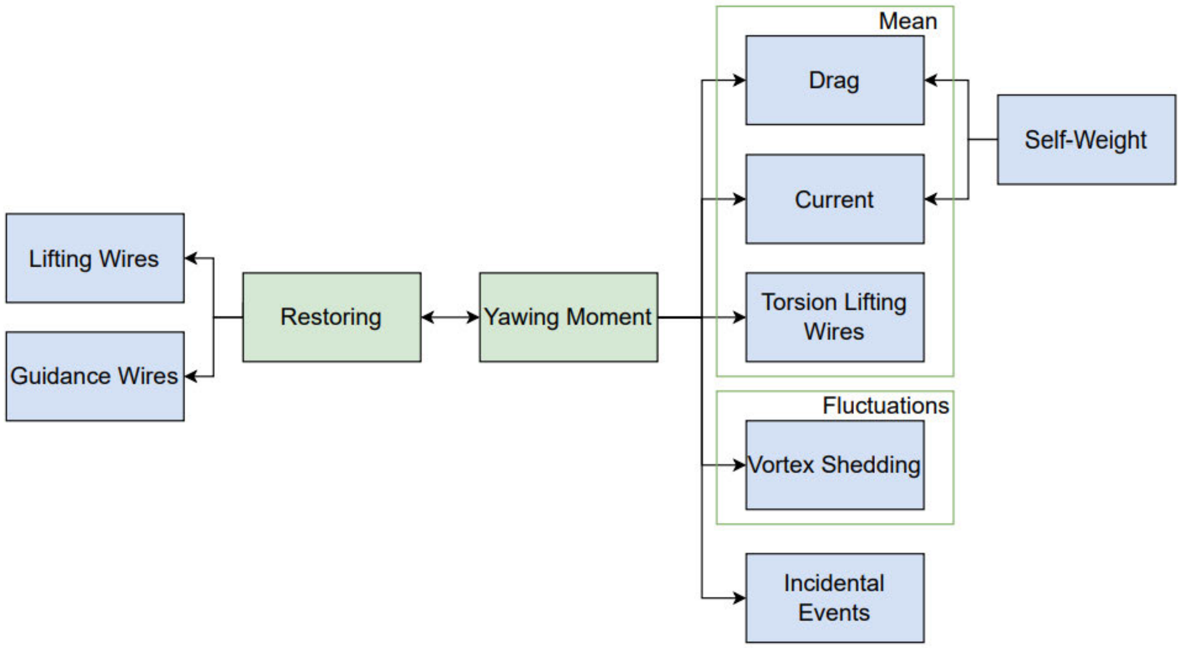

Figure 3.1: Overview of the analytical analysis.

3.1. Restoring force and moment

The moving system induces restoring forces and a corresponding restoring moment by the tension in the lifting and guidance wires. The magnitude depends on the offset, as shown in Figure 3.2a. An example is given in Figure 3.2b: a rotation of 45°, a translation in the X-direction of 5 m and in the Y-direction of 6 m. *S1* to *S4* are the locations of the guidance wires and *L1* and *L2* are the locations of the lifting wires of the container. The restoring force is calculated using the tension in the wires. For the guidance wires, the tension is the submerged mass of the docking unit. The lifting wires are tensioned by the mass of the container and cursor itself and make for a restoring force only upwards, as the wires end at the container.

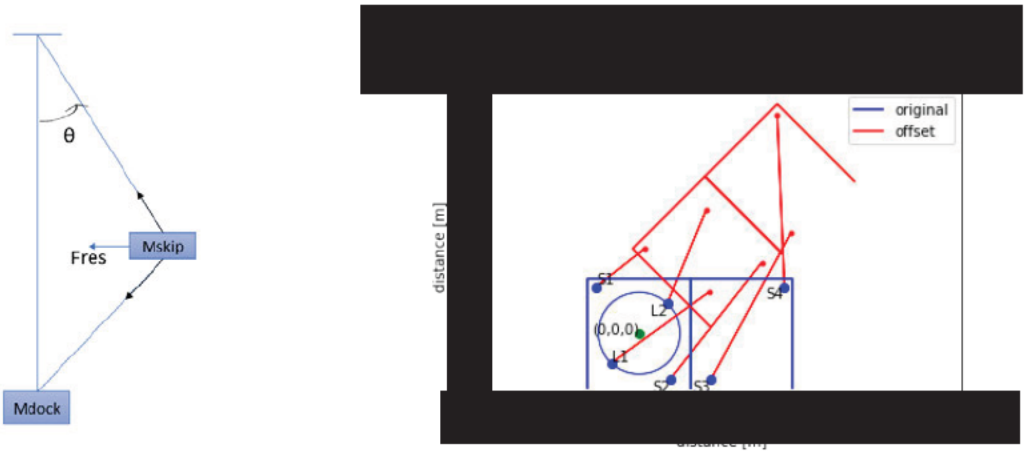

(a) (b)

Figure 3.2: Schematic overview of the restoring force due to an offset of the system (a) and an example offset (b).

The restoring moment depends on the location of the system and the yaw rotation. Figure 3.3a presents the dependency on the depth, for the example situation in Figure 3.2b. The closer the system is to the docking unit or vessel, the larger the restoring moment. The lifting wires have little effect on the restoring moment compared to the guidance wires, which can be seen in the figure, and are therefore neglected in the remainder of this thesis. Figure 3.2b presents the dependency on yaw rotations of the system at different depths for zero translation. At larger rotations, the offset increases and thus the restoring moment increases. However, there is a turning point, where the rotation is too large and the restoring moment decreases. Figure 3.2b shows that the maximum restoring moment occurs at 90°. When the excitation moment is larger than the maximum restoring moment at 90°, the system will rotate even further and the ropes might entangle.

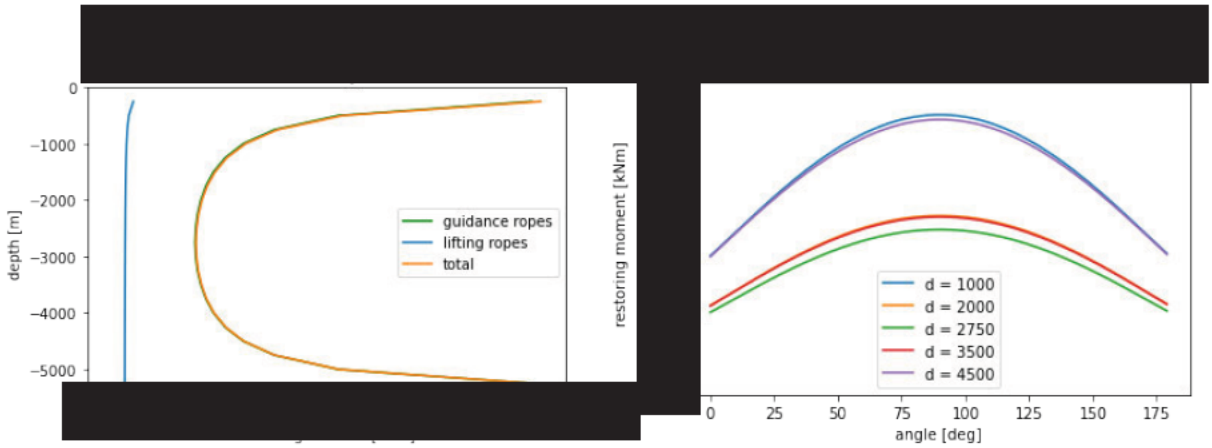

(a) (b)

Figure 3.3: The dependency of the restoring moment on the depth (a) and the yaw rotation (b).

To examine the response of the system, an increasing yawing moment [redacted]) is exerted on the system at a depth of -2750 m. Yaw rotation, X-translation and Y-translation are variables. The system finds a new equilibrium state for each yawing moment, as shown in Figure 3.4a, where the static response of the system is shown for the increasing yawing moments. The system rotates around the centre of the cursor frame. The yaw rotation as a function of the yawing moment is plotted in Figure 3.4b.

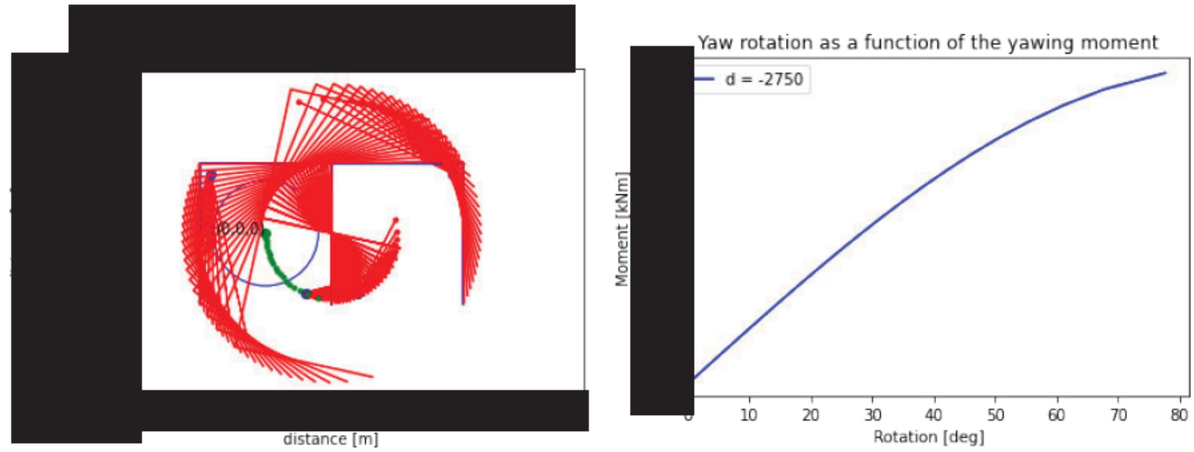

(a) (b)

Figure 3.4: The response of the system at the increasing moment (a) and the corresponding rotation for each moment (b).

The restoring moment and rotational stiffness as a function of the depth for a yaw rotation of 20° and 45° are plotted in Figure 3.5a and 3.5b. In the middle of the water column at -2750 m, the restoring moment at 45°, the safety limit, is [redacted] The rotational stiffness at that location is [redacted]

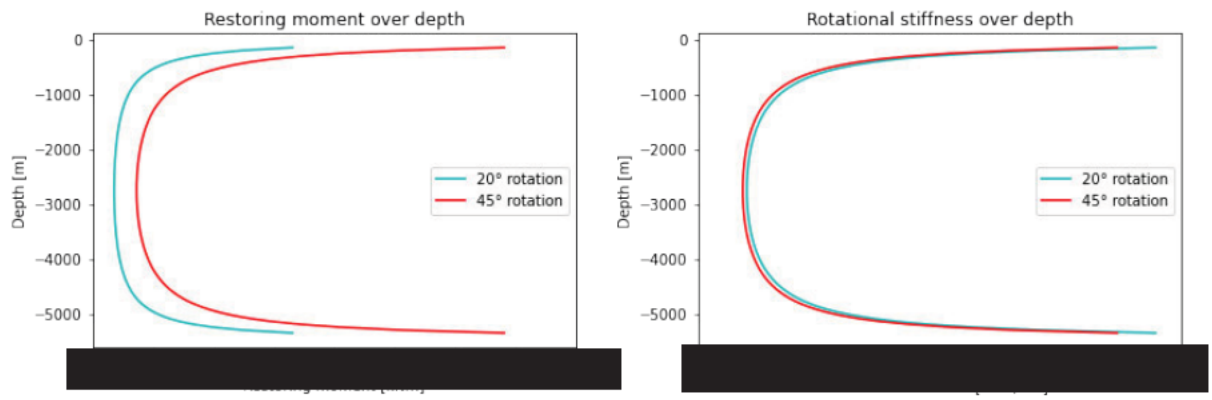

(a) (b)

Figure 3.5: The restoring moment (a) and the rotational stiffness (b) over the depth for a yaw rotation of 20° and 45° respectively.

3.2. Self-weight

The container and cursor can be split into 6 parts: 5 pipes and the container as shown in Figure 3.6. The submerged weights of the parts, taken from Appendix A, are presented in Table 3.1.

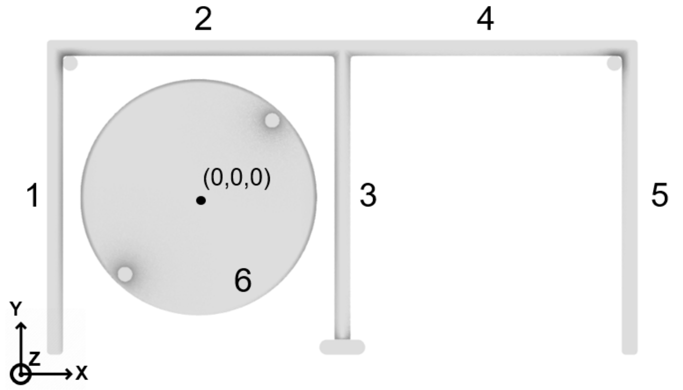

Figure 3.6: Numbering of the parts for further calculations.

Table 3.1: Submerged weight of the parts.

[redacted]

The centre of gravity of the container [redacted] as calculated in Appendix E.1. The location of the centre of gravity of the container and cursor combined, full and empty, with respect to the lifting point in (0, 0, 0), are shown in Table 3.2. For the full container, uncertainty in the centre of gravity is present, as the nodules could be unevenly distributed.

Table 3.2: Distance of the centre of gravity to the lifting point for different situations.

[redacted]

3.2.1. Mass moment of inertia

The mass moments inertia of the system, with and without added mass, are summarised in Table 3.3. These values represent the mass moments of inertia of the empty container and are calculated as the sum of the mass moments of inertia for each body by

$$I = \sum (I_G + m \cdot d^2), \tag{3.1}$$

with
I_g as the mass moment of inertia through the centroid G of the body [kgm^2],
d as the distance between the centroid of the body and the axis [m],
m as the mass of the body [kg].

The calculations can be found in Appendix E.6 and E.7.

Table 3.3: Mass moment of inertia (MOI) with and without the added mass incorporated.

[redacted]

3.2.2. Eigenperiod

With the added mass incorporated in the inertia, the eigenfrequency of the system can be calculated by

$$\omega_n(d) = \sqrt{\frac{K_{rot}(d)}{I_z}}, \tag{3.2}$$

with
$\omega_n(d)$ as the eigenfrequency as a function of the depth [rad/s],
$K_{rot}(d)$ as the rotational stiffness around the Z-axis as a function of the depth [Nm/rad],
I_z as the mass moment of inertia around the Z-axis [kgm^2].

The eigenfrequency and corresponding eigenperiod are shown in Figure 3.7. The eigenperiod is calculated by dividing 2π by the eigenfrequency. At a depth of -2750 m and a yaw rotation of 45°, the eigenperiod is 32 s.

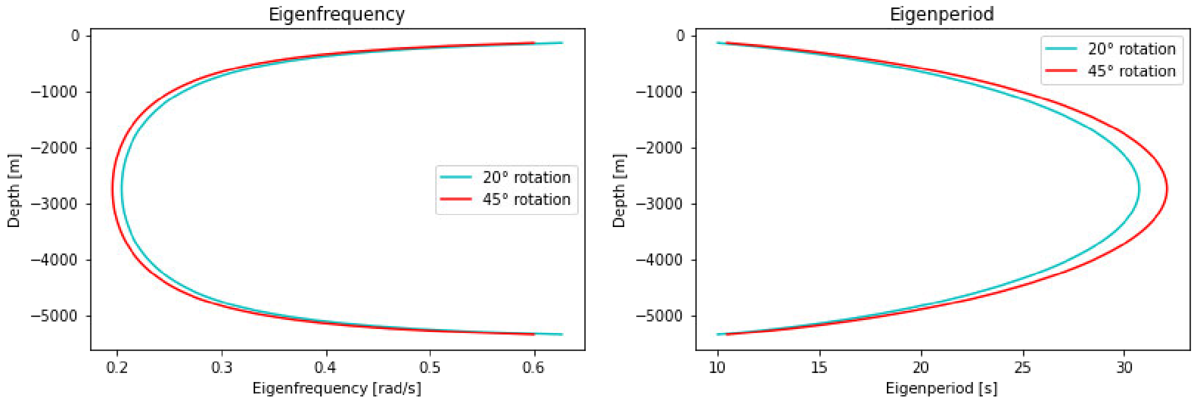

(a) (b)

Figure 3.7: The eigenfrequency (a) and the eigenperiod (b) over the depth for a yaw rotation of 20° and 45° respectively.

3.3. Drag

During operation, the system is experiencing drag forces. This is shown in Figure 3.8, with Figure 3.8a the lowering operation and Figure 3.8b the hoisting operation. The orange arrows indicate the drag forces, the green arrows indicate the submerged weights and the yellow arrow is the lifting force. The drag force is calculated by

$$F_d = \frac{1}{2} \cdot C_d \cdot A \cdot \rho \cdot U^2, \tag{3.3}$$

with
C_d as the drag coefficient of the object [-],

A as the reference area [m^2],
ρ as the density of the fluid [kg/m^3],
U as the flow velocity relative to the object [m/s].

This is an approximation, as it assumes a uniform flow in 1D and does not consider disturbances between the parts of the system. Besides, the coefficients for the shape of the system are approximated as they are not available in literature.

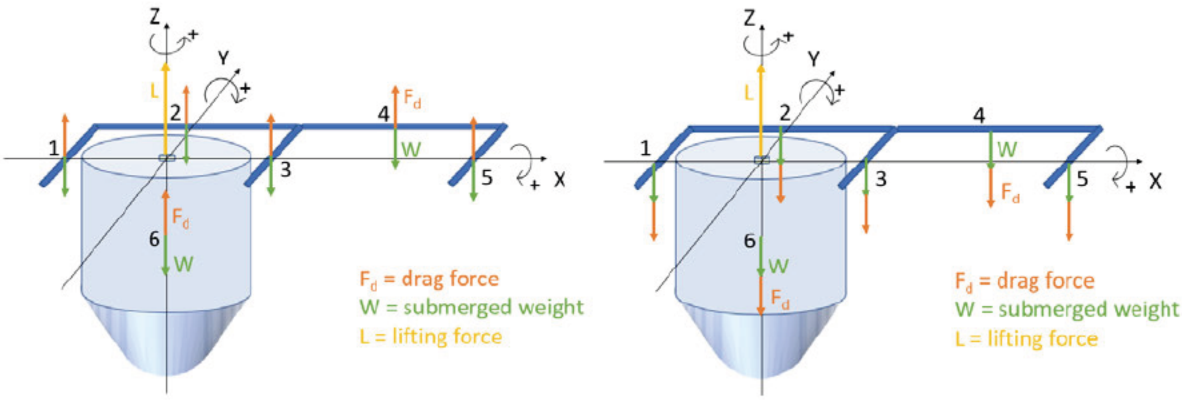

(a) (b)

Figure 3.8: Forces acting on the container and cursor frame during lowering (a) and hoisting (b) due to self-weight, drag and lifting.

The drag coefficient C_d depends on the shape and the Reynolds number. The Reynolds number is given by

$$\mathrm{Re} = \frac{UL}{\nu}, \tag{3.4}$$

with
U as the flow velocity [m/s],
L as the characteristic length [m],
$\nu = \frac{\mu}{\rho}$ as the kinematic viscosity [m^2/s].

The Reynolds numbers and drag coefficients are defined in Appendix E.2 and summarised in Table 3.4.

Table 3.4: Reynolds number and drag coefficient of the container and cursor at 2 and 3 m/s.

[redacted]

The cross-sectional area is the projected frontal area of the body. The relative velocity is the lowering and hoisting speed as these values are defined for a uniform flow. The drag force is calculated and summarised in Table 3.5. Lifting force L, the force due to the lifting wires, can be calculated by taking a balance of forces in Z-direction: $L = \sum W_{1-6} \cdot g - \sum F_{d,1-6}$, with $g = 9.81\ m/s^2$.

The rotations due to the drag forces and the self-weight of the system, are calculated. The rotation is split into three rotation angles: roll is α, pitch is β and yaw γ. The rotations are calculated by taking the

Table 3.5: Calculation of the drag force per part during lowering (+) and hoisting (-).

[redacted]

balance of moments around the lifting point, for the X, Y and Z-axis respectively. The calculation can be found in Appendix E.3 and E.4. The results for lowering are shown in the Table 3.6 and hoisting in Table 3.7.

[redacted]

Hoisting an empty container is not a situation in the production cycle and is therefore an incidental situation. The hoisting velocity could be lowered to avoid large roll and pitch rotations.

3.4. Current

As presented in the site characteristics in Chapter 2.2, there is a current acting on the system. The maximum expected current in the middle of the water column at -2750 m is 0.1 m/s and from -1000 m to the sea surface, the current can increase to 0.6 m/s. The current can act from varying directions. The force due to the current is estimated by assuming a uniform 1D flow with $Fc = \frac{1}{2} \cdot C_d \cdot A \cdot \rho \cdot U^2$.

The response of the system can be estimated by a balance of forces in X- and Y- directions and a balance of moments around the Z-axis, including the current and restoring. The system of equations, as shown in Appendix E.5, can be solved for a specific current velocity, direction and depth of where the system is located. Figure 3.9a shows the result for a current velocity of 0.1 m/s from 180° at a depth of -2750 m. Figure 3.9b shows the result for a current velocity of 0.2 m/s from 0° at a depth of -200 m.

[redacted]

[redacted]

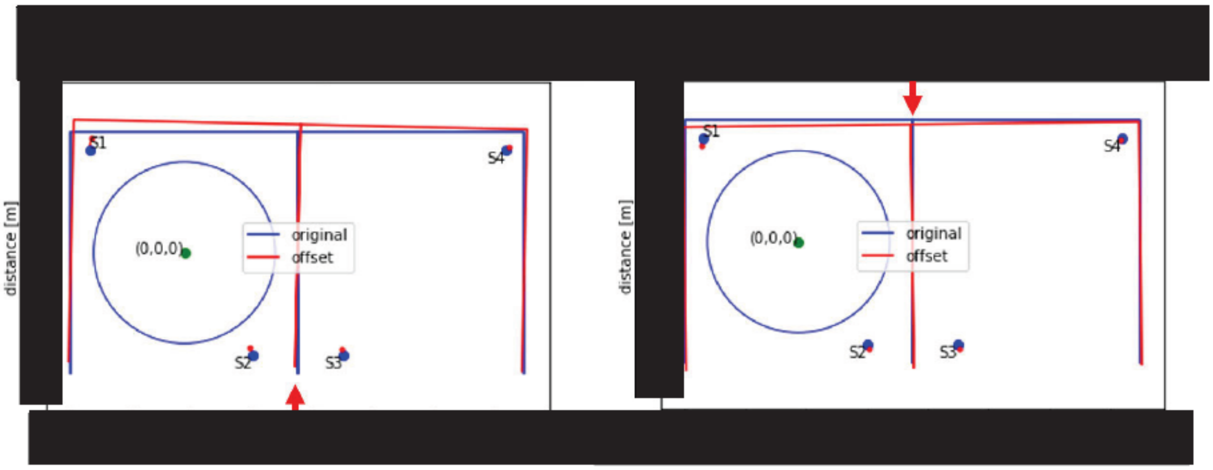

[redacted]a) (b)

Figure 3.9: Excitation due to a current with a velocity of 0.1 m/s from 180° at -2750 m depth (a) and a velocity of 0.2 m/s from 0° at -200 m depth (b).

3.5. Forward velocity

The response of the container and cursor frame due to the forward velocity of the mining head and the vessel can be calculated in the same manner as the current. The forward velocity is 0.1 m/s as shown in the concept parameters in Chapter 2. The response of the system at a depth of -2750 m is shown in Figure 3.10a.

[redacted]

(a) (b)

Figure 3.10: Excitation due to the forward velocity of 0.1 m/s from 90° at -2750 m depth (a) the response of the forward velocity combined with the current resulting in 0.2 m/s from 90° at -2750 m depth (b).

When the direction of the forces due to the current is equal to the direction of the forces due to the forward velocity, the relative velocity at -2750 m increases to 0.2 m/s. The response of the container and cursor frame for this situation is shown in Figure 3.10b.

[redacted]

3.7. Vortex shedding

The flow patterns for a flow around a cylinder are shown in Figure 3.12. Table 3.4 shows that the Reynolds number for the cursor frame lies between 4.55E+05 and 6.82E+05, for transporting between 2 and 3 m/s. This corresponds to the middle pattern in Figure 3.12, the critical flow regime, where the wake is disorganised and no clear vortex street is apparent. However, as the flow velocity at the cursor could decrease due to the container being present, a vortex street could develop.

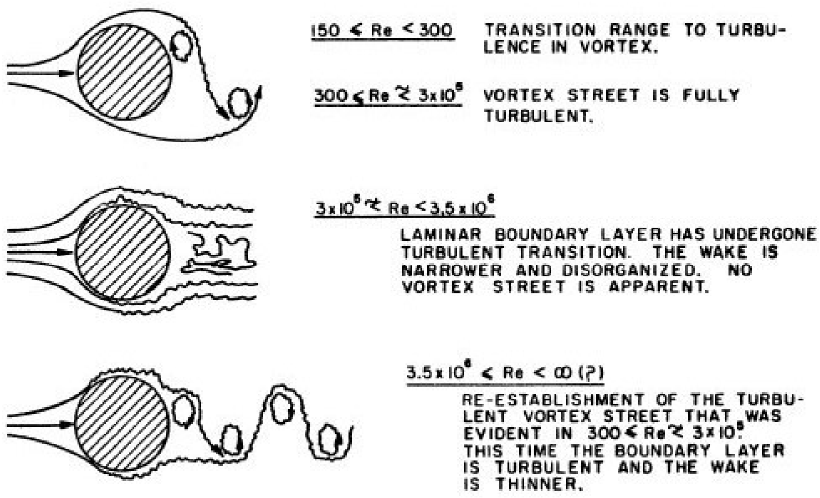

Figure 3.12: The flow regimes for a cylinder dependent on the Reynolds number [17].

The Reynolds number for the container is between 6.82E+06 and 1.02E+07, for transporting between 2 and 3 m/s. Comparing to the flow around a sphere for the same Reynolds numbers, gives the rightmost flow in Figure 3.13. A fully turbulent disorganised wake is developed.

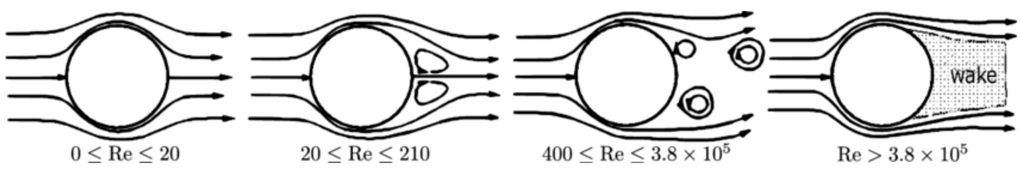

Figure 3.13: The flow regimes for a sphere dependent on the Reynolds number [18].

3.7.1. Vortex induced vibrations

Vortex shedding can induce vortex-induced vibrations when the flow on a body develops vortex shedding at or near the structural natural frequency of the body. The lock-in phenomenon can occur and large vibrations arise. Vortex-induced vibrations are an important design issue in particular for areas with a large depth, such as risers, as the large height lowers the natural frequency of a structure and thus lowers the magnitude of the current required to induce vortex-induced vibrations [19]. Although the current at Penrhyn Basin and the Clarion Clipperton Zone is low (0.1 m/s), the hoisting and lowering operation does create a high relative velocity (2 to 3 m/s). The natural frequency of the container and cursor frame changes over the depth as shown in Figure 3.7a and therefore operating at or near the natural frequency somewhere along the water column is a possibility.

3.7.2. Strouhal number

An important parameter in vortex shedding is the Strouhal number, which describes the oscillation in the flow. The Strouhal number can be calculated by

$$St = \frac{f_w D}{U}, \quad f_w = \frac{St \cdot U}{D}, \tag{3.6}$$

with
f_w as the vortex shedding frequency [Hz],
D as the projected width normal to the flow direction [m],
U as the relative flow velocity [m/s].

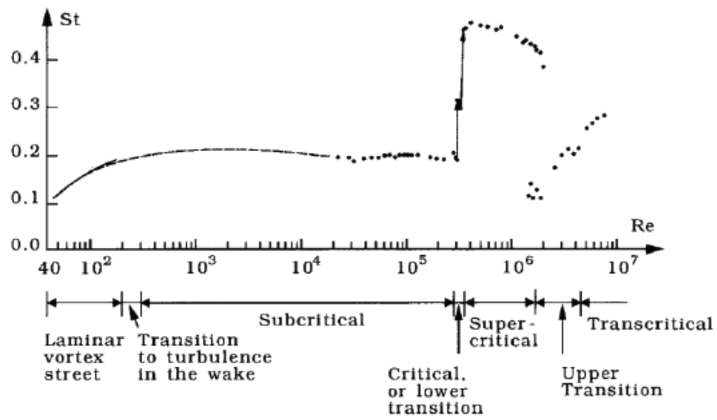

Figure 3.14: Relation between the Strouhal number and the Reynolds number for a smooth cylinder [20].

[redacted]

During hoisting, it is expected that the frequency of the fluctuations at the cursor frame exist at the container as well, due to the vortices developed disturbing the flow around the container. However, the parts of the cursor do not necessarily shed vortices in phase and therefore the frequencies can differ. During lowering, the frequency of vortex shedding at the cursor frame does not necessarily match the container, as the flow reaches the container first.

3.8. Incidental events

An incidental event is for instance a sudden high current, friction in one of the ropes or a lifting or winch failure. The incidental event could dislocate the system of the container and cursor frame, which must stabilise itself to be able hoist. Another event is an uneven distribution of the nodules in the container. The centre of gravity shifts, which could tilt the system and be disadvantageous for the yaw stability.

4
Methodology

The question is whether the restoring moment by the guidance wires is large enough to account for the yawing moment acting on the system while hoisting and lowering through the water column. The analytical analysis in Chapter 3 is accompanied with uncertainties. Firstly, because the calculations approximate the shape of the system. Secondly, the simplified calculations do not include interaction between the parts of the system and finally, dynamics are not yet considered. Therefore, the modelling technique(s) should give answers to the following questions:

1. What is the drag on the system?
2. What is the yawing moment induced by the vertical transportation and/or current?
3. What are the fluctuations in the yawing moment?

The topic of this research is a fluid-structure interaction problem. This is the field where fluid dynamics and solid dynamics come together. These problems can be solved by using computational methods or analytical expressions. However, analytical expressions have simplifications, such as a limited flow and solid deformation regime, only linear phenomena and simple geometries [21]. Therefore, it cannot include large structure deformations and turbulence, which computational methods can [21].

4.1. Other fields

Little public research is available about the research problem and thus an overview of other fields that offer literature on similar problems is given. This includes modelling of load-lifting mechanisms, riser dynamics, hydrodynamic characteristics of a remotely operated vehicle and modelling of mooring systems.

4.1.1. Modelling of load-lifting mechanisms

The vertical transport system shows similarities to load-lifting mechanisms, which are usually modelled as mass-spring-dashpot systems. An example is a dynamic model for crane lifting with multiple degrees of freedom [22]. A second example is the dynamic model for an elevator. An elevator is guided during lifting and lowering. The dominant influences on the dynamic behaviour are the elements' masses, the rope stiffness and the driving mechanism characteristics [23]. In elevators with great heights and high velocities, the stiffness drastically changes, which is the case for the transportation system of this thesis as well. The differential equations for this problem are described by Vladic et al. (2011) [23].

4.1.2. Riser dynamics

In Chapter 3, vortex shedding has been introduced as a phenomenon that can induce periodic forces on the system. Literature exists on vortex-induced vibrations in riser dynamics. A riser is usually modelled as an Euler-Bernoulli beam, which vibrates due to waves, currents and vessel movements [24]. The deflections are lateral, transverse and axial, all dependent on position and time. For risers with large depths, the ocean current is the main cause of damage by vortex induced vibrations, as it acts over the entire length [25]. The important contributions when modelling a riser can be divided into four areas: the hydrodynamic force [26, 27], lateral vibrations [28, 29, 30], transverse or vortex-induced vibrations [31, 32, 33] and multi-dimensional riser models [34, 35].

Analysing riser systems is usually done numerically or experimentally, as for distributed-parameter systems (nonlinear PDEs) an analytical solution is not always feasible [24]. The solution to the equation of motion of a riser system can be obtained by static or dynamic analysis. The static analysis is performed to obtain the solution under a constant load, where inertia is not considered. For dynamic analysis, inertia, the time-varying load and the movements of the vessel are taken into account. There are three types of dynamic analysis: time-domain, frequency-domain and stochastic [28].

4.1.3. Hydrodynamic characteristics of a remotely operated vehicle

Public research is available on finding the hydrodynamic characteristics for complex-shaped remotely operated vehicles. Zan et al. (2020) show the result of an experimental and numerical analysis, to find insights into the asymmetric and non-linear effects in other degrees of freedom while moving in one or two degrees of freedom [36]. The numerical results are compared to experimental testing. The study revealed that additional hydrodynamic forces were present, solely due to the asymmetrical structure of the remotely operated vehicle [36]. The numerical study by Zan et al. (2020) is performed with the computational fluid dynamics (CFD) STAR-CCM+ numerical software, using the Reynolds-Averaged Navier-Stokes equations [36]. The analysis shows that the forces and moments in the direction of the motion were symmetrical and those perpendicular to the direction of the motion were asymmetrical in a longitudinal and vertical motion, due to the asymmetrical characteristics of the remotely operated vehicle [36]. This can be explained by vortex shedding.

A study by Li et al. (2020) researches the hydrodynamic characteristics of an open-frame remotely operated vehicle with the open-source CFD software OpenFOAM with four principal degrees of freedom using the Reynolds Averaged Navier–Stokes equations [37]. Again the numerical analysis is compared to experimental testing. Another study, about the hydrodynamic calculation and analysis of a complex-shaped underwater robot, was performed by Zhandong Li et al. (2017) [38]. Again CFD and experimental testing were used. The numerical simulation is divided into two types: a steady-state solution and an unsteady-state solution. The unsteady-state simulation was performed to find the inertial hydrodynamic coefficients. The steady-state simulation was performed to find the hydrodynamic force and moments. In all CFD simulations mentioned above, the turbulence model $k - \epsilon$ model is used, which is one of the most widely used turbulence models for external aerodynamics and hydrodynamics [39].

4.1.4. Modelling of mooring systems

In mooring systems, restoring forces are important, likewise the topic of this research. Mooring systems can be split into two types: catenary mooring systems, which have free-hanging catenaries that use gravity to anchor the floating unit, and a taut mooring systems, which use pre-tensioned mooring lines where the restoring force is generated by the elasticity in the mooring line. An analysis of a jumper hose is similar to catenary mooring systems [40]. For the static analysis, which is done to verify the parameters, an existing script of the course 'Introduction to Computational Dynamics for Offshore Structures' of the TU Delft, by Chris Keijdener and Joao Barbosa, is used [41]. The dynamic analysis is performed with the software package OrcaFlex [42].

4.2. Modelling techniques

Based on the other fields described in Section 4.1 and the analytical analysis in Chapter 3, the following modelling techniques are chosen for this thesis: an experimental test and a CFD analysis. The experimental test includes the dynamics of the system, while the CFD analysis studies the fluid mechanics to take away the uncertainties and unknowns.

An alternative would have been a dynamic analysis. To perform a correct dynamic analysis, the forces (input) must be known. Although the system itself and the operating circumstances are known in this thesis, the forces and moments acting on the container and cursor frame can only be approximated as the precise shape is not known in literature. Therefore, a dynamic analysis can be done based on empirical equations and uncertainty will remain.

4.2.1. Experimental testing

The behaviour of the system can be estimated by experimental testing. In literature, experiments are usually performed to validate a numerical model. In this thesis, the experiment presents a better understanding of how the container and cursor move during vertical transport, prior to modelling. The goal of the experiment is to examine if unexpected movements appear and it is a way to validate further modelling. The dynamics of the system are included. However, accurate experimental testing is difficult, as scale effects are a challenge for the vertical transport system of this thesis, as the system is large and the velocities are high, and measurement errors are easily present.

4.2.2. CFD analysis

Computational fluid dynamics (CFD) in the maritime industry has been used for resistance and propulsion computations of ships. As the accuracy level has evolved over the years, CFD is nowadays useful for evaluating manoeuvring characteristics for marine vehicles as well [39]. In this thesis, a CFD analysis can take away the uncertainties in the forces and moments acting on the container and cursor frame. In the CFD analysis, the container and cursor are fixed. Therefore, the analysis is static, as the system cannot move. Multiple simulations are performed to obtain results for different configurations. The question answered with the CFD analysis after validation of the model, is summarised by: What is the drag and the yawing moment on the container and cursor frame and what are the fluctuations?

5 Experimental test

The objective of the experiment is to obtain a first indication and understanding of the yawing moment on the system. The experiment is performed, as the dynamics of the system and the effect of the response of the system on the excitation forces and moments are included.

In this chapter, all model scale values for depth, tension, velocity and time are converted to full scale values.

5.1. Scaling

To obtain dynamic similitude between full and model scale while scaling the dimensions, loads and characteristics, the Froude number and the Reynolds number must be identical. However, it is typically not possible to keep both numbers constant, as they require different geometric values [43]. Scaling according to Froude is represented by

$$\frac{U_M^2}{gL_M} = \frac{U_F^2}{gL_F}, \tag{5.1}$$

with
U as the relative velocity [m/s],
g as the gravitational acceleration [m/s^2],
L as the characteristic length [m].

Scaling according to Froude scales the viscous forces incorrectly, for instance the drag force. At the model scale, the Reynolds number decreases significantly due to the lower speed and smaller dimensions calculated by Froude scaling, which influence the flow around the system. [redacted]

In this thesis, the parameters at model scale are determined according to Froude scaling, implying that the experiment operates at a lower Reynolds number compared to full scale. If the Reynolds number is significantly lower, some of the turbulent characteristics might disappear. Therefore, a CFD simulation of the experimental test is performed. The simulation is compared to the result of the simulations at full scale, to argue if the experimental test is representative for full scale and what the differences are. This is done in the discussion in Chapter 7.

5.2. Parameters

The scaling factor is chosen according to the frame length, which should be large enough that rotation can be visible and small enough to avoid interference with the boundaries of the water basin. Assumed is that the object at model scale should at least be 6 times smaller than the diameter of the water basin. As the water basin has a diameter of [redacted] Scaling according to Froude results in a scaling [redacted] in Appendix G.

Table 5.1: Reynolds numbers for scaling factor λ = 100 for the container and cursor frame transporting at 2 and 3 m/s.

[redacted]

The container and cursor frame are 3D printed to obtain the correct shape and dimensions. The hoisting and lowering is done by a single lifting wire connected to a motor, adjusted to the correct speed with the use of gears. Instead of four guidance wires, the system is equipped with two guidance wires for simplification, as shown in Figure 5.1, with the tension in the wires adjusted to account for the total restoring moment. Besides, at model scale one lifting wire is used. This can be done due to the large elongation of the ropes, as explained in Appendix D.

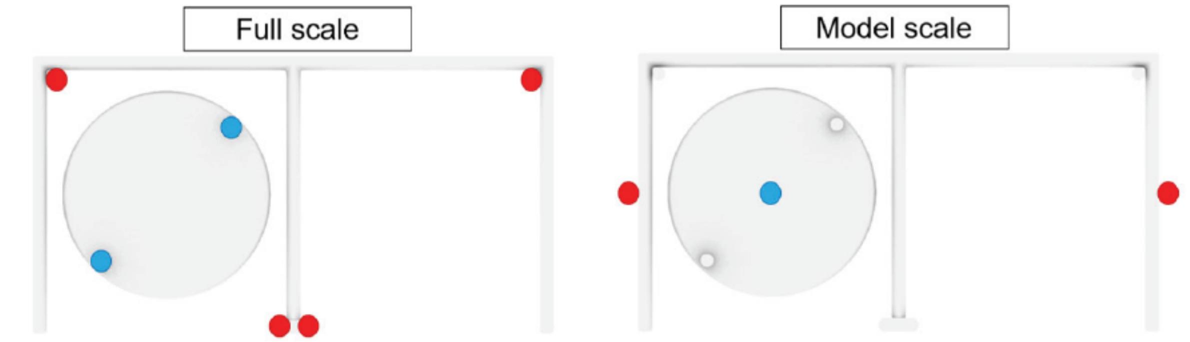

(a) (b)

Figure 5.1: Lifting and guidance wires at full scale (a) and model scale (b) with the lifting wires in blue and the guidance wires in red.

The guidance wires are fixed to a plate on the bottom of the water basin and at the top of the basin the [redacted]

Figure 5.3a shows the restoring moment for a yaw rotation of 45° as a function of the depth for multiple tensions at model scale. At full scale, over a section of 250 m, the rotational stiffness remains roughly constant. Figure 3.5b shows the rotational stiffness at full scale and at model scale for the different

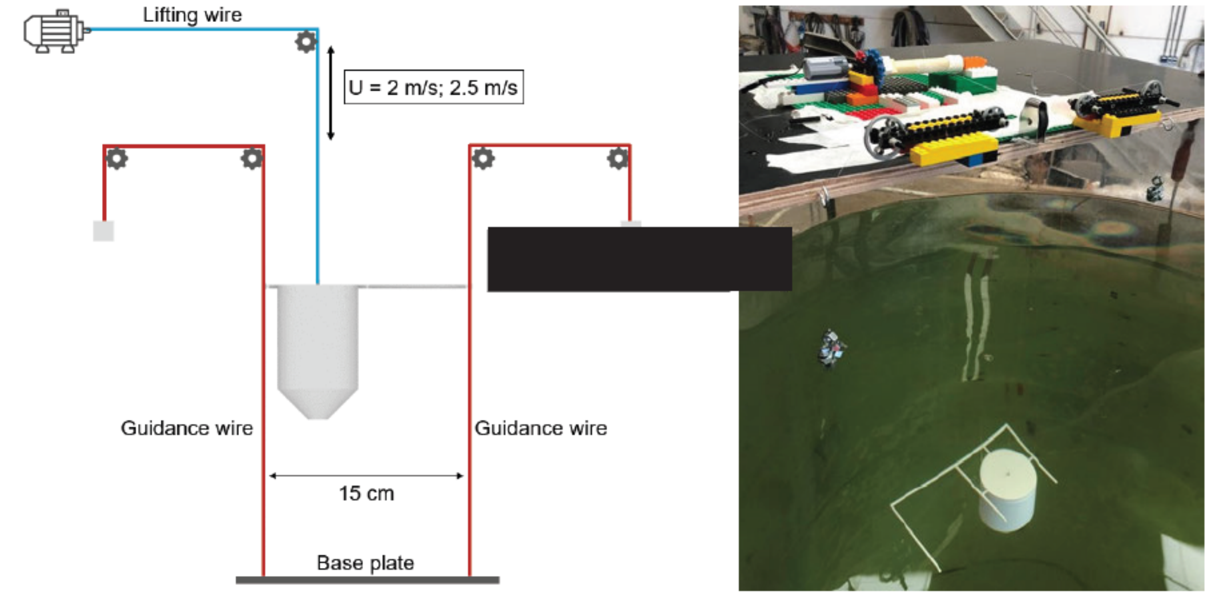

(a) (b)

Figure 5.2: Schematic overview (a) and picture (b) of the setup of the experimental test.

tensions, found by dividing the restoring moment by the rotation angle. At model scale the rotational stiffness is not constant, as the guidance wires are attached to the top and bottom of the basin. Therefore, in the experiment only the middle 100 m are used, to obtain a roughly constant rotational stiffness.

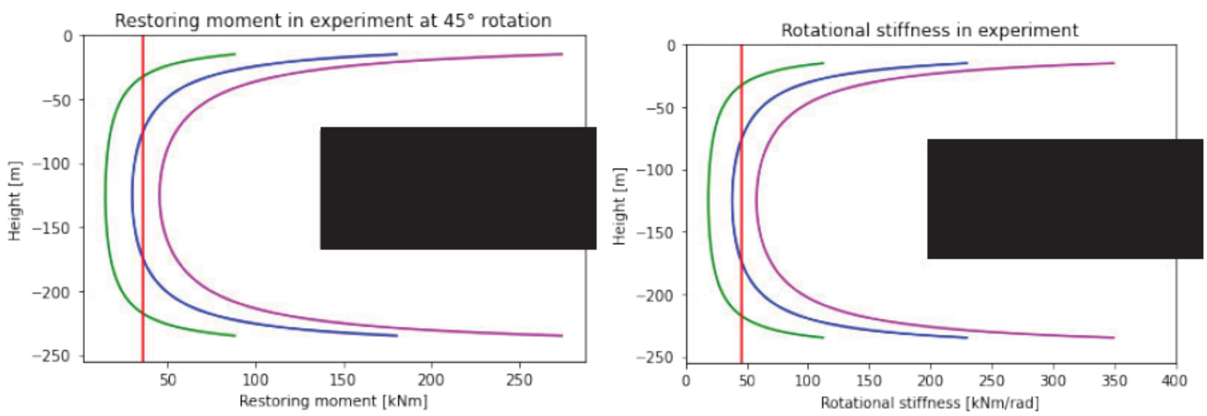

(a) (b)

Figure 5.3: The restoring moment for a yaw rotation of 45° (a) and the rotational stiffness (b) as a function of the height of the test basin for multiple tensions.

The system will not rotate immediately due to its inertia. To assess whether the test tube is long enough to observe yaw rotations, the eigenperiod of the system at the model scale is calculated and shown in Figure 5.4. The time to transport the system at model scale through the test tube is 9 to 11 seconds, corresponding to the speeds 2 and 2.5 m/s at full scale, as defined in Appendix G. The graphs show that the eigenperiod fo[redacted] large compared to the transport time in the experiment.

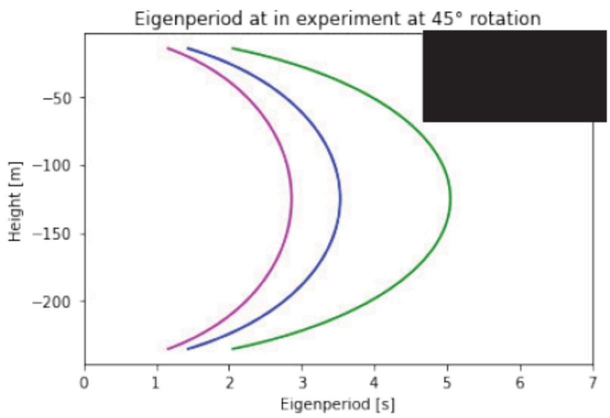

(a)

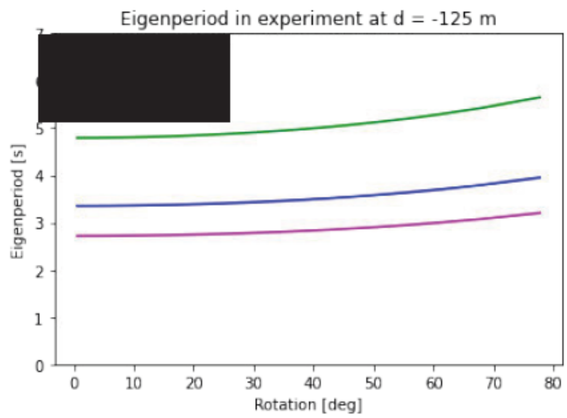

(b)

Figure 5.4: The eigenperiod for a yaw rotation of 45° as a function of the height of the test basin (a) and the eigenperiod in the middle of basin at d = - 125 m as a function of the yaw rotation (b) for multiple tensions.

While performing the experiments a camera is suspended above the basin, that records each lowering and hoisting transportation. Afterwards, two snapshots, at the top and bottom of the 100 m section, are taken per video. The change in yaw rotation is measured and combined in graphs. Four different configurations are tested, as shown in Figure 5.5: a flat and conical top of the container and an initial pitch angle upwards and downwards. The conical top is chosen as it would reduce the drag significantly while hoisting, which can be seen by the estimation of the drag coefficient in Figure F.2 in Appendix F.

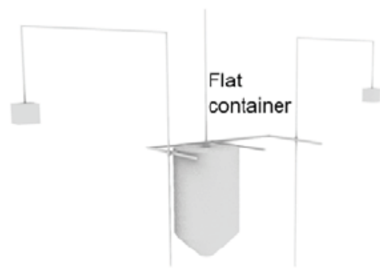

(a)

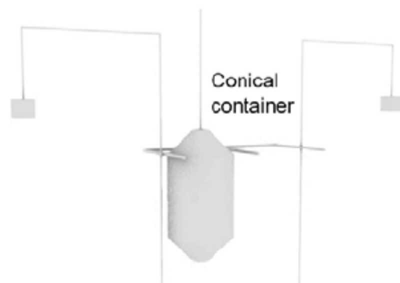

(b)

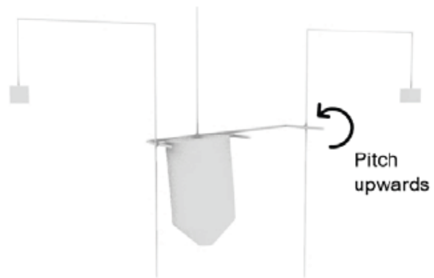

(c)

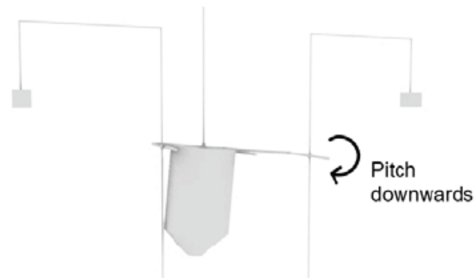

(d)

Figure 5.5: The four configurations tested in the experiment: Flat top of the container (a), conical top of the container (b), initial pitch angle upwards (c) and initial pitch angle downwards (d).

5.3. Results

First the system is transported with a flat and conical container, corresponding to the situations in Figure 5.5a and 5.5b. Figure 5.6a shows the results for lowering and Figure 5.6b for hoisting. The tests were carried out at two velocities, 2 and 2.5 m/s. Although the tests were carried out with no initial pitch, due to drag the system tilts during transportation.

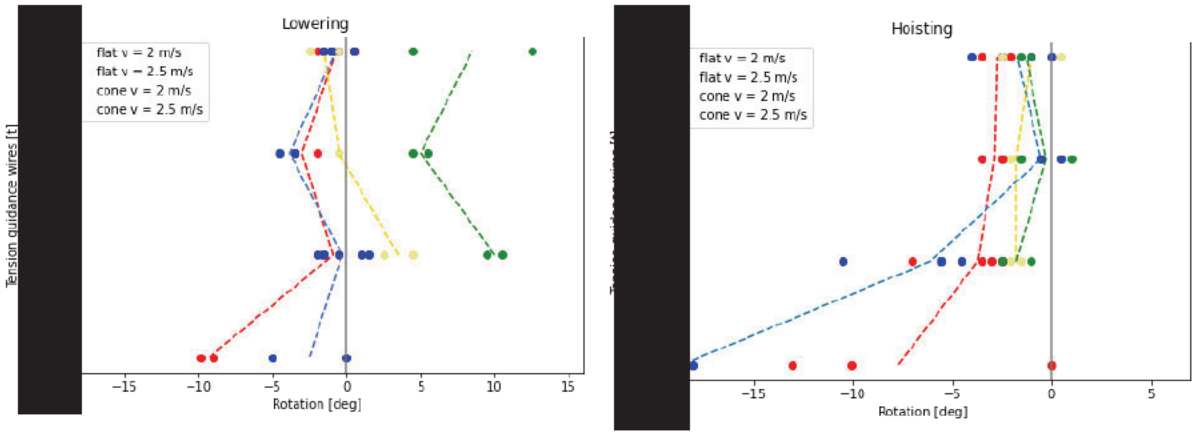

(a) (b)

Figure 5.6: Results of the experimental test with zero initial roll and pitch for lowering (a) and hoisting (b) of the system with a flat and conical topside of the container at 2 and 2.5 m/s.

Figure 5.6 shows the following:

- During lowering, Figure 5.6a shows that for a tension of [redacted] yaw rotation is smaller compared [redacted] This could be due to the eigenperiod of the experiment being too high compared to the transport time in the test tube. The rotation may not have been developed.
- The flat top of the container, shows for both hoisting and lowering negative yaw rotations, with no clear difference between the two velocities. Hoisting shows larger yaw rotations.
- For the conical top of the container, the yawing rotation is positive for lowering, which could be due to water releasing in a different manner compared to the flat top of the container. In hoisting the conical top reduces the yaw rotation compared to the flat top, while the rotation remains negative.
- No clear difference can be obtained between the two velocities. Overall the yaw rotations are rather small and therefore clear differences between the configurations cannot be obtained.

Secondly, tests have been performed with an initial pitch angle, corresponding to Figure 5.5c and 5.5d. Figure 5.7a shows the results for lowering and Figure 5.7b for hoisting. These tests are carried out at a constant velocity of 2.5 m/s and the result for system without an initial pitch is also shown in the figures for comparison.

Figure 5.7 shows the following:

- Again during the tension of [redacted] smaller yaw rotations compared to a higher tension.
- During lowering, the container and cursor frame show negative yaw rotations for a downwards initial pitch angle, similar to a flat frame. However, an upwards pitch angle shows positive yaw rotations.

- In hoisting, all operations show negative angles. Besides, hoisting shows larger rotation angles for both pitched configurations compared to no initial pitch.
- Overall the yaw rotations are rather small.

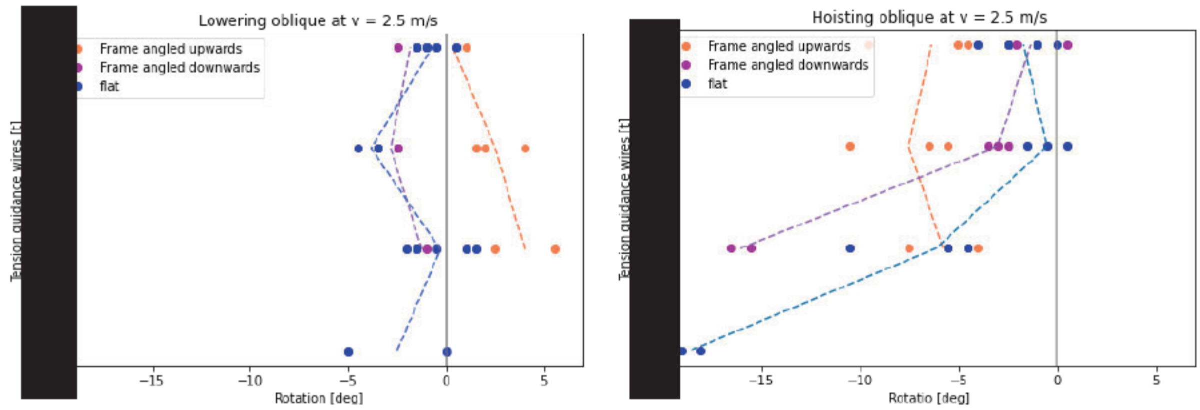

(a) (b)

Figure 5.7: Results of the experimental test for an initial pitch angle for lowering (a) and hoisting (b) of the system with a flat topside of the container at 2.5 m/s.

In all experiments mentioned above, the yaw rotations are measured by hand, measurement errors in the order of 1° to 2° could be made.

5.4. Analytical time integration

A time integration calculation is performed, to validate the response of the system in the experiment. This calculation shows whether the test tube of the experiment is long enough to develop the yaw rotations. The steps are

$$\begin{aligned} \dot{\theta}_1 &= \dot{\theta}_0 + \ddot{\theta}_0 \cdot \Delta t, \\ \theta_1 &= \theta_0 + \frac{\dot{\theta}_0 + \dot{\theta}_1}{2} \cdot \Delta t + \frac{1}{2} \cdot \ddot{\theta}_0 \cdot (\Delta t)^2, \end{aligned} \tag{5.2}$$

with
θ as the rotation [rad],
$\dot{\theta}$ as the angular velocity [rad/s],
$\ddot{\theta}$ as the angular acceleration [rad/s^2],
Δt as the time step [s].

The acceleration $\ddot{\theta}$ can be defined by Newton's second law: $a = \frac{F}{m}$. For rotation, this can be rewritten as $a = \frac{M_{total}}{I_{rot}}$, with M_{total} as the total moment acting on the system and I_{rot} as the mass moment of inertia. The total moment M_{total} includes restoring, yawing and damping. The acceleration is

$$\ddot{\theta} = \frac{M_{total}}{I_{rot}} = \frac{M_{rest} + M_{yaw} + M_{damp}}{I_{rot}}, \tag{5.3}$$

with

$$\begin{aligned} M_{rest} &= K_{rot} \cdot \theta, \\ M_{yaw} &= M_{yaw,static} + M_{yaw,dyn} \cdot \sin(\omega_{yaw} \cdot t + \phi_{yaw}), \\ M_{damp} &= \frac{\dot{\theta}}{C_{rot}}, \end{aligned} \tag{5.4}$$

[redacted]

The damping coefficient C_{rot} is found by comparing the time-integration calculation to a decay test. The system of the container and cursor frame in the water basin is released at an angle of 42° and 92° respectively and the excitation is measured. The tension in the wires is set to mimic the middle of the water depth at full scale. The result of the decay tests is shown in Figure 5.8. C_{rot} can be found by setting the initial rotation θ_0 to 42° and 92° respectively, the initial velocity $\dot{\theta}_0$ to zero and the yawing moment to zero. [redacted]

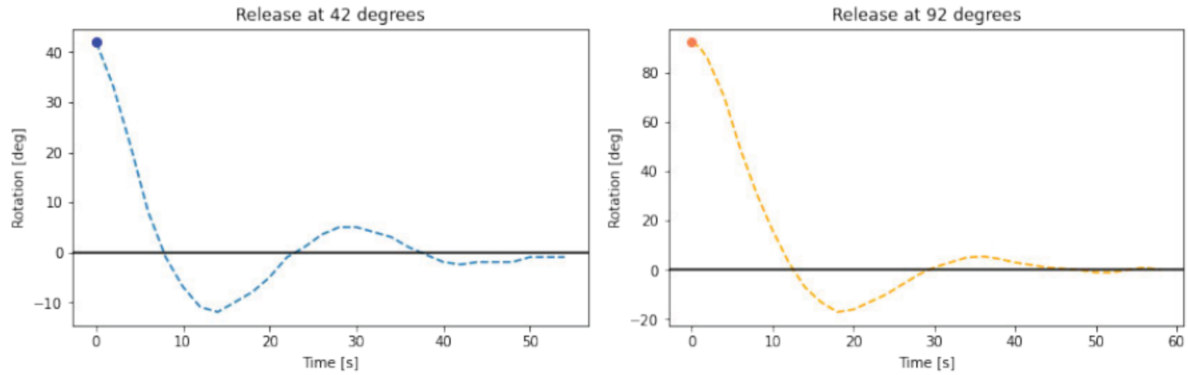

Figure 5.8: Result of the decay tests with a release at 42° (a) and 92° (b).

With the obtained value for the damping, a static and dynamic yawing moment can be chosen and the analytical result can be plotted. Four solutions are shown in Figure 5.9. From the graph, it can be seen that if a yawing moment were to act on the system, consisting of a static and/or dynamic moment, the experiment would show a yaw rotation. The water basin is therefore validated to be long enough. Secondly, from the graph can be concluded that if a dynamic rotation is seen in the experiment, a dynamic moment is exerted on the system. The dynamic rotation would not be caused by 'overshooting'.

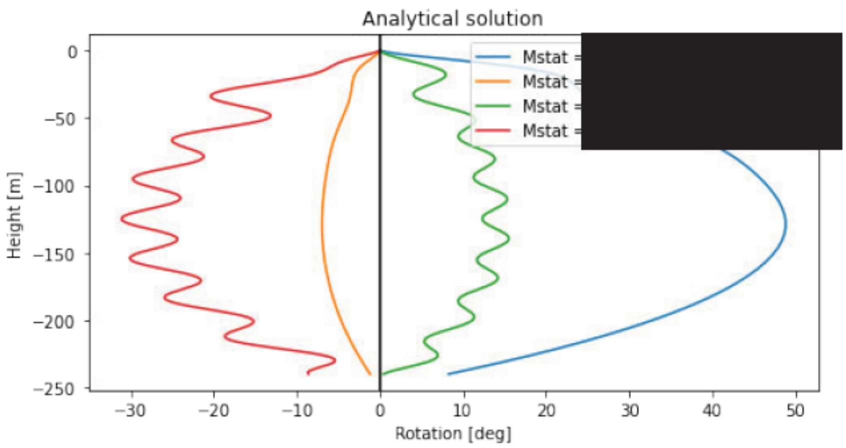

Figure 5.9: Results of the analytical solution to validate the experimental test.

6 CFD analysis

This chapter shows the CFD analysis of the container and cursor frame. The objective of the CFD analysis is to quantify the drag, the yawing moment and the fluctuation magnitudes and frequencies. First OpenFOAM and the CFD model are described. The model is validated by simulating a 2D cylinder and a 3D sphere, and a mesh convergence study is performed, to validate the mesh used in the simulations of the container and cursor frame. Thereafter, the simulations are executed. An overview is presented in Figure 6.1. The green boxes indicate an analysis that is presented in the Appendices and the blue boxes indicate the six CFD simulations presented in this chapter: Lowering at 2 and 3 m/s, lowering with an oblique system due to its self-weight and drag at 2 and 3 m/s including a current of 0.1 m/s, hoisting at 2 m/s and a simulation of the experiment, which is lowering at model scale at 0.2 m/s.

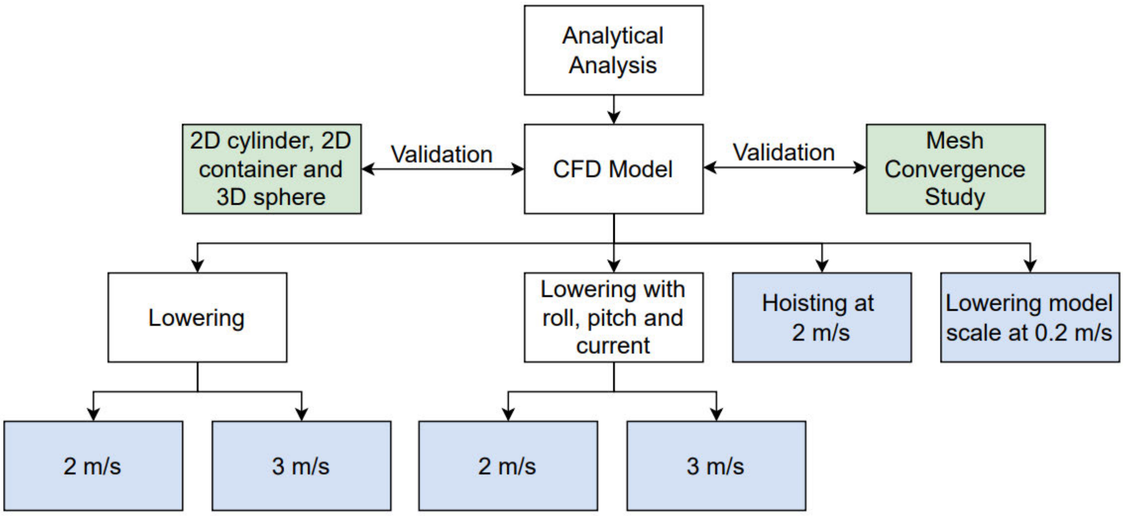

Figure 6.1: Overview of the CFD analysis.

6.1. OpenFOAM

The analysis is performed in OpenFOAM. OpenFOAM is an open-source software package, a `C++` library, that can solve partial differential equations (PDEs) and stands for Field Operations And Manipulation. OpenFOAM can do CFD calculations, but also finite element and financial calculations as those are based on PDEs. The first stage in OpenFOAM is pre-processing, where the domain, the mesh, the initial conditions and boundary conditions are defined. The mesh in this thesis is obtained with `snappyHexMesh`. The second phase is solving by choosing solver and models that apply to the problem. The final phase is post-processing. In this thesis, the result is post-processed with `ParaView` and Python.

OpenFOAM uses a case folder structure. The structure consists of three main folders: `0`, `constant` and `system`. The folder `0` contains the initial conditions at the inlet, outlet, boundaries and object. The `constant` folder contains all constants, including the mesh geometry, fluid properties and turbulent settings. The folder `system` contains all information for solving the problem, including the differential schemes, solvers and time domain. A typical folder structure is shown in Figure 6.2.

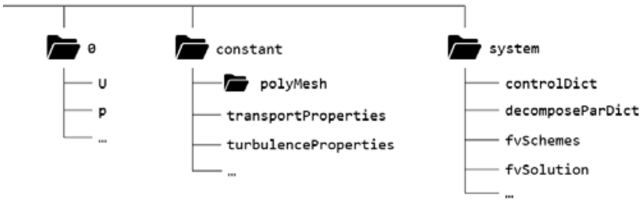

Figure 6.2: Overview of a typical case folder structure in OpenFOAM.

As OpenFOAM is open-source software, the working principles can be investigated and checked whether the simulation is done correctly. Besides the code can be modified to whatever function the user wants. There are numerous solvers and boundary conditions and is therefore flexible. A final advantage is that there are no license costs for the software. However, there are some disadvantages when using OpenFOAM as the CFD software. The largest disadvantage is the lack of a user manual, resulting longer learning paths when setting up the cases. Besides, there is no GUI as OpenFOAM works with a terminal only, which is less intuitive and can therefore be difficult. Finally, different packages exist and it is not always possible to interchange between the packages for a specific case.

6.2. CFD model

The problem of this thesis is a fully submerged object pulled through the water column with a current acting on the object. The problem can be modelled as an object with the fluid moving, instead of the object moving, to simplify the model. The Reynolds numbers at full scale are in the order of 5E+05 to 1E+07, as shown in Table 3.4, and thus the flow is fully turbulent. As the density and the viscosity remain constant, the flow can be modelled as an incompressible Newtonian fluid. The flow is governed by the unsteady incompressible Navier-Stokes equations:

$$\begin{aligned} \text{momentum equation: } \delta u_t + u \cdot \nabla u + \frac{1}{\rho}\nabla p - \nu \nabla^2 u = 0, \\ \text{continuity equation: } \nabla \cdot u = 0, \end{aligned} \tag{6.1}$$

with
u as the flow velocity [m/s],
ρ as the density [kg/m^3],
p as the pressure [Pa],
ν as the kinematic viscosity [m^2/s].

6.2.1. Solver: PimpleFOAM

The Navier-Stokes equations have to be solved numerically. In this thesis, the solver PimpleFOAM is used, which is a transient solver of 3D incompressible, unsteady (turbulent) flows of Newtonian fluids. The PimpleFOAM solver uses the PIMPLE algorithm, which is a combination of PISO (pressure-implicit with splitting of operators) and SIMPLE (semi-implicit method for pressure-linked equations), to solve the equations.

6.2.2. Turbulence model: Detached-Eddy Simulation

As the flow is fully turbulent, separation, reattachment and vortex shedding could occur, which makes the simulation quite complicated. Reynolds-Averaged Navier-Stokes (RANS) simulations can only model the mean flow and thus spectral effects get lost [44]. For the topic of this thesis, the fluctuations are important and therefore RANS is not applicable. Direct numerical simulation and large-eddy simulation could be a good alternative. However, these simulations are computationally non-affordable at high Reynolds numbers [44]. A hybrid approach, detached-eddy simulation, is therefore chosen in this research. It takes into account most of the flow unsteadiness at reasonable computation times [44].

A turbulent flow can be described as an averaged value and a fluctuation: $u = \overline{u} + \tilde{u}$. Substituting this in the momentum equation gives

$$\begin{gathered} \delta\overline{u}_t + \delta\tilde{u}_t + (\overline{u} + \tilde{u}) \cdot \nabla(\overline{u} + \tilde{u}) + \overline{u} \cdot \nabla\overline{u} + \tilde{u} \cdot \nabla \\ \overline{u} + \overline{u} \cdot \nabla\tilde{u} + \tilde{u} \cdot \nabla\tilde{u} - \nu \cdot \nabla\overline{u} - \nu \cdot \nabla\tilde{u} \\ + \frac{1}{\rho}\nabla\overline{p} + \frac{1}{\rho}\nabla\tilde{p} = 0. \end{gathered} \tag{6.2}$$

This can be rewritten as

$$\delta\overline{u}_t + \overline{u} \cdot \nabla\overline{u} - \nu \cdot \nabla\overline{u} + \frac{1}{\rho}\nabla\overline{p} + F(\tilde{u}) = 0, \tag{6.3}$$

with

$$F(\tilde{u}) = \delta\tilde{u}_t + (\overline{u} + \tilde{u}) \cdot \nabla(\overline{u} + \tilde{u}) + \tilde{u} \cdot \nabla\overline{u} + \overline{u} \cdot \nabla\tilde{u} + \tilde{u} \cdot \nabla\tilde{u} - \nu \cdot \nabla\tilde{u} + \frac{1}{\rho}\nabla\tilde{p}. \tag{6.4}$$

$F(\tilde{u})$ contains all terms dependent on $\tilde{u}$ and can be estimated in the CFD analysis by using a turbulence model. In this thesis, the turbulence model 'SpalartAllmarasDDES' is used, with its formulation described in [45].

6.2.3. Spatial discretization

The spatial discretization in OpenFOAM is achieved by the Finite Volume Method (FVM), which subdivides the fluid domain into a finite number of control volumes. Each volume is considered homogeneous and has single-averaged physical properties. FVM is used, because volume-averaged quantities have more physical meaning compared to point values and the conservation laws can be secured [46]. The foundation of the FVM is Gauss' theorem, which is shown in Equation 6.5. The theorem states that the integral of the divergence of a given vector, generic vector $\vec{a}$ in the equation, over a volume is equal to the flux of this vector across a closed surface bounding the volume [46].

$$\oint_V (\nabla \cdot \vec{a}) dV = \oint_S \vec{a} \cdot \hat{n} dS. \tag{6.5}$$

Using Gauss' theorem for the continuity equation results in

$$\begin{gathered} \partial_t \rho + \nabla \cdot \rho\vec{u} = 0, \\ \frac{d}{dt}\oint_V \rho dV = -\oint_S \rho\vec{u} \cdot \hat{n} dS. \end{gathered} \tag{6.6}$$

The change in time of the total mass in volume V is equal to the flux of the water across the surfaces that bound the volume [46].

6.2.4. Temporal discretization

When predicting the oscillation in a flow past an object in the transient space using DES or LES, a second-order temporal scheme is most suitable. The backward scheme, which uses a three-point difference, is therefore selected. The scheme is implicit [47].

6.2.5. Boundary and initial conditions

The boundaries in the CFD model are the boundaries of the fluid domain and the object itself. As OpenFOAM cannot calculate 2D cases, the 2D cases, like 3D cases, have 6 boundaries of the fluid domain. In 2D these are defined as inlet, outlet, top, bottom and 2 sides. In 3D cases, these are defined as inlet, outlet and 4 sides. For each boundary and the internal field, an initial condition is defined for the pressure and the velocity. An initial condition for ν_t and $\tilde{\nu}_t$ is defined as well, which is necessary for the turbulence model. The boundaries and initial conditions are summarised in Table 6.1 for the 2D cases and Table 6.2 for the 3D cases, for lowering at 2 m/s. The conditions for lowering at 3 m/s can be obtained by substituting the 2 by a 3. The conditions for hoisting can be obtained by adding a minus sign in the velocities and exchange the conditions for the inlet and outlet. In the internal field, the pressure is zero, as OpenFOAM works with gauge pressures.

Table 6.1: Overview of the boundary and initial conditions for the 2D cases for lowering at 2 m/s.

2D

ID	Boundary	Type	$p_{t=0}$ [Pa]	$U_{t=0}$ [m/s]	ν_t [m^2/s]	$\tilde{\nu}_t$ [m^2/s]
1	Object	Wall	zeroGradient	U = (0, 0, 0)	ν-func *	zeroGradient
2	Inlet	Patch	zeroGradient	U = (2, 0, 0)	calculated	$\tilde{\nu}$ = 1.76E-06
3	Outlet	Patch	p = 0	inletOutlet	calculated	inletOutlet
4	Top	Patch	zeroGradient	zeroGradient	calculated	zeroGradient
5	Bottom	Patch	zeroGradient	zeroGradient	calculated	zeroGradient
6	Side	Patch	empty	empty	empty	empty
7	Side	Patch	empty	empty	empty	empty
0	Internal Field	-	p = 0	U = (2, 0, 0)	ν = 1.76E-06	$\tilde{\nu}$ = 1.76E-06

Table 6.2: Overview of the boundary and initial conditions for the 3D cases for lowering at 2 m/s.

3D

ID	Boundary	Type	$p_{t=0}$ [Pa]	$U_{t=0}$ [m/s]	ν_t [m^2/s]	$\tilde{\nu}_t$ [m^2/s]
1	Object	Wall	zeroGradient	U = (0, 0, 0)	ν-func *	zeroGradient
2	Inlet	Patch	zeroGradient	U = (0, 0, 2)	calculated	$\tilde{\nu}$ = 1.76E-06
3	Outlet	Patch	p = 0	inletOutlet	calculated	inletOutlet
4	Side	Patch	zeroGradient	U = (0, 0, 0)	ν-func *	zeroGradient
5	Side	Patch	zeroGradient	U = (0, 0, 0)	ν-func *	zeroGradient
6	Side	Patch	zeroGradient	U = (0, 0, 0)	ν-func *	zeroGradient
7	Side	Patch	zeroGradient	U = (0, 0, 0)	ν-func *	zeroGradient
0	Internal Field	-	p = 0	U = (0, 0, 2)	ν = 1.76E-06	$\tilde{\nu}$ = 1.76E-06

* nutUSpaldingWallFunction: a wall constraint on the turbulent viscosity.

6.2.6. Verification

To verify the simulations in a CFD analysis, the user checks whether the analysis is performed correctly. The two variables to verify are the mesh size and the time step, which should both be small enough to capture the physics. However, a small mesh size and time step result in large computation times and therefore optimisation is necessary. To verify the mesh size, the results must converge, meaning that when a smaller mesh size is chosen, the result of the CFD analysis should be equal. To verify the time step, one needs to pay attention to the Courant number. The Courant number is a dimensionless number that provides a measure of the rate at which information is transported. For the application of this thesis, the Courant number represents the time that a particle stays in one cell of the mesh, which is defined by

$\frac{U \cdot \Delta t}{\Delta x}$. If the Courant number is too large, meaning larger than 1, the time step is too large and a particle "skips" a cell. This is visible in Figure 6.3, where CFL denotes the Courant number. For a Courant number lower than 1, no cells are "skipped" and the time step is verified. For explicit cases, the Courant number should always be below 1 [48]. However, for implicit cases, like this thesis, the Courant number can be a little above 1 and still obtain the correct results [48].

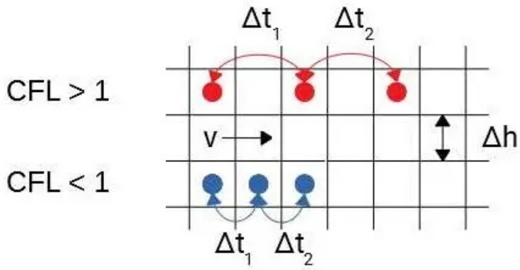

Figure 6.3: Stability criterion for the Courant number [48].

A final verification step of the CFD is taking a close look at the residuals. Every cell in the simulation needs conservation of energy and the residual is an extra term that represents the local energy imbalance in a particular cell. The closer the residual term is to zero, the more accurate the solution is. The residuals have the same unit as the source term. A residual exists for each cell in each iteration at every time step. To track the residuals, a representative residual can be calculated, which is done by OpenFOAM. When the representative residual does not change anymore, the solution is most likely to converge. For each simulation in this thesis, the representative residuals are plotted for the final iterations.

6.2.7. Validation

The CFD model is validated by starting with simplified simulations. First a 2D cylinder is simulated, which is validated by literature. The model is extended to a 3D simulation of a sphere, which is validated by literature as well. Once the model is validated, the container and cursor frame are simulated and the results are compared to the analytical calculations from Chapter 3.

6.3. Configurations

The CFD analysis consists of five simulations at full scale, including the lowering and hoisting operation. The lowering operation is simulated with a velocity of 2 and 3 m/s respectively and with and without initial pitch, roll and current. The initial roll and pitch angles are defined after the simulations of lowering at 2 and 3 m/s. The hoisting operation is simulated transporting at only 2 m/s due to computational power. The configurations for lowering are shown in Figure 6.4 and hoisting in Figure 6.5.

All simulations result in graphs for the forces on the system in the X-, Y- and Z-direction and moments around the X-, Y- and Z-axis. The moment around the Z-axis signifies the yawing moment and with the forces in Z-direction the drag coefficient can be calculated. Before simulating the container with the cursor, the model has been tested by a 2D cylinder, 3D sphere and 2D container. The results of the model validation are presented in Appendix H: CFD model validation. The 2D cylinder and 2D container match well with literature. The drag coefficient from the CFD analysis of the 3D sphere is in the expected region compared to literature, although it is slightly lower than expected. This can be seen in Figure H.16. However, little literature is available about a sphere with a Reynolds number higher than 1E6.

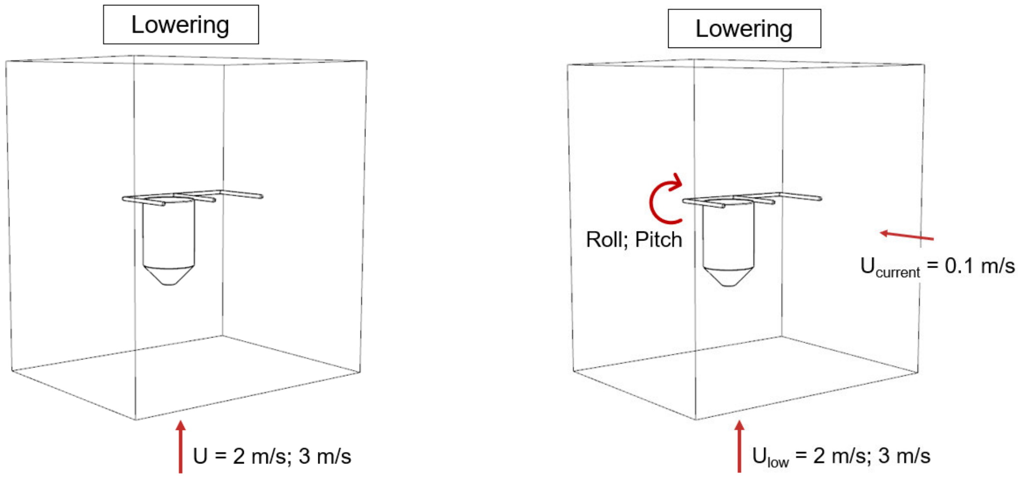

(a) (b)

Figure 6.4: Configurations for lowering in the in the CFD simulations: Lowering at 2 and 3 m/s (a), lowering with initial roll, pitch and current at 2 and 3 m/s (b).

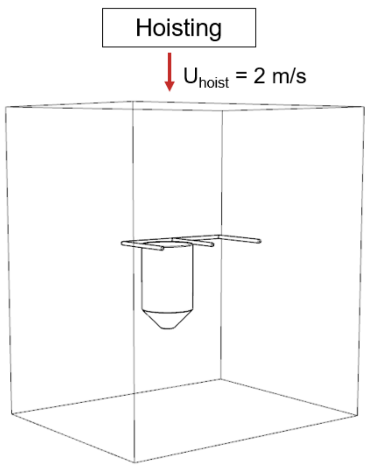

Figure 6.5: Configuration for hoisting in the CFD simulations: Hoisting at 2 m/s.

6.4. Mesh

The mesh for the container and cursor is defined by evaluating the lowering simulation. The mesh convergence study can be found in Appendix I and hereafter the chosen mesh is described.

First a grid is generated with BlockMesh, without including the container and cursor frame. BlockMesh is an internal tool in OpenFOAM, which can describe the domain of the simulations and the amount of cells in the domain. A domain [redacted] resulting in a structured grid. Of interest in this thesis, are the pressures at the container and cursor frame. The wake and surrounding fluid serves as a means to obtain the correct pressures at the system. Therefore, no refinement is required at this stage and thus simpleGrading is defined as (1 1 1), indicating that every cell has the same length. This is summarised by:

```
blocks
```

[redacted]

Next, the container and cursor are added using snappyHexMesh, a mesh refinement tool in OpenFOAM. The refinement is defined by levels that divide cells by the power of 2. Level 1 divides the cell into two, level 2 divides the cell into four, etc. The area around the container and cursor frame is defined by distances to the object and corresponding refinement levels. This is shown in the code below, where the first number in the brackets specifies the distance and the second the refinement level. In addition, a box is specified, that refines the wake behind the container with refinement level 2. The levels are defined as

```
[redacted]
}
```

The mesh for the lowering simulations is presented in Figure 6.6. The domain with refinement leads to 2,578,670 cells, 48,176 cells at the container and 46,005 cells at the cursor frame. The area of the container is [redacted] to an area [redacted] cursor frame. This shows that the refinement at the cursor is much larger. This is necessary to capture the physics at the cursor.

The forces are calculated by the 'forces' function in OpenFOAM. Below the set on entries is shown for the forces and moments at the cursor. The CofR indicates the centre of rotation of the moment calculations, which is the lifting point in this thesis. The density is set to 2025 kg/m^3. The forces at the container are defined in the same manner.

```
forces_cursor
{
        type            forces;
        libs            (forces);
        writeControl    writeTime;
        timeStart       0;

        patches         (cursor);
        CofR            (0 0 0);
        writeFields     yes;

        rho             rhoInf;
        rhoInf          1025;
}
```

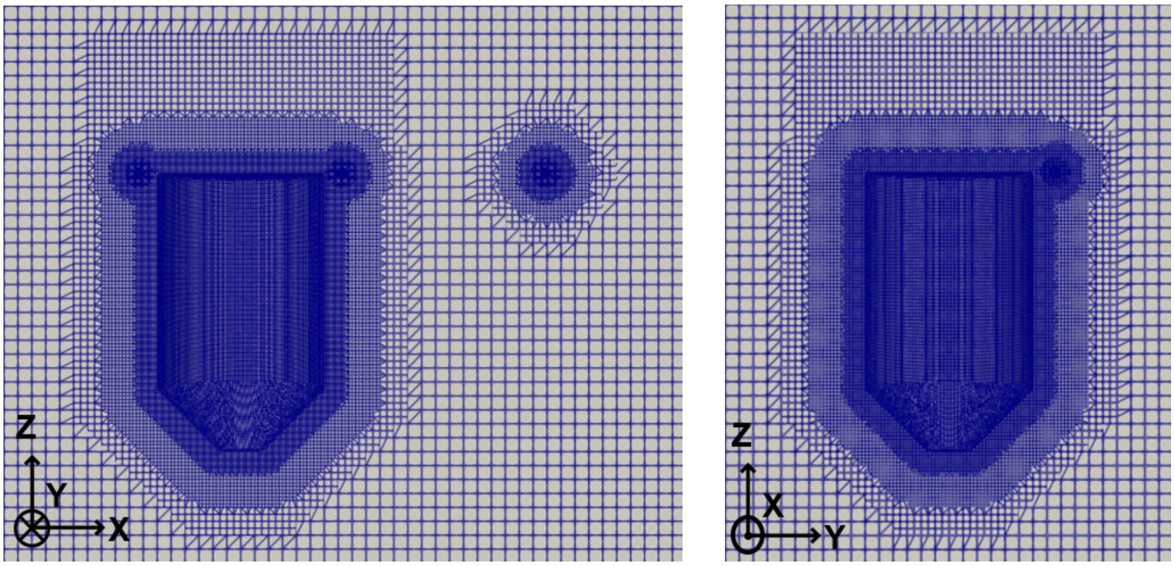

(a) (b)

Figure 6.6: Mesh for lowering the container with cursor frame along the X-axis (a) and Y-axis (b).

6.5. Result lowering

The first two simulations are the vertical transportation of the container and cursor frame with zero roll and pitch, and no current at 2 and 3 m/s. Figure 6.7 shows two snapshots of the flow field around the container and cursor frame along the X-axis and Y-axis at 2 m/s. As expected, the flow field is fully turbulent and large eddies arise next to the container. After the cursor, bending can be seen in the wake, which could indicate a vortex street. Figure 6.7 matches well with the obtained flow patterns from the analytical analysis in Figure 3.12 and Figure 3.13.

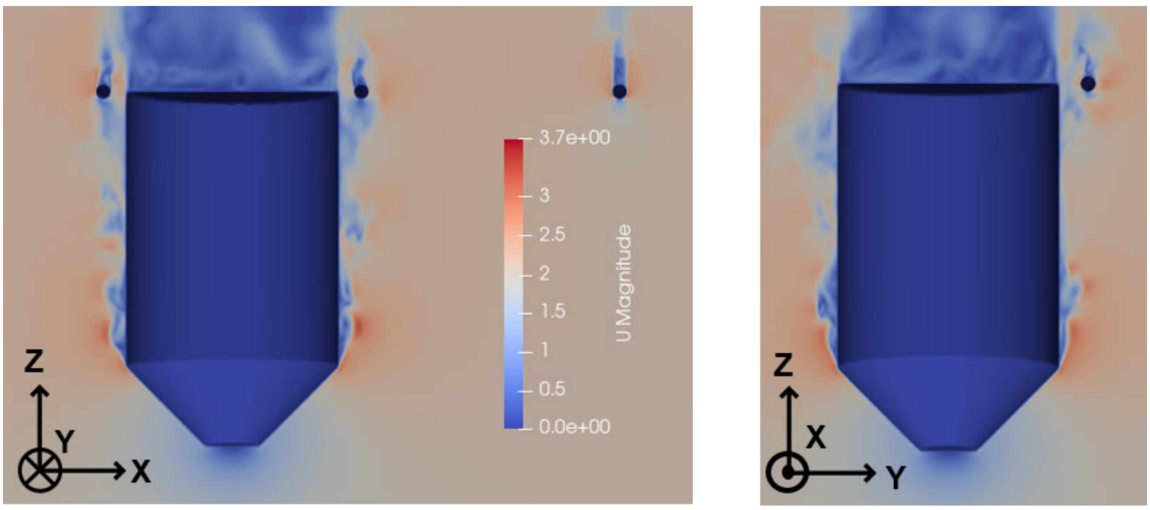

(a) (b)

Figure 6.7: Flow field around the container and cursor along the X-axis (a) and Y-axis (b) at 2 m/s.

Figure 6.8 shows the flow field around the container and cursor frame transporting at 3 m/s. The field is similar to the flow field at 2 m/s in Figure 6.7.

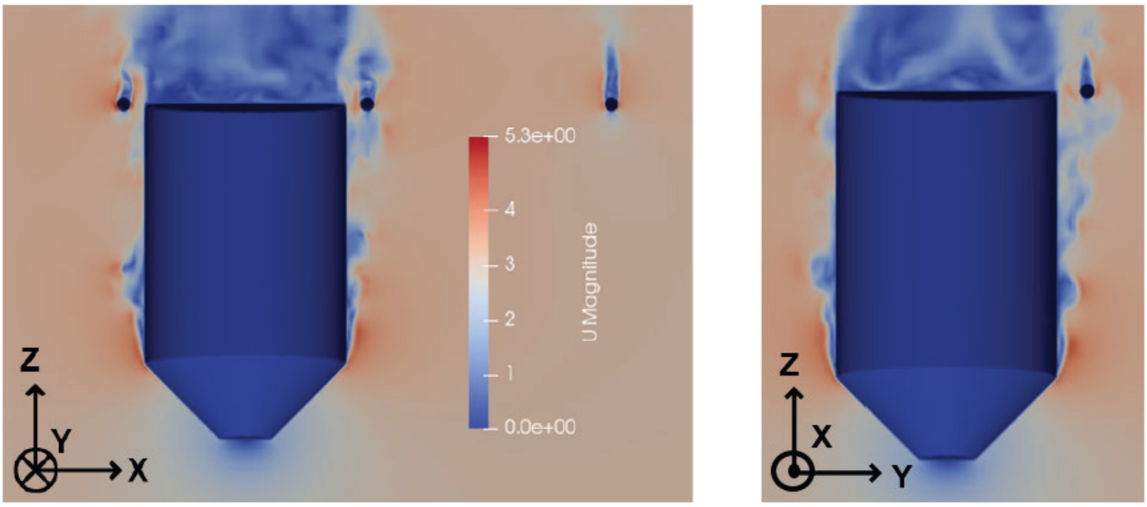

(a) (b)

Figure 6.8: Flow field around the container and cursor along the X-axis (a) and Y-axis (b) at 3 m/s.

Figure 6.9 shows the forces in the Z-direction and the resulting drag coefficients C_d for both cases.

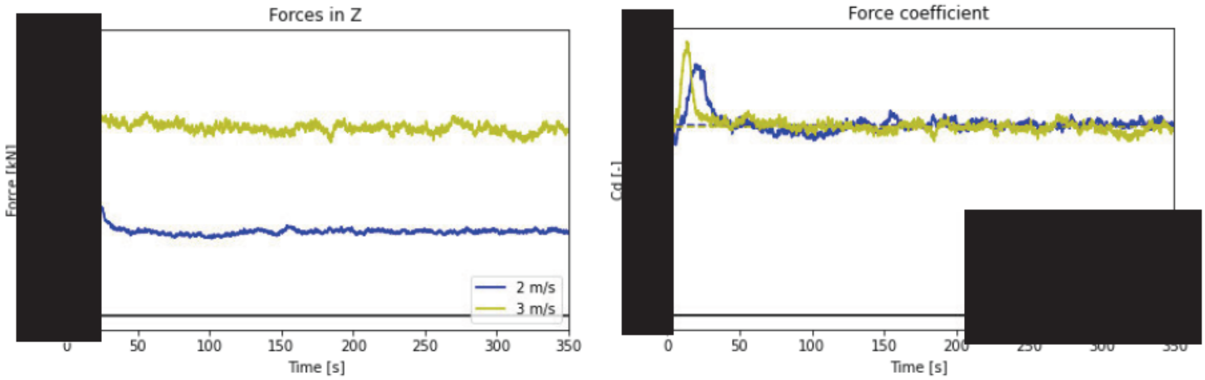

(a) (b)

Figure 6.9: Forces in Z-direction (a) and force coefficients (b) for lowering at 2 and 3 m/s.

[redacted]

[redacted] based on the combination of a cylinder with blunt nose and a cone, which could be inaccurate. Besides, in literature, the drag coefficient for cylinders with various nose shapes in an axial flow is mostly based on the shape rather than the Reynolds number, as shown in Appendix F.1. As the Reynolds number is uncommonly high for the container, the estimation from Chapter 3 could be wrong. To substantiate this, a CFD simulation has been performed where only the container, meaning without the cursor frame, is simulated. The result is shown in Figure 6.11, where the brown line corresponds

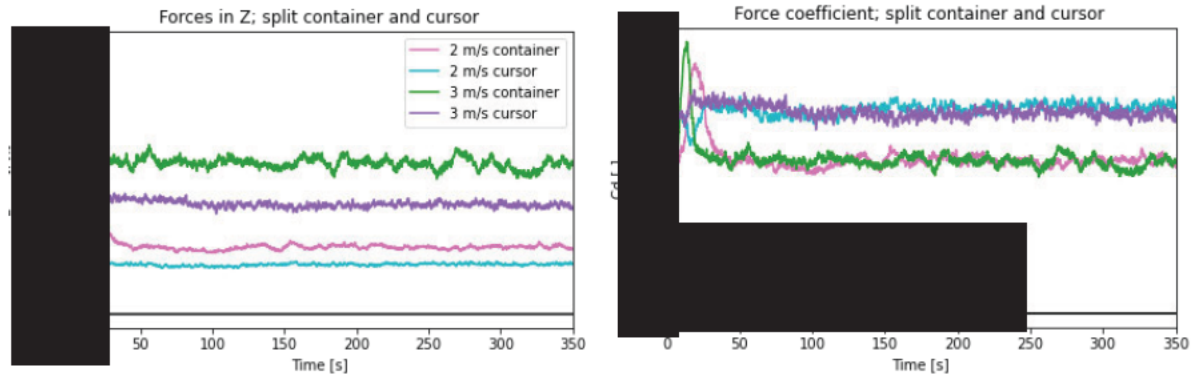

(a) (b)

Figure 6.10: Forces in Z-direction (a) and force coefficients (b) for lowering at 2 and 3 m/s split in the forces at the container and cursor frame.

to the simulation of only the container, meaning without cursor frame, and the pink line corresponds to the container taken from the simulation of the whole system. [redacted]

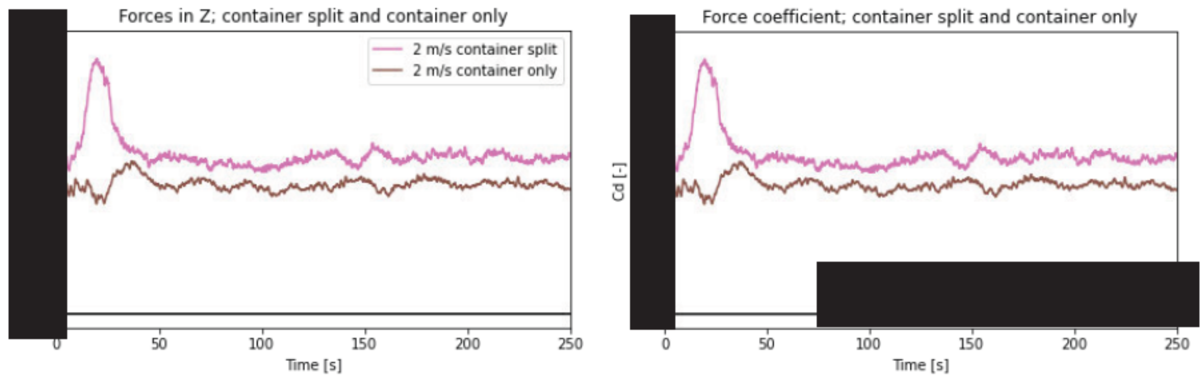

[redacted] (b)

Figure 6.11: Forces in Z-direction (a) and force coefficients (b) for the split container from the full system and the simulation of only the container lowering at 2 m/s.

The cursor frame is made of cylinders, which are well researched in literature. The difference between the initial estimation and CFD analysis is therefore most likely due to the interaction between the container and the cursor frame. The estimation from Section 3.3 assumes an undisturbed flow field. Figure 6.12 shows a snapshot of the flow field in Z-direction for lowering the container and cursor frame at 2 m/s a[redacted], which is right below the cursor frame. The figure shows a disturbed flow field arriving at the cursor frame, due to the container. The eddies reduce the flow velocity and therefore reduce the forces. This results in a lower drag coefficient for the cursor.

Figure 6.13 shows the forces in X- and Y- direction. In X-direction the mean forces for 2 and 3 m/s are comparable and fluctuating around zero. This is expected, the bodies are symmetrical in X-direction. The system is asymmetrical in Y-direction, which corresponds well to the negative forces obtained in the CFD analysis. The forces for 3 m/s show larger fluctuations compared to 2 m/s, which can be explained by the flow regimes as shown in Figure 3.12. At a higher velocity, the vortex street is re-establishes, which could result in larger fluctuations in the forces.

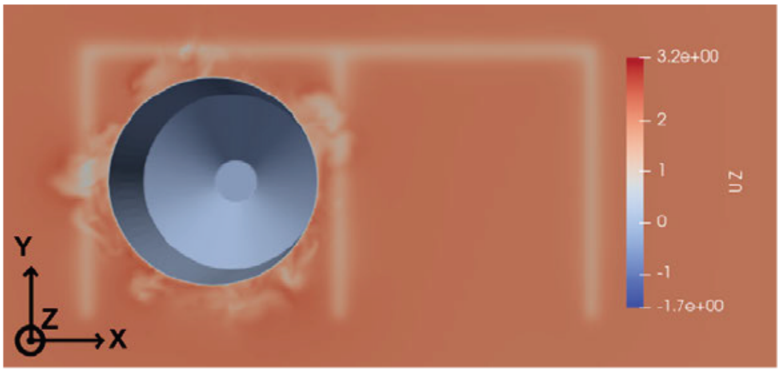

Figure 6.12: Undisturbed flow field for lowering the container and cursor frame at 2 m/s at [redacted]

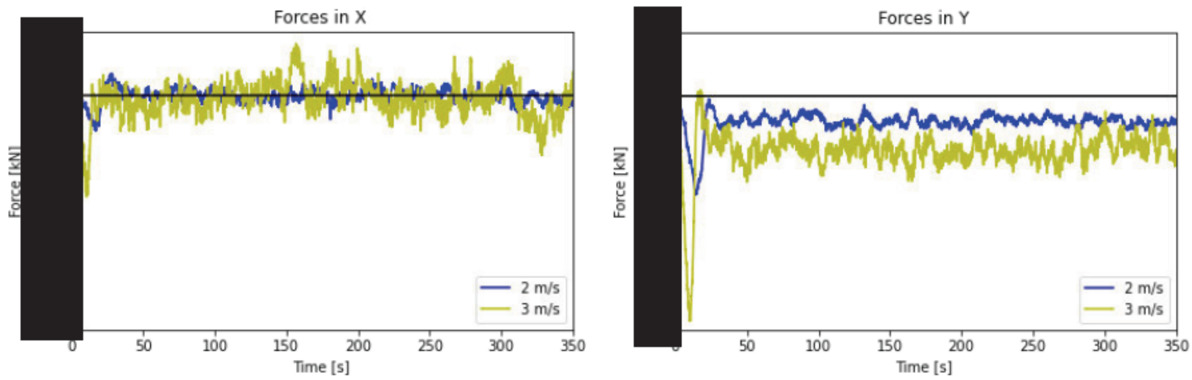

(a)

(b)

Figure 6.13: Forces in X-direction (a) and Y-direction (b) for lowering at 2 and 3 m/s.

Figure 6.14 shows the forces in X- and Y-direction split between the container and cursor frame, which shows that the high frequency oscillations are caused by the cursor frame and the low frequency oscillations by the container. This corresponds well with the vortex shedding periods for the cursor, calculated in the analytical analysis in Section 3.7, which is in the order of 0.4 to 0.5 s. Fluctuations in the forces at the container with lower frequencies are expected, as the container is much larger compared to the cursor and the flow is disorganised.

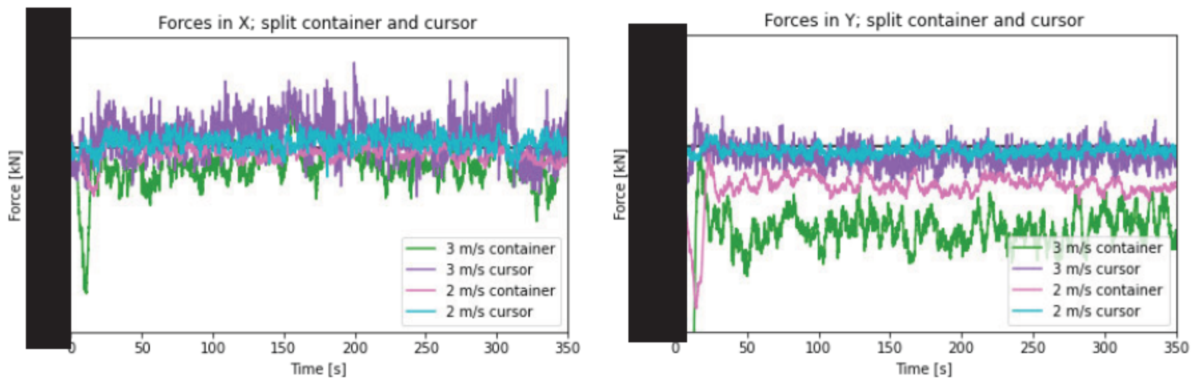

(a)

(b)

Figure 6.14: Forces in X-direction (a) and Y-direction (b) for lowering at 2 and 3 m/s split in the forces at the container and the cursor frame.

Figure 6.15 shows the moments around the X- and Y-axis. The higher velocity of 3 m/s shows larger moments and fluctuations compared to 2 m/s. This has already been seen in the forces in Figure 6.13 and is therefore expected. The sign of the moments correspond well with the analytical results from Table 3.6. [redacted]

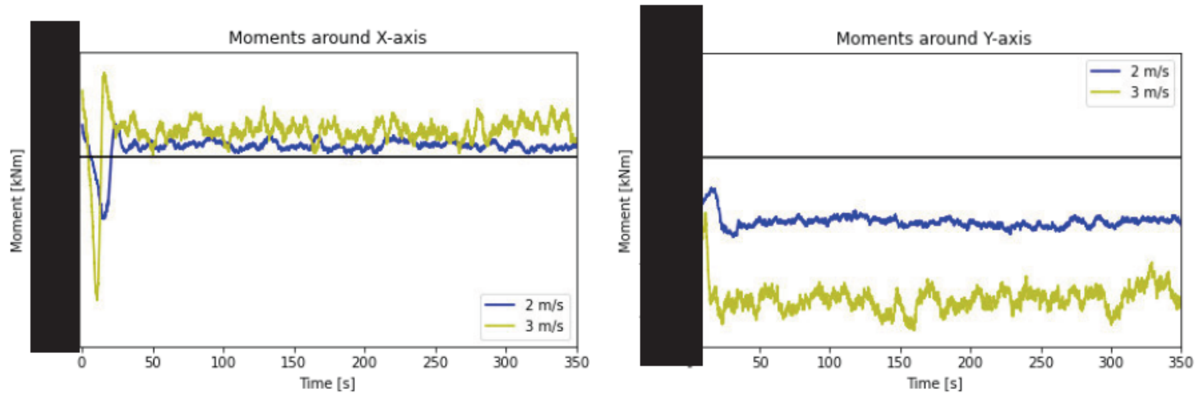

(a) (b)

Figure 6.15: Moments around the X-axis (a) and Y-axis (b) for lowering at 2 and 3 m/s.

Figure 6.16 shows the moments around the X- and Y-axis, split between the moments at the container and at the cursor frame. The container causes a negative moment around the X-axis, while the cursor frame causes a positive moment. Both are due to the asymmetrical cursor. Around the Y-axis the moment is almost fully caused by the cursor frame. The moments at the container are zero, as the cursor exists on both sides of the container and therefore the sum of the moments at the container is zero.

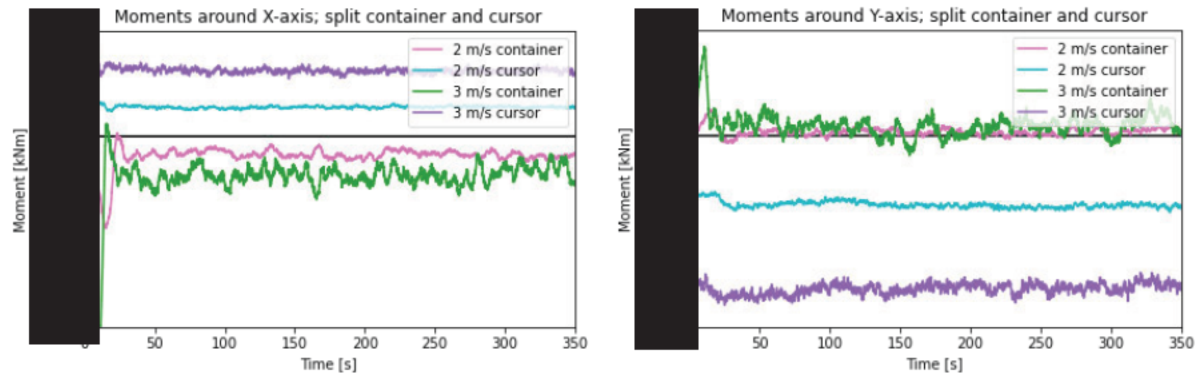

(a) (b)

Figure 6.16: Moments around the X-axis (a) and Y-axis (b) for lowering at 2 and 3 m/s with the total moments split into the container and cursor.

In Figure 6.17 the moments around the Z-axis, the yawing moments, are shown. Both cases show fluctuations with high frequencies, but also fluctuations with lower frequencies are visible. As the lower frequencies could be at or near the natural frequency of the system, a spectral analysis must be performed. This is carried out in Chapter 7.

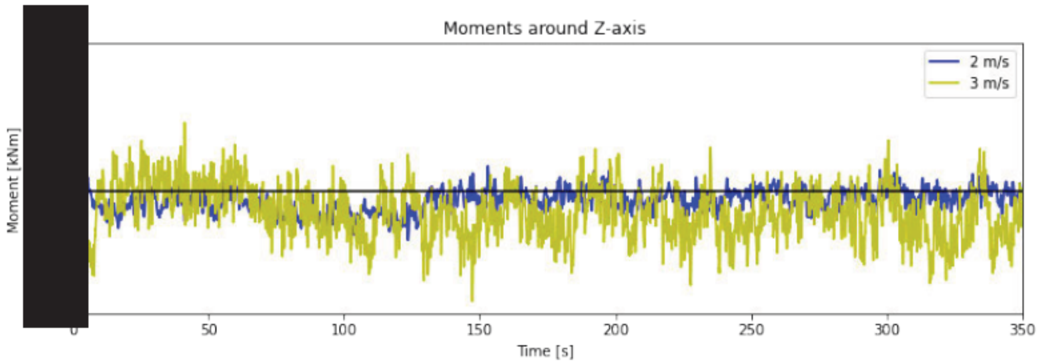

Figure 6.17: Moments around the Z-axis for lowering at 2 and 3 m/s.

The mean and maximum yawing moments are converted to yaw rotations. Figure 6.18a and Figure 6.18b show the static rotation corresponding to the mean and maximum yawing moment at a transportation velocity of 2 m/s. The mean and maximum rotations are both small and well below the safety limit of 45°. Figure 6.18c and Figure 6.18d correspond to lowering at 3 m/s. The yaw rotations are significantly larger compared to 2 m/s. However, this is a static evaluation with no damping included and the rotations are below the limit of 45°.

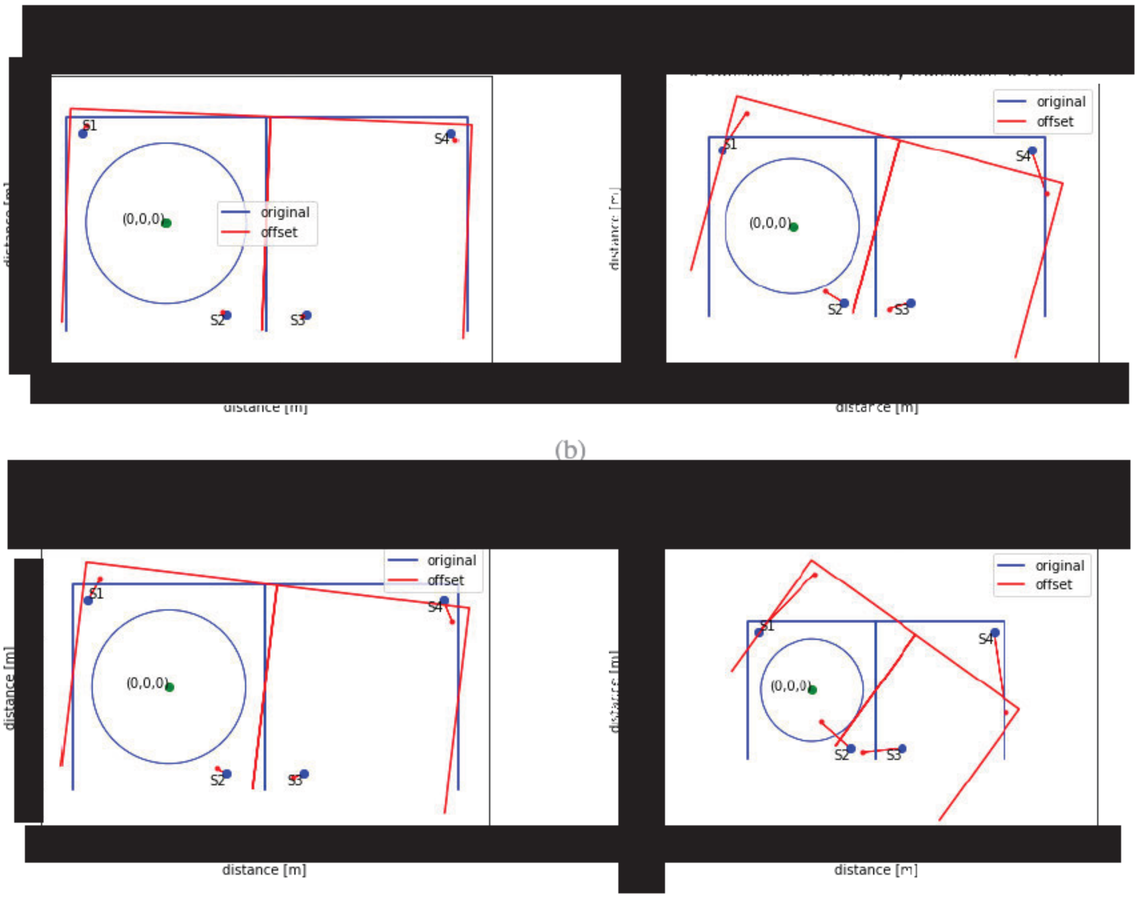

(a) (b)

(c) (d)

Figure 6.18: Mean (a) and maximum (b) rotation around the Z-axis for lowering at 2 m/s and the mean (c) and maximum (d) rotation around the Z-axis for lowering at 3 m/s.

6.5.1. Verification lowering

The simulations start at standstill and therefore transition time is needed to exclude the effects of the building flow field. In all figures these effects are clearly visible in the first 40 seconds. The simulations are validated by plotting the Courant numbers and the residuals. The figures are shown in Appendix J.1 and J.2. For both cases, lowering at 2 and 3 m/s, the Courant numbers are below or near 1 and the residuals have converged.

The result of the CFD simulations and the values from the analytical analysis from Chapter 3 are summarised in Table 6.3.

Table 6.3: Summary of the results of the CFD simulations together with the analytically calculated values for lowering at 2 and 3 m/s.

[redacted]

[redacted] Result lowering inclined including current

Due to the drag and weight, during transportation the system converges to a pitch and roll angle. In the analytical analysis the roll and pitch angles are calculated, summarised in Table 3.6. These values are summarised in Table 6.4 and 6.5 under the column $\theta_{calculated}$. However, the roll and pitch moments due to drag around the X- and Y-axis from the CFD simulations differ from the analytical calculations, as shown in Table 6.3. Therefore, the roll and pitch angles are adjusted to the values under the column $\theta_{updated}$ in Table 6.4 and 6.5.

Besides roll and pitch, the next simulations account for the current with a velocity of 0.1 m/s that acts on the system. The current is integrated by adding an extra roll angle, as shown by Figure 6.19.

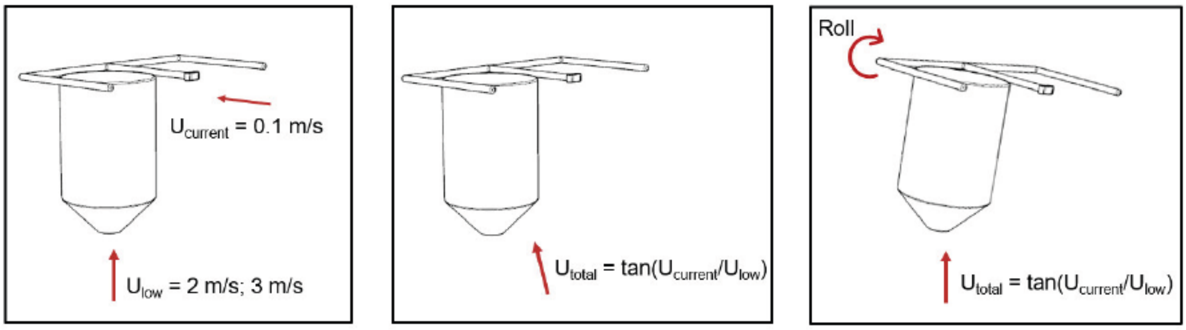

(a) (b) (c)

Figure 6.19: Integration of the current in the simulation with the overview in (a), the result of adding the forces together in (b) and the situation used in the CFD simulations.

Figure 6.19a shows the velocity due to lowering and the current acting on the system. Figure 6.19b shows the result of adding the two flows together and Figure 6.19c shows the system after a roll rotation.

The velocity in Z-direction is adjusted to account for the current. The roll angle to account for the current is summarised in Table 6.4 and 6.5 under the column $\theta_{current}$. As the axis system should not move due to the current, this is accounted for afterwards by translating the forces and moments back to the coordinate system of this thesis, as shown in Figure 2.5. For the forces this is done by the equations

$$\begin{aligned} F_{X,real} &= F_{X,CFD}, \\ F_{Y,real} &= F_{Y,CFD} \cdot \cos(\theta_{current}) - F_{Z,CFD} \cdot \sin(\theta_{current}), \\ F_{Z,real} &= F_{Z,CFD} \cdot \cos(\theta_{current}) + F_{Y,CFD} \cdot \sin(\theta_{current}), \end{aligned} \tag{6.7}$$

with
F_{real} as the forces in the correct axis system [kN],
F_{CFD} as the forces from the CFD simulations [kN],
$\theta_{current}$ as the roll rotation to account for the current [deg].

For the moments this is done by the equations

$$\begin{aligned} M_{X,real} &= M_{X,CFD}, \\ M_{Y,real} &= M_{Y,CFD} \cdot \cos(\theta_{current}) - M_{Z,CFD} \cdot \sin(\theta_{current}), \\ M_{Z,real} &= M_{Z,CFD} \cdot \cos(\theta_{current}) + M_{Y,CFD} \cdot \sin(\theta_{current}), \end{aligned} \tag{6.8}$$

with
M_{real} as the moments in the correct axis system [kNm],
M_{CFD} as the moments from the CFD simulations [kNm].

The roll and pitch angle used in the CFD simulations are defined in the column θ_{total} in Table 6.4 for 2 and in Table 6.5 for 3 m/s, which is the sum of $\theta_{updated}$ and $\theta_{current}$.

Table 6.4: Summary of the roll, pitch and yaw angles for lowering at 2 m/s.

[redacted]

[redacted]

[redacted]

Figure 6.20 shows the snapshots of the flow field around the system along the X-axis and Y-axis lowering at 2 m/s. Here the inclined position is clearly visible. Comparing to the system without roll and pitch in Figure 6.7, shows that along the X-axis the large eddies now develop on one side of the container, due to the pitch angle. At the other side the flow field is less disturbed. Along the Y-axis the smaller eddies develop on both sides of the container. This could be due to the roll being small. However, it could also be the effect of the current that acts in positive Y-direction and reduces the size of the eddies.

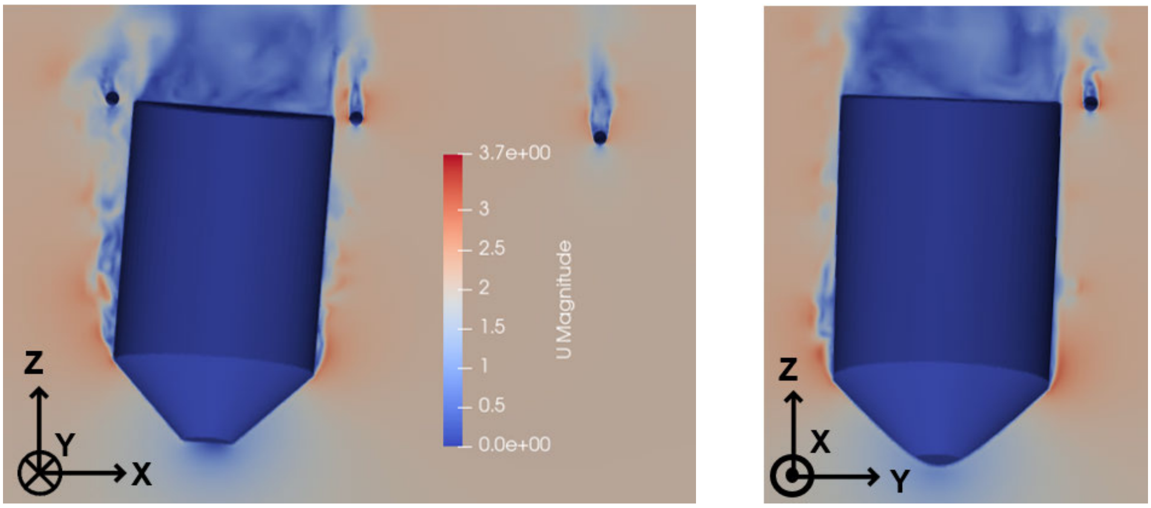

(a) (b)

Figure 6.20: Flow field around the container and cursor frame along the X-axis (a) and Y-axis (b) at 2 m/s including roll, pitch and the current.

Figure 6.21 shows the snapshot of the flow field when lowering at 3 m/s with the inclined system and including the current.

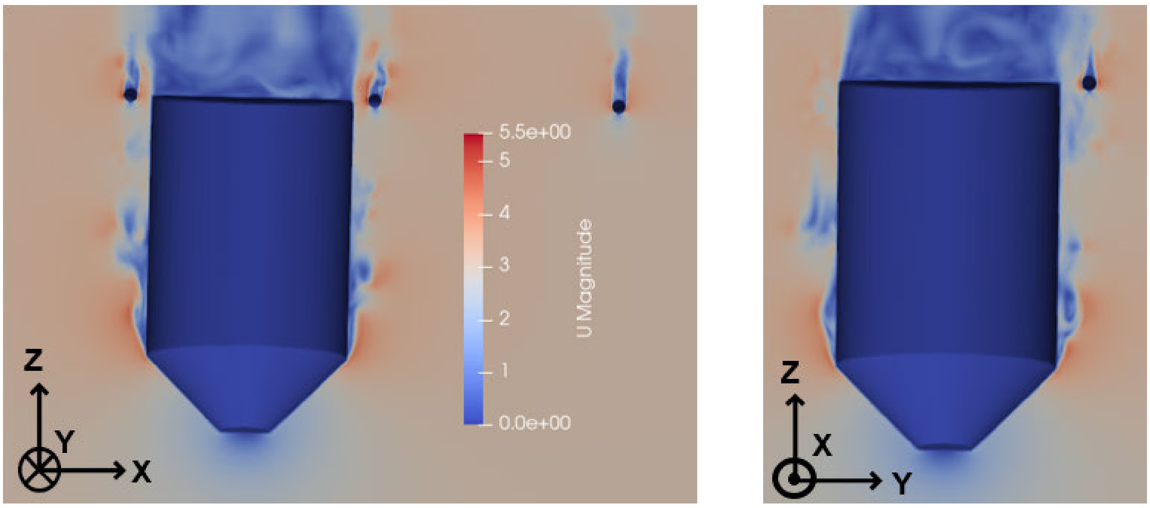

(a) (b)

Figure 6.21: Flow field around the container and cursor frame along the X-axis (a) and Y-axis (b) at 3 m/s including roll, pitch and the current.

Figure 6.22 shows the forces in Z-direction and corresponding force coefficients for the simulations. The forces have increased compared to Figure 6.9, which is expected as the reference area is larger in the new simulations, due to the roll and pitch angles.

Figure 6.31 shows the forces in the X- and Y-direction. A mean negative force in X-direction is visible, which is due to included pitch. In Y-direction the forces have changed little compared to Figure 6.13, which is expected. In the analytical analysis the force in Y-direction due to the current was calculated to be [redacted] meaning that the current has relatively little effect on the system. The force in Y-direction has increased slightly, which is therefore due to the included roll rotation.

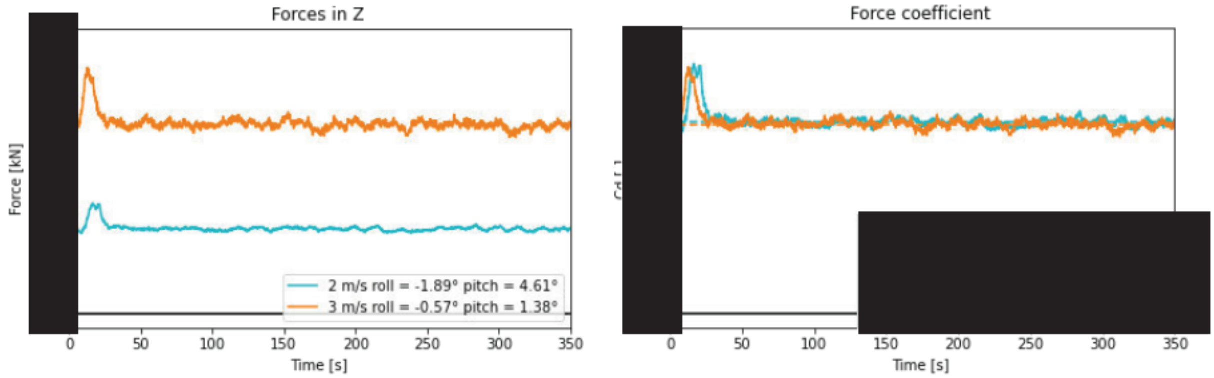

(a) Forces in Z

(b) Force coefficients

Figure 6.22: Forces in Z-direction (a) and corresponding force coefficients (b) for lowering at 2 and 3 m/s with an inclined system.

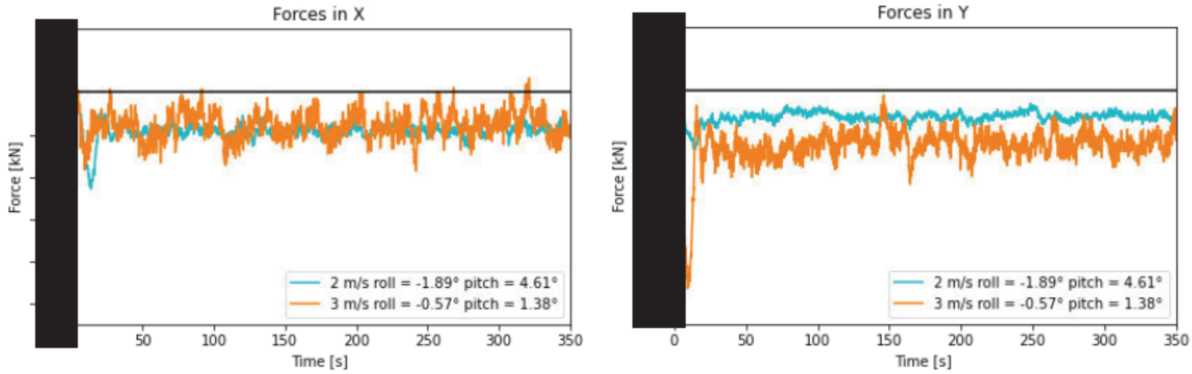

(a)

(b)

Figure 6.23: Forces in X-direction (a) and Y-direction (b) for lowering at 2 and 3 m/s with an inclined system.

The moments around the X- and Y-axis are shown in Figure 6.24.

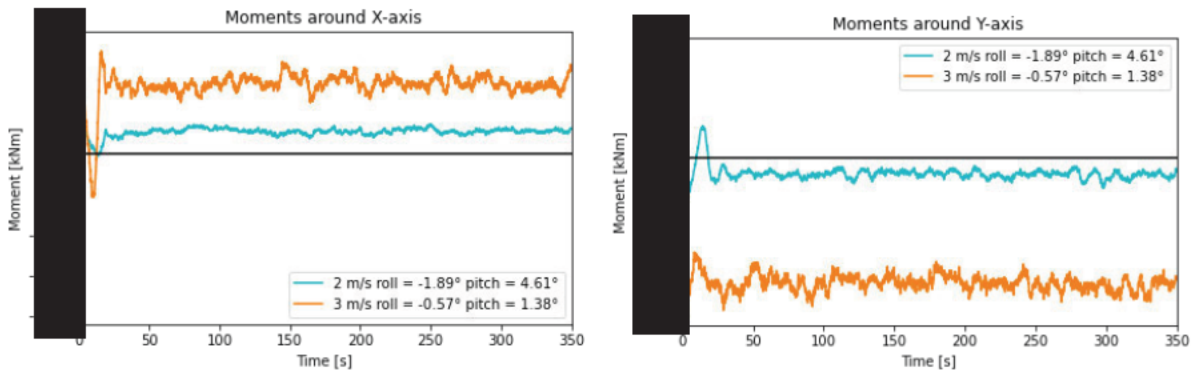

(a)

(b)

Figure 6.24: Moments around the X-axis (a) and Y-axis (b) for lowering at 2 and 3 m/s with an inclined system.

The moments around the Z-axis, the yawing moments, are shown in Figure 6.25. A large increase in the simulation for 3 m/s is noticeable, resulting in yawing moments of [redacted] which exceeds the safety limit of [redacted]. The obtained yawing moments for 2 m/s are well within the limit.

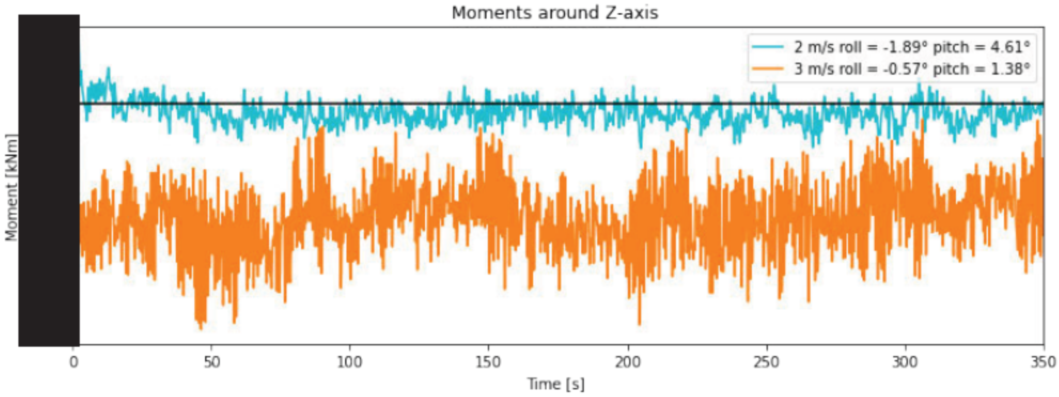

Figure 6.25: Moments around the Z-axis for lowering at 2 and 3 m/s with an inclined system.

The mean yawing moments for both cases are converted to static rotations. Figure 6.26 shows the result. The static yaw rotation for lowering at 2 m/s is small. However, the yaw rotation corresponding to the mean yawing moment for lowering at 3 m/s is 40°. Including the fluctuations, the static yaw rotation increases, which exceeds the safety limit. Therefore, based on a static evaluation, lowering with 3 m/s is not possible.

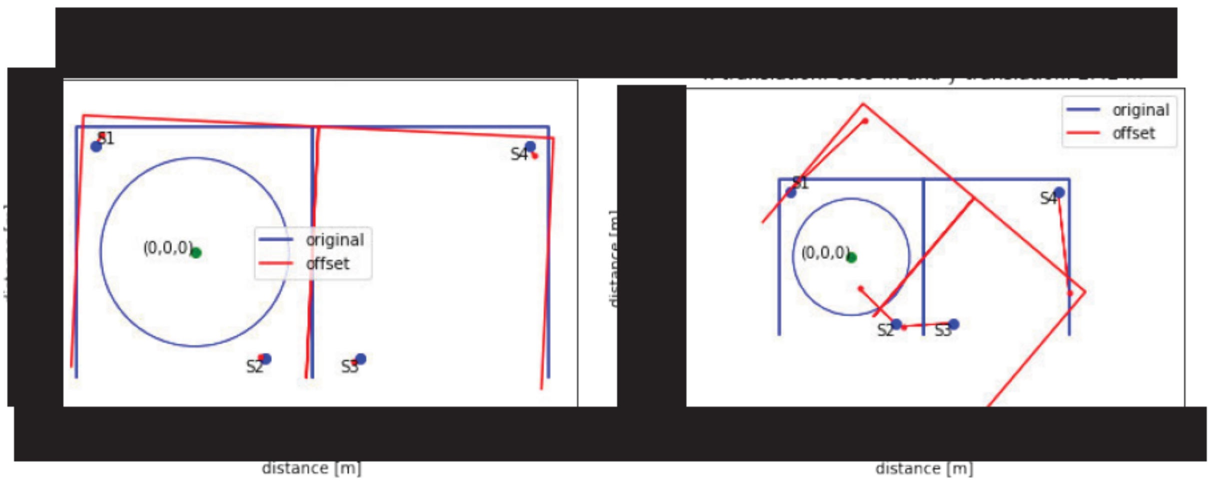

(a) (b)

Figure 6.26: Mean rotation around the Z-axis for lowering at 2 m/s (a) and 3 m/s (b).

6.6.1. Verification lowering inclined including current

The verification graphs of the Courant number and the residuals can be found in Appendix J.3 and J.4. For both cases, lowering at 2 and 3 m/s with an inclined system, the Courant numbers are below or near 1 and the residuals have converged.

Table 6.6 shows a summary of the obtained values from the CFD analysis.

Table 6.6: Summary of the results of the CFD simulations for lowering at 2 and 3 m/s with an inclined system.

[redacted]

6.7. Results hoisting

The final CFD simulation for full scale is hoisting at 2 m/s, corresponding to Figure 6.5. The mesh shown in Figure 6.27, which is similar to lowering, except for the refinement box for the wake that is now at the bottom of the container. The domain is [redacted] with five refinement levels leading to 3,178,586 cells, 48,176 faces at the container and 46,005 faces at the cursor. In the simulation for hoisting the flow has a velocity of 2 m/s. The system has no pitch and roll and the current is excluded.

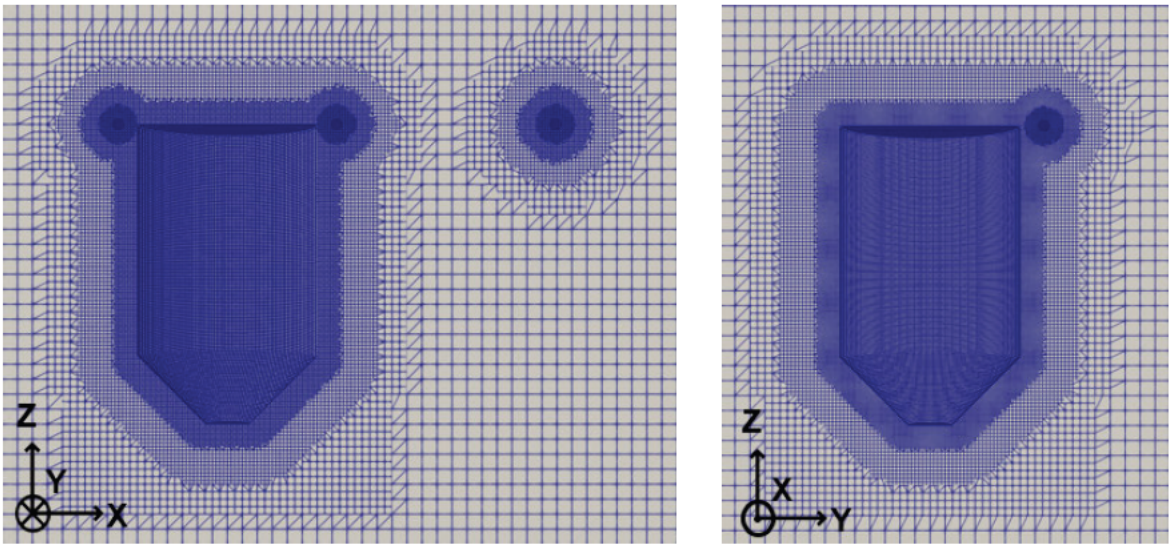

(a) (b)

Figure 6.27: Mesh for hoisting the container with cursor frame along the X-axis (a) and Y-axis (b).

Figure 6.28 shows the snapshots of the flow field around the system along the X and Y-axis when hoisting at 2 m/s. Compared to the flow fields for lowering in Figure 6.7, 6.8, 6.20 and 6.21, the flow field for hoisting is more disturbed due to the flat top of the container.

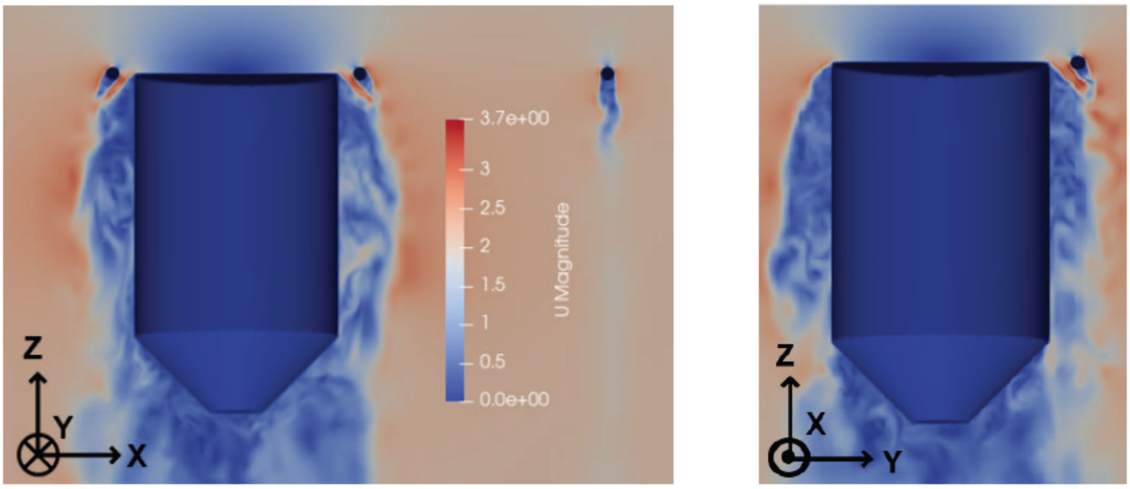

(a) (b)

Figure 6.28: Flow field around the inclined container and cursor frame along the X-axis (a) and Y-axis (b) at 2 m/s.

The forces in Z-direction and the corresponding force coefficients are shown in Figure 6.29. For the full system a rather constant force coefficient of [redacted].

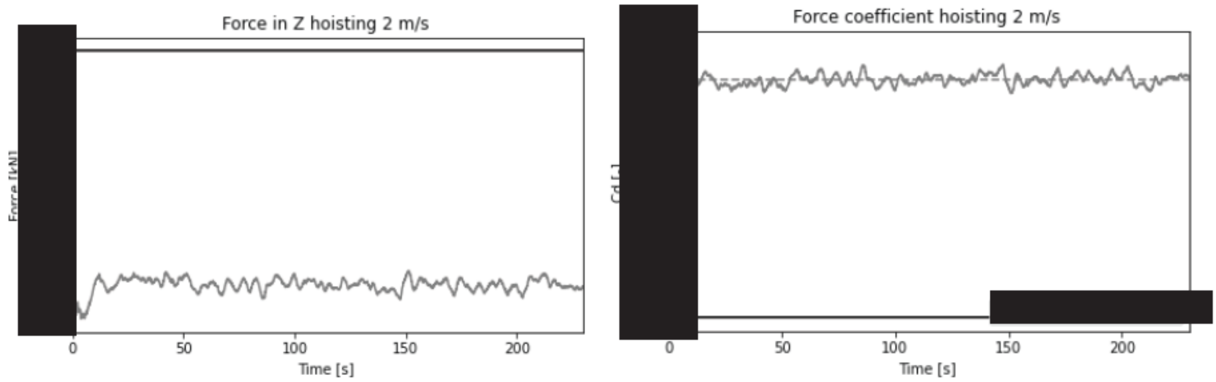

(a) (b)

Figure 6.29: Forces in Z-direction (a) and corresponding force coefficients (b) for hoisting at 2 m/s.

[redacted]

The difference in the force coefficient for the cursor frame between the CFD simulation and the analytical analysis, can be explained by the flow field in Figure 6.28. Although the flow field is less disturbed when reaching the cursor frame compared to lowering, the flow field is influenced by the container resulting in a lower flow velocity near the cursor frame. Therefore, the force in Z-direction and thus the force coefficient is lower.

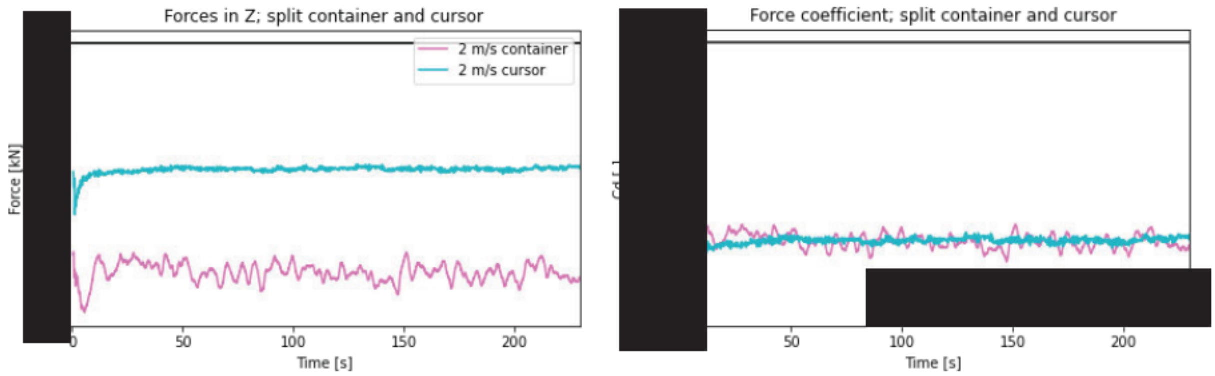

(a) (b)

Figure 6.30: Forces in Z-direction (a) and force coefficients (b) for hoisting at 2 m/s split in the forces at the container and cursor frame.

Figure 6.31a shows the forces in the X- and Y-direction. Both forces are oscillating with a relatively small negative mean force. Comparing to lowering at 2 m/s without roll, pitch and current, shows that hoisting at 2 m/s gives a smaller force in Y-direction, which is due to the flow reaching the cursor first.

[redacted]

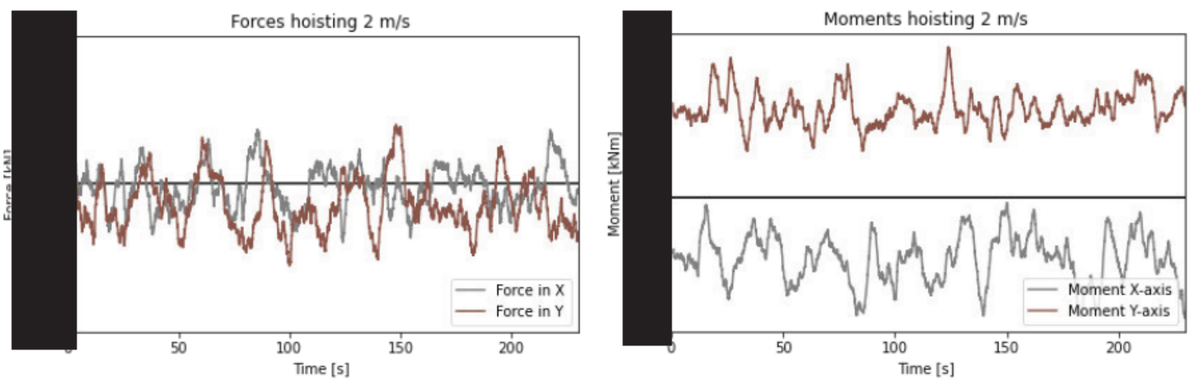

(a) (b)

Figure 6.31: Forces in X- and Y-direction (a) and moments around the X- and Y-axis (b) for hoisting at 2 m/s.

The moment around the Z-axis is shown in Figure 6.32. The mean moment is [redacted] is well below the safety limit of [redacted] The magnitude of the fluctuations with low frequencies are smaller compared to the lowering operation.

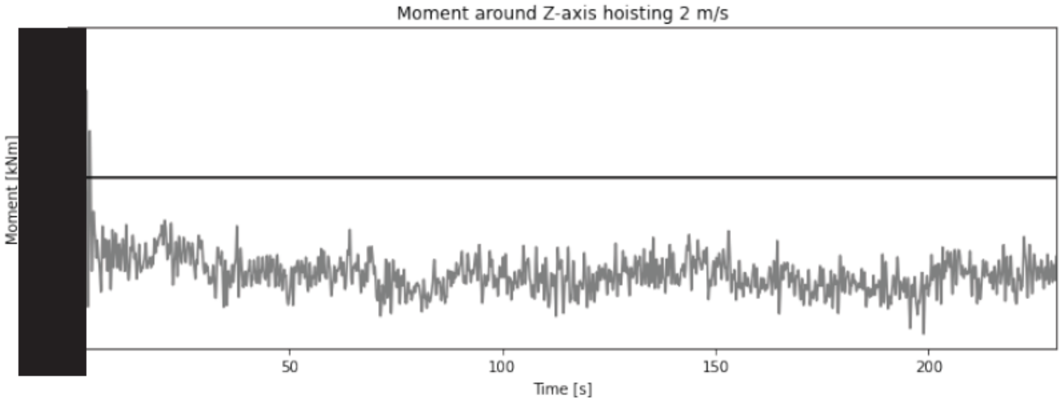

Figure 6.32: Moments around the Z-axis for hoisting at 2 m/s.

The mean and maximum yawing moments are converted to static yaw rotations as shown in Figure 6.33, which are both well below the safety limit of 45°.

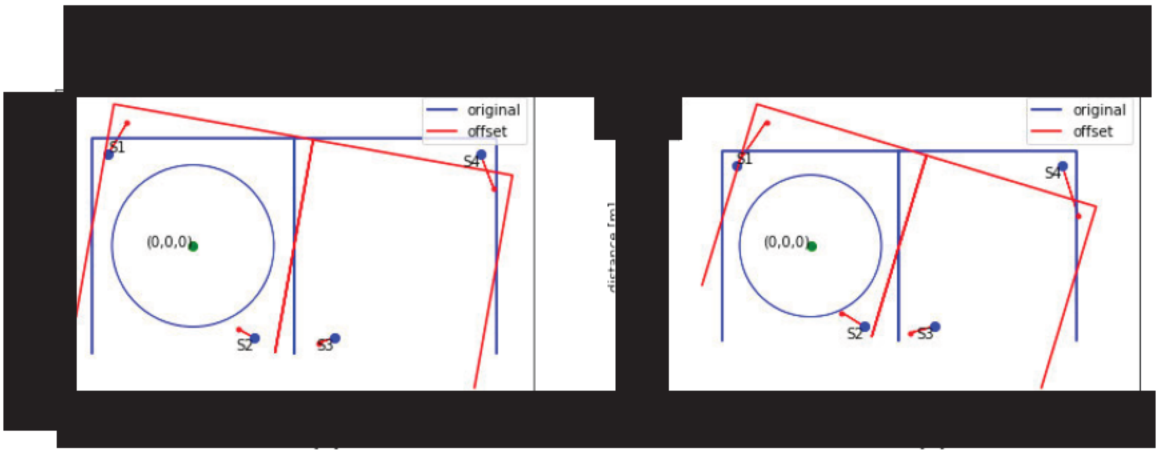

(a) (b)

Figure 6.33: Mean (a) and maximum (b) rotation around the Z-axis for hoisting at 2 m/s.

6.7.1. Verification hoisting

The verification graphs of the Courant number and the residuals can be found in Appendix J.5. The Courant number is below 1 and the residuals have converged. Therefore, the simulation is verified.

The result of the CFD simulations compared to the calculated values from Chapter 3 are summarised in Table 6.7.

Table 6.7: Summary of the results of the CFD simulation together with the analytically calculated values for hoisting at 2 and 3 m/s.

[redacted]

7 Discussion

The objective of the discussion is to quantify the response of the container and cursor frame due to the yawing moment induced during transportation and argue whether the guidance wires can provide enough restoring to obtain safe transport. The discussion consists of a presentation of the static response of the container and cursor frame, a spectral analysis, a presentation of the dynamic response which includes dynamic amplification, and a comparison between the CFD simulations and the experiment and an overview of the energy consumption. Figure 7.1 shows a summary of the yawing moments obtained with the CFD analysis. Hoisting shows a shorter signal, as the simulation is run only until t = 230 s due to computational power.

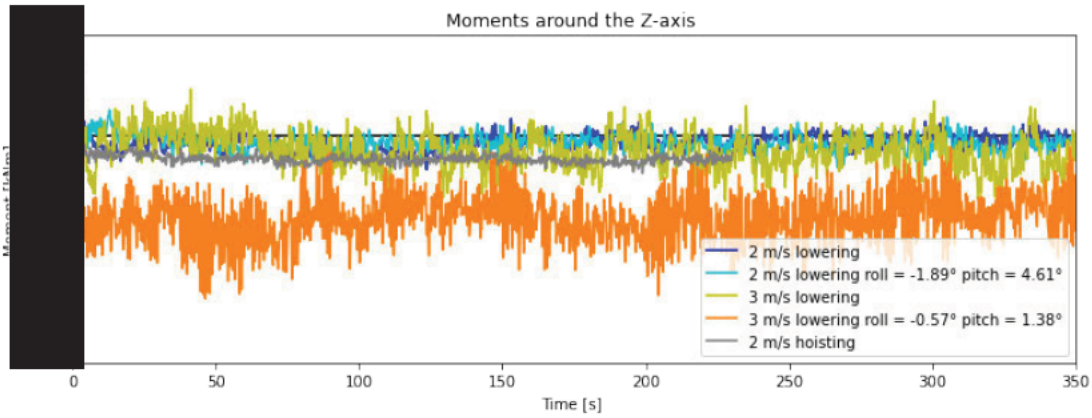

Figure 7.1: Summary of the yawing moments from the CFD simulations.

The probability distributions of the yawing moments are presented in Figure 7.2.

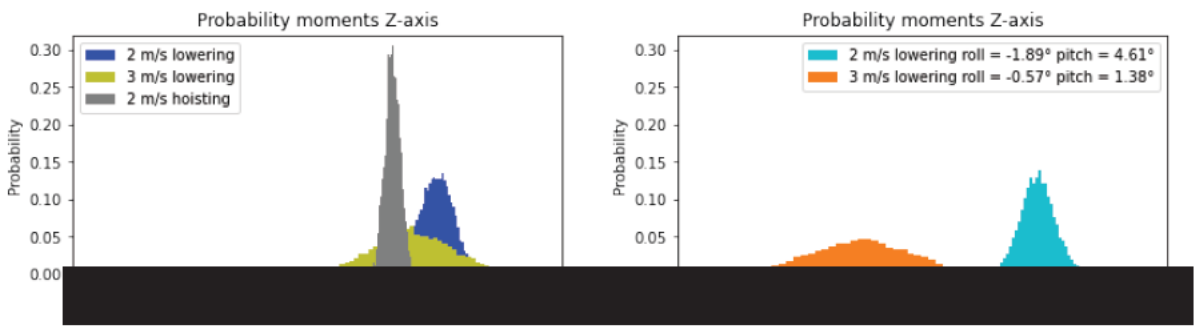

(a) (b)

Figure 7.2: Probability distributions with 60 bins of the yawing moment for zero roll, pitch and current (a) and the inclined system with current (b) for hoisting and lowering.

The higher magnitude fluctuations for 3 m/s compared to 2 m/s are clearly noticeable in the probability distributions. All simulations show a negative mean yawing moment, with a significantly larger mean value for the 3 m/s simulation with roll, pitch and current. The fluctuations for hoisting are smaller in magnitude compared to lowering. This can be explained by the location of the cursor frame. As shown in Figure 6.7, the flow passing the container contains large eddies resulting in a disturbed flow field that moves towards the cursor. While hoisting, the flow hits the cursor first, as shown in Figure 6.28, resulting in smaller fluctuations. Lowering at 3 m/s shows larger fluctuations compared to lowering at 2 m/s, as the flow has a higher Reynolds number.

The yawing moments for all simulations are separated into the yawing moment at the container and the yawing moment at to cursor frame. Figure 7.3 shows the yawing moment at the container and Figure 7.4 shows the yawing moment at the cursor frame, from which can be concluded that the yawing moment is almost fully caused by the cursor frame.

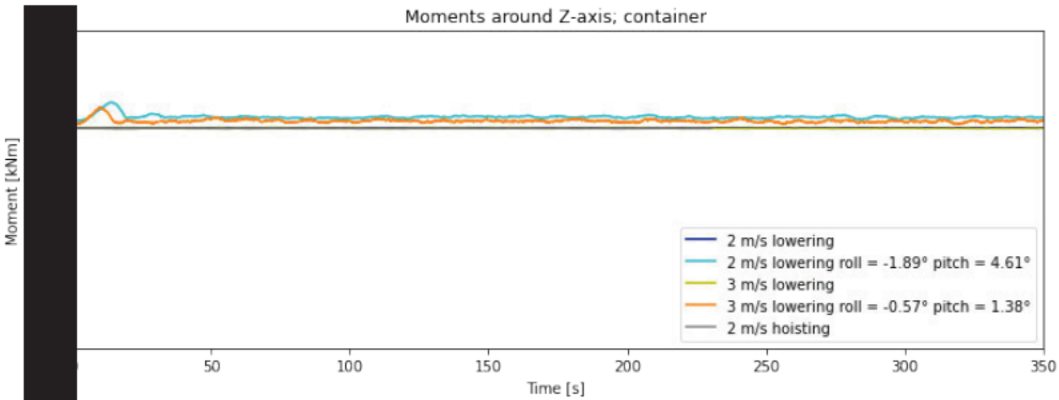

Figure [redacted]Moments around Z-axis at the container for all CFD simulations.

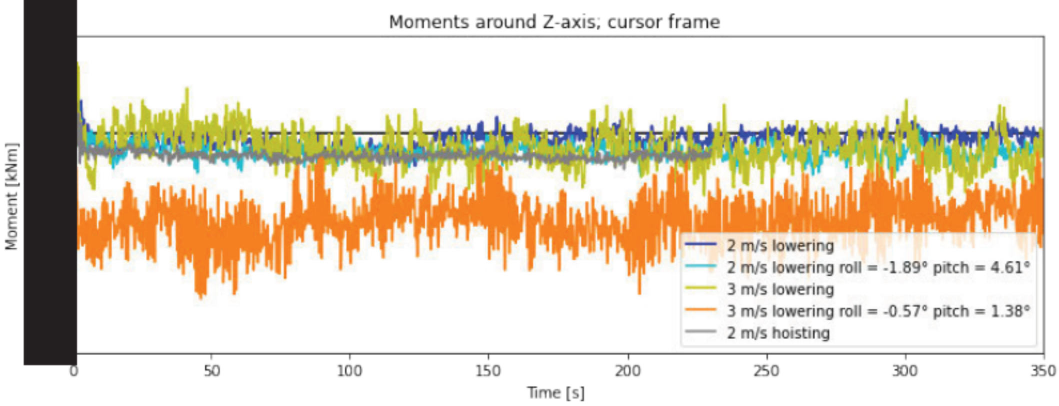

Figure 7.4: Moments around Z-axis at the cursor frame for all CFD simulations.

7.1. Static response: translation and rotation

The static responses at d = -2750 m, consisting of translation and rotation, for the lowering situations from Figure 7.1 are presented in Figure 7.5 and 7.6. The mean values for the forces and moments are used. The rotations are well below the limit of 45°. The X- and Y-translations are relatively small and therefore no showstopper. The situation of lowering at 3 m/s with an inclined system and including current shows the largest response, closest to the safety limit, and is therefore further investigated.

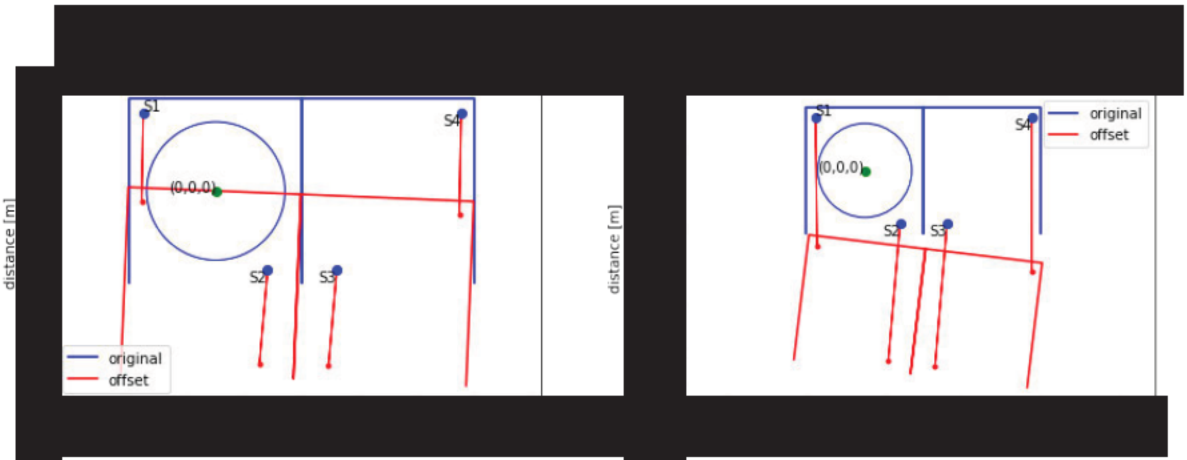

(a) (b)

Fig[redacted]7.5: Total excitation for lowering with no roll, pi[redacted]d current at 2 m/s (a) and 3 m/s (b).

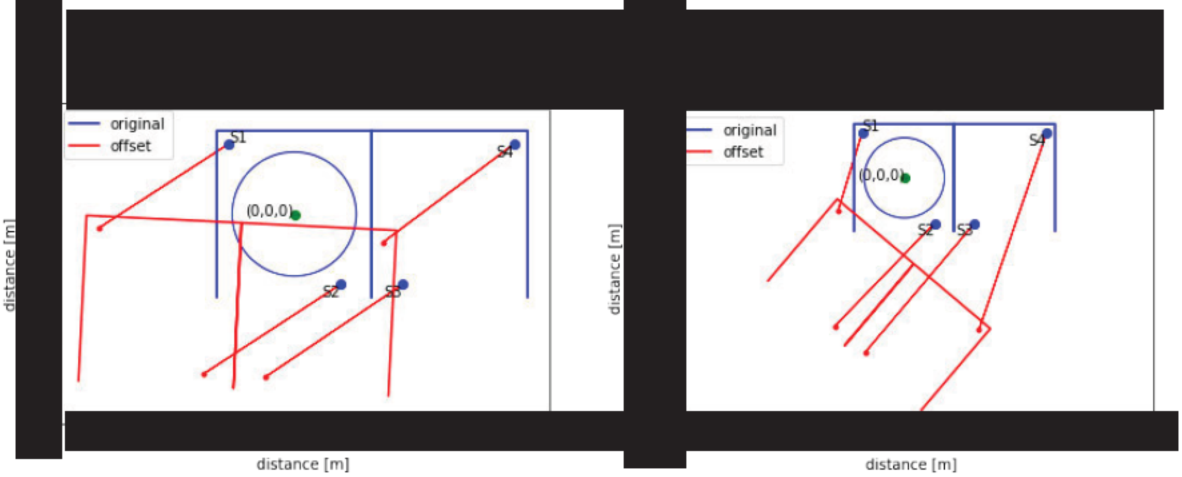

(a) (b)

Figure 7.6: Total excitation for lowering the inclined system including the current at 2 m/s (a) and 3 m/s (b).

The pressures at the container and cursor are shown in Figure 7.7 and Figure 7.8 shows the cursor only. The pressures at the container and cursor frame are alternating due to eddies, resulting in fluctuations in forces and moments. A difference can be observed between Figure 7.7a and 7.7c. Figure 7.7c shows a higher pressure at the top half of the container compared to Figure 7.7c resulting in a negative force in Y-direction. This is caused by the water decelerating due to the cursor frame, which has a larger effect than the current, as the current would have resulted in a positive force in Y-direction. In Figure 7.7b, compared to Figure 7.7d, the low pressure zone denoted in blue is larger. This is due to the pitch angle, which causes a negative force in X-direction at the container.

Figure 7.8 shows the varying pressures at the cursor frame. At the locations where the container and cursor frame are closest to each other, lower pressures can be found, which are due to the accelerating water.

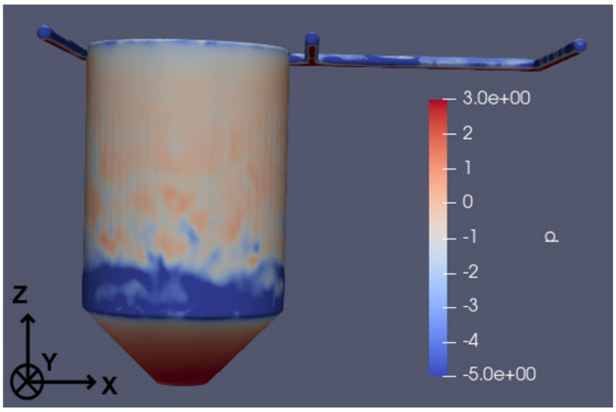

(a)

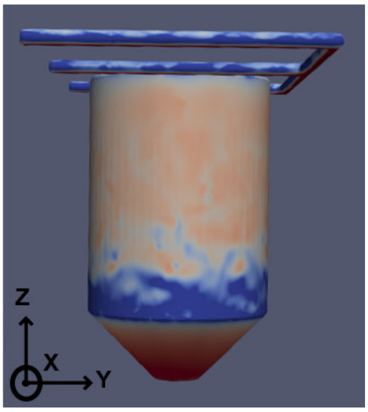

(b)

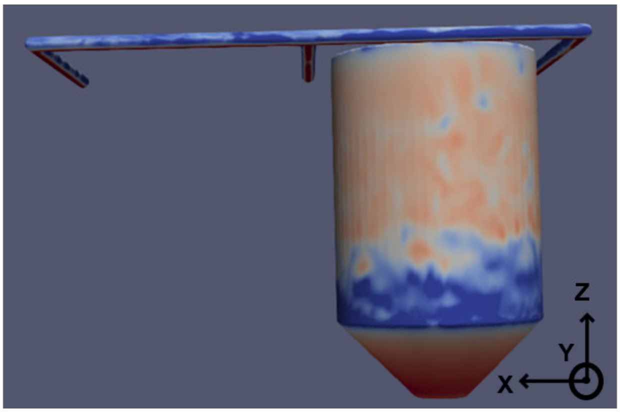

(c)

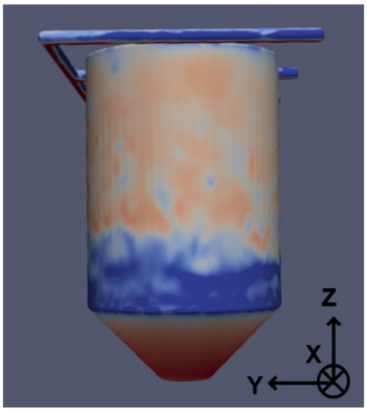

(d)

Figure 7.7: Pressures [Pa] at the system for lowering at 3 m/s including roll, pitch and current.

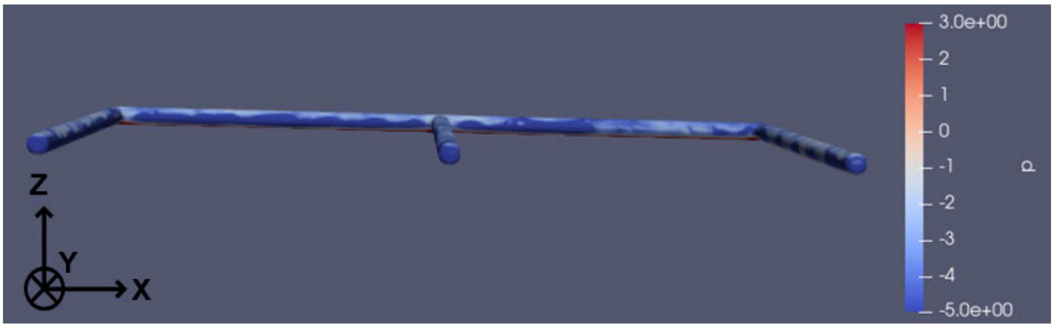

(a)

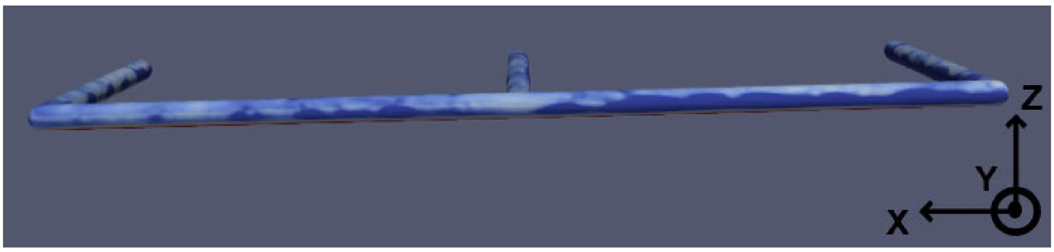

(b)

Figure 7.8: Pressures [Pa] at the cursor frame for lowering at 3 m/s including roll, pitch and current.

The total excitation for hoisting at 2 m/s is presented in Figure 7.9. Again the mean values for the forces and moment are used.

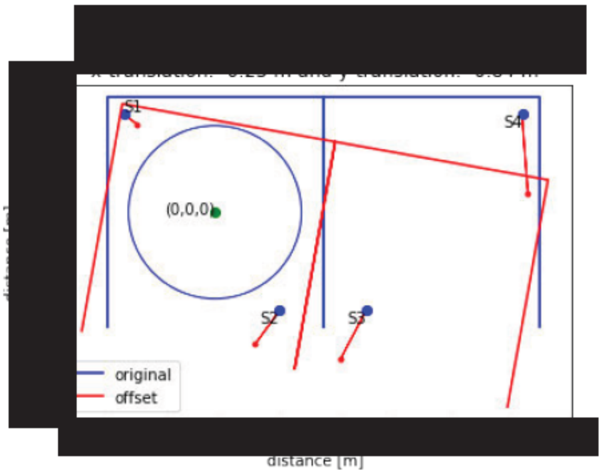

Figure 7.9: Total excitation for hoisting with no roll, pitch and current at 2 m/s.

7.2. Spectral analysis

A spectral analysis is performed to compare the yawing moment frequencies to the eigenfrequencies of the transported system. For the spectral analysis, the CFD simulations for lowering at 2 m/s are extended to be able to average separate sections of the signal. The extended result is visible in Figure 7.10. Lowering with an inclined system shows a shorter signal due to computational constraints. As the flow field needs to build up starting at t = 0 s, the first 40 s are removed from the signals.

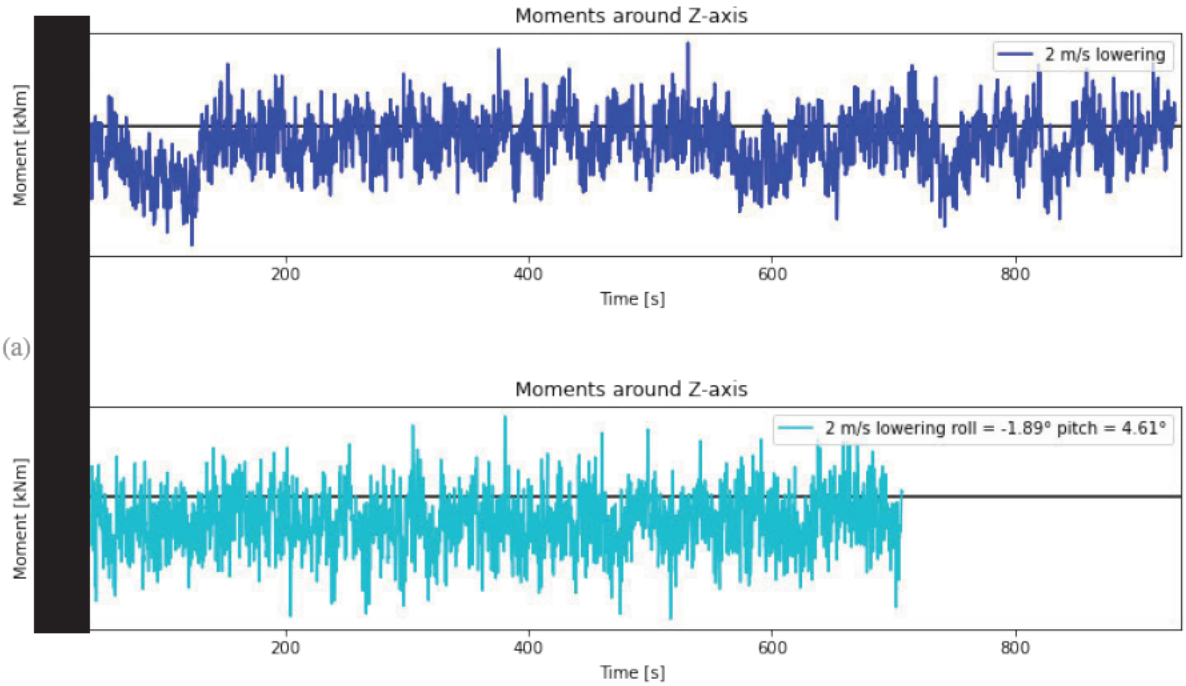

(a)

(b)

Figure 7.10: Moment around the Z-axis for lowering at 2 m/s extended.

Figure 7.11 shows the power spectral density (PSD) spectrum of the moments around the Z-axis. Figure 7.12 shows the PSD for the forces in the X- and Y-direction of both simulations. The time signal is divided into segments by Welch's method [49] and the output spectra are averaged. The simulation for lowering at 2 m/s uses 5 segments and the simulation for lowering at 2 m/s with the inclined system including current uses 4 segments. The eigenfrequency range of the container with cursor frame is indicated with the black dashed and dotted lines. In the frequency spectrum for the moment around the Z-axis, only small peaks can be obtained within the region of the eigenfrequency. The higher peaks are outside the region. However, in the frequency spectrum of the forces in X- and Y-direction, high peaks are obtained in the region of the eigenfrequency, especially for the inclined system. Therefore, resonance can occur.

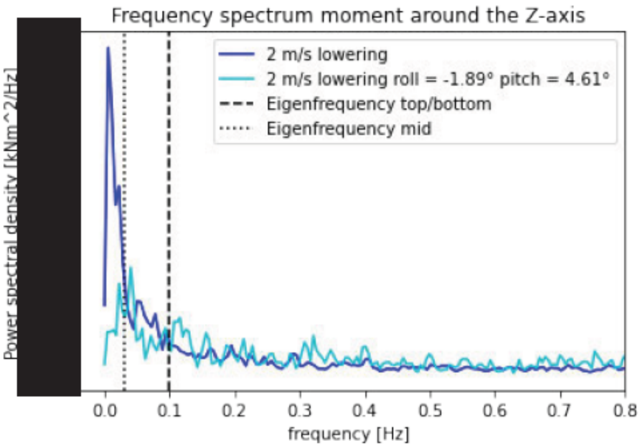

Figure 7.11: Power spectral density spectrum for the moment around the Z-axis obtained by Welch's method [49] including the boundaries of the eigenfrequencies of the system.

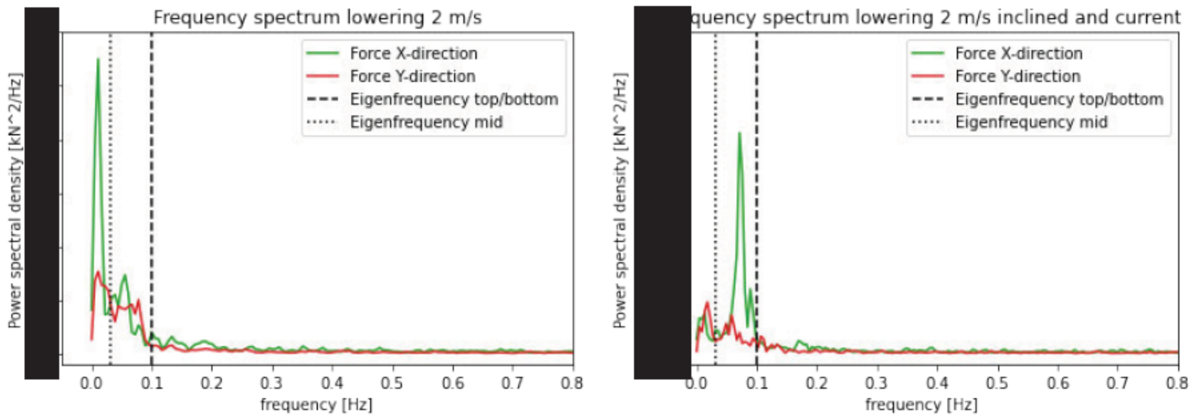

(a) (b)

Figure 7.12: Power spectral density spectrum for the forces in X- and Y-direction for lowering at 2 m/s (a) and lowering at 2 m/s with the inclined system including current (b) obtained by Welch's method [49] including the boundaries of the eigenfrequencies of the system.

7.3. Dynamic response

The dynamic response is calculated for lowering at 2 m/s and lowering with the inclined system and including current at 2 m/s.

7.3.1. Lowering at 2 m/s

The static response of the system to the signal from Figure 7.10 can be calculated by dividing the yawing moment (M_Z) by the rotational stiffness (K_{rot}):

$$\gamma_{static}(d) = \frac{M_Z}{K_{rot}(d)}. \tag{7.1}$$

The rotational stiffness is dependent on the depth, as shown in Figure 3.5b, and therefore the response of the system is dependent on the depth as well. Figure 7.13 shows the static response at various depths. At depths near the top and bottom of the water column the static response is much less compared to in the middle of the water column. The maximum static rotation is [redacted]

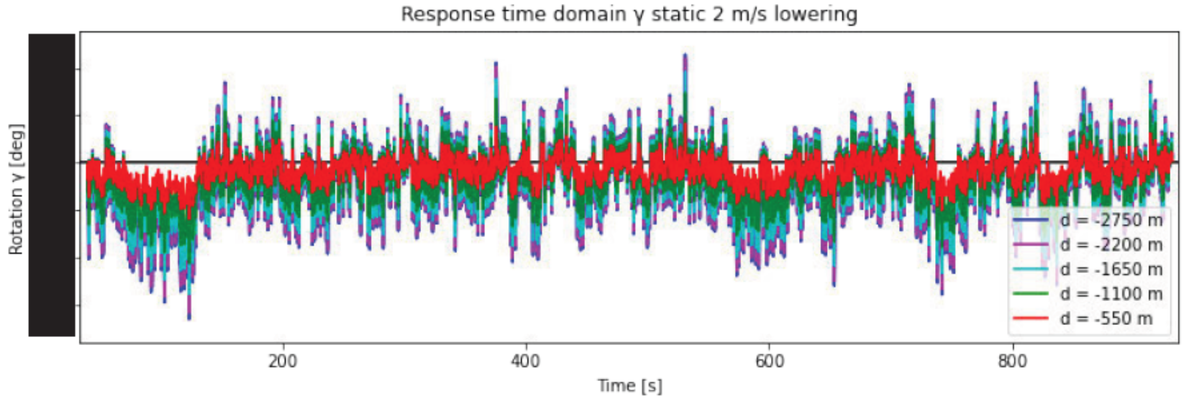

Figure 7.13: Static response of the container and cursor frame to the yawing moment at various depths for lowering at 2 m/s.

The dynamic response of the system can be calculated by multiplying the static response by the dynamic amplification factor (DAF). The dynamic amplification factor is a dimensionless number that describes how much the static response to the yawing moment magnifies, due to the dynamic characteristics including momentum, kinetic energy and damping. The factor is calculated per frequency. The dynamic response is calculated by

$$\gamma_{dynamic} = \gamma_{static} \cdot DAF, \tag{7.2}$$

with
DAF as the dynamic amplification factor [-], for a single degree of freedom system calculated by

$$\begin{gathered} \mathrm{DAF}(d) = \frac{1}{\sqrt{(1-r^2)^2 + (2\zeta r)^2}}, \\ r = \frac{\omega}{\omega_n}, \end{gathered} \tag{7.3}$$

with
ω as the response frequency [Hz],
ω_n as the natural frequency of the system[Hz],
ζ as the damping ratio [-].

The damping ratio can be calculated by dividing the damping of the system by the critical damping:

$$\begin{gathered} \zeta = \frac{c}{c_c}, \\ c_c = 2 \cdot \sqrt{KM} = 2 \cdot \sqrt{K_{rot} \cdot I_{rot}}, \end{gathered} \tag{7.4}$$

with
c as the damping coefficient [kNms/rad],
c_c as the critical damping [kNms/rad],
I_{rot} as the inertia [kg m^2],
K_{rot} as the rotational stiffness [kNm/rad].

The damping coefficient for the system is estimated in the time integration calculation in Chapter 5 as [redacted]. However, this value is an estimation and therefore a sensitivity analysis is performed for a damping coefficient of 50% higher and lower. At various depths, the dynamic amplification factor per frequency is calculated, with the result shown in Figure 7.14a. As the rotational stiffness increases near the top and bottom of the water column, compared to the middle, the damping ratio will decrease near the top and bottom. [redacted]

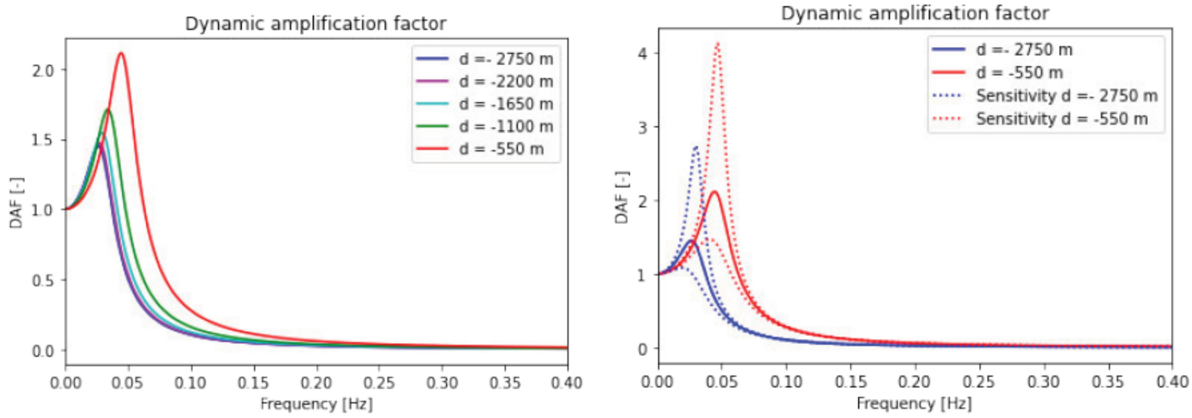

(a) (b)

Figure 7.14: DAF at various depths (a) and the DAF with ± 50 % damping (b).

The frequency spectrum for the static response of the system is shown in Figure 7.15a and for the dynamic response in Figure 7.15b. In the dynamic response, the higher frequencies are filtered out and some lower frequencies are amplified, which corresponds to the dynamic amplification factor.

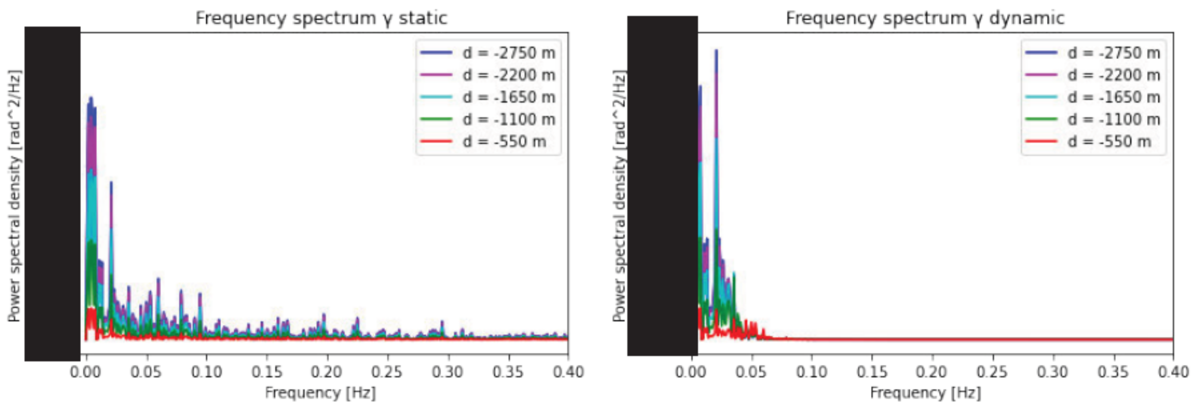

(a) (b)

Figure 7.15: PSD spectrum for the static (a) and dynamic response (a) to the yawing moment at 2 m/s.

The obtained power density spectrum for the dynamic response can be transformed back into a time domain signal. This is shown in Figure 7.16, which shows that the largest excitation appears in the middle of the water column. The higher frequencies are filtered out and the maximum rotation in the middle of the water column has reduced t[redacted]

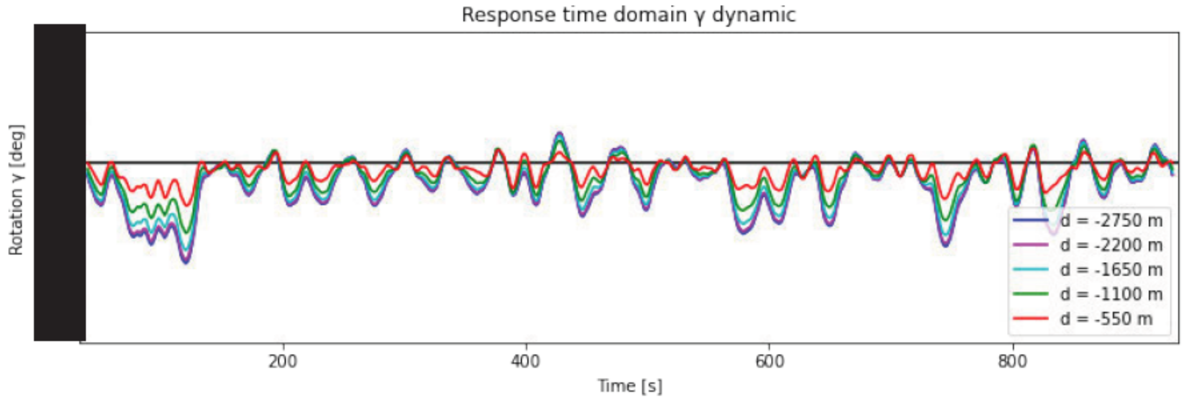

Figure 7.16: Dynamic response at different depths of the system to the yawing moment for lowering at 2 m/s.

Including the 50 to 150 % damping interval for the depths -2750 m and -550 m, the dynamic response is shown in Figure 7.17. The maximum rotation is well below the limit of 45° and thus no issues arise due to the forces that act on the container and cursor frame during lowering at 2 m/s

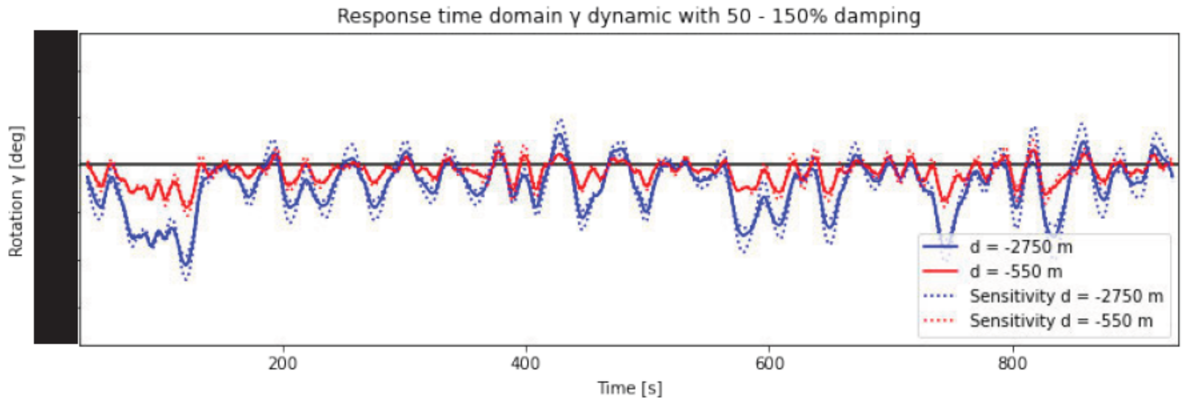

Figure 7.17: Dynamic response of the system to the yawing moment for lowering at 2 m/s with 50 to 150 % damping.

7.3.2. Lowering at 2 m/s with an inclined system including current

The calculation of the dynamic response by using the method described above is performed for the simulation lowering at 2 m/s with an inclined system and including current. The static and the dynamic response are shown in Figures 7.18 and 7.19. From the figures the same conclusion can be drawn as for lowering at 2 m/s without roll, pitch and current. The maximum rotation is well below 45° and operating is therefore within the safety limit. Dynamic amplification does not result in larger rotations and in the middle of the water column the largest rotation occurs.

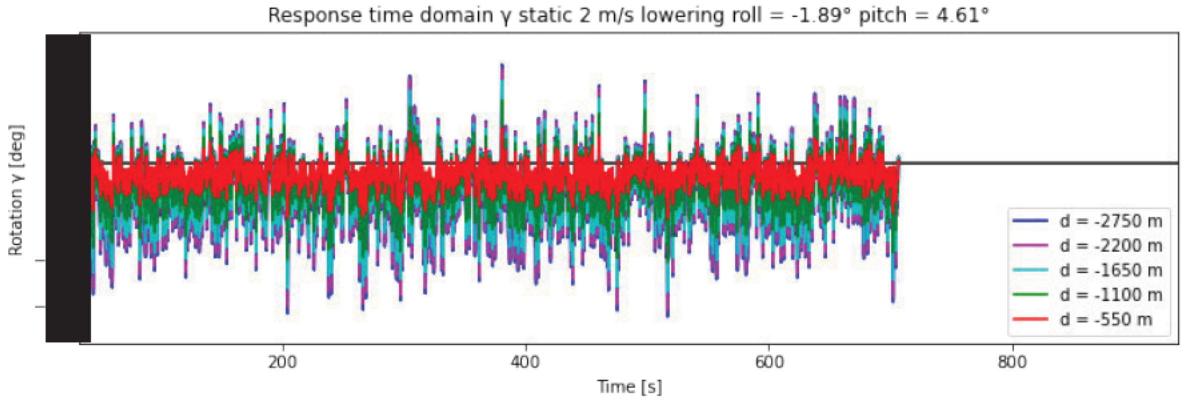

Figure 7.18: Static response of the container and cursor frame to the yawing moment at various depths for lowering at 2 m/s with roll, pitch and current.

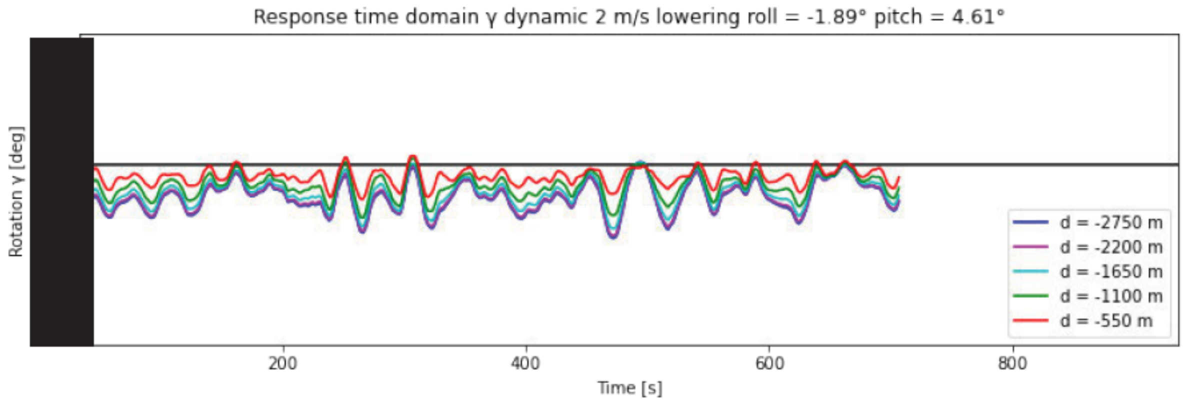

Figure 7.19: Dynamic response at different depths of the system to the yawing moment for lowering at 2 m/s with roll, pitch and current.

7.4. CFD simulation of the experimental test

The experiment shows yaw rotations of -4° to -5° for lowering at 2 and 2.5 m/s, taken from Figure 5.6a. Hoisting shows a similar yaw rotation for 2 m/s and an even smaller rotation for 2.5 m/s. These values match well with the rotations obtained in the CFD analysis in Figure 7.5. The experimental test did not include a current and thus the values in Figure 7.6 cannot be compared. However, the experiment is performed at a lower Reynolds number as Reynolds scaling was not achievable. The experiment at model scale is simulated in OpenFOAM to argue if the experiment is representative for full scale. The verification of the simulation is shown in Appendix J.6, which shows the graphs of the residuals and the Courant number.

[redacted]

Figure 7.21 shows the obtained yawing moment of the CFD simulation at model scale. The first 20 seconds show higher fluctuations. However, the Courant number is above 1 in that region, as shown in Appendix J.6, and can therefore be neglected.

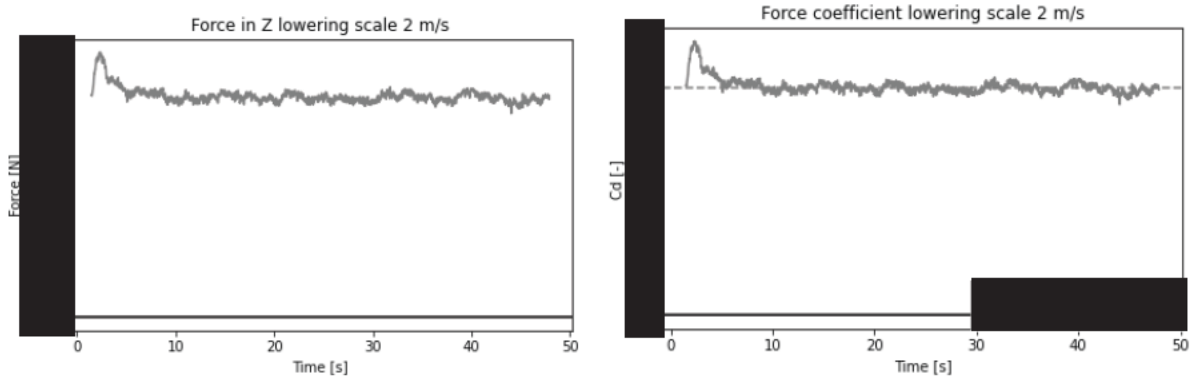

(a) (b)

Figure 7.20: Forces in Z-direction (a) and corresponding force coefficients (b) for lowering at scale at 2 m/s.

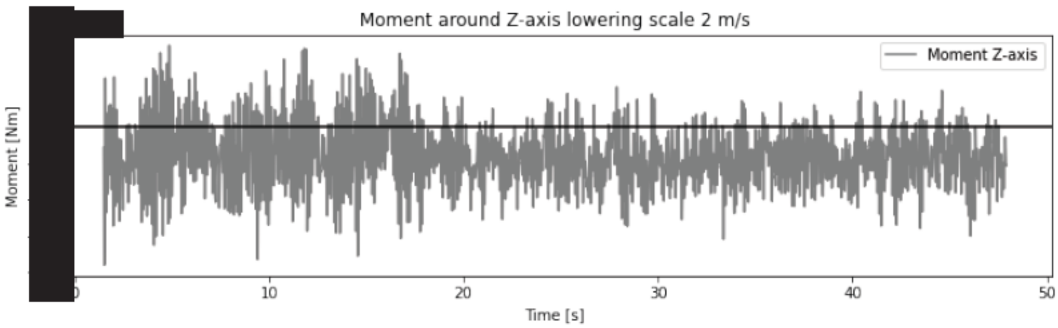

Figure 7.21: Moments around the Z-axis for lowering at scale at 2 m/s.

[redacted]

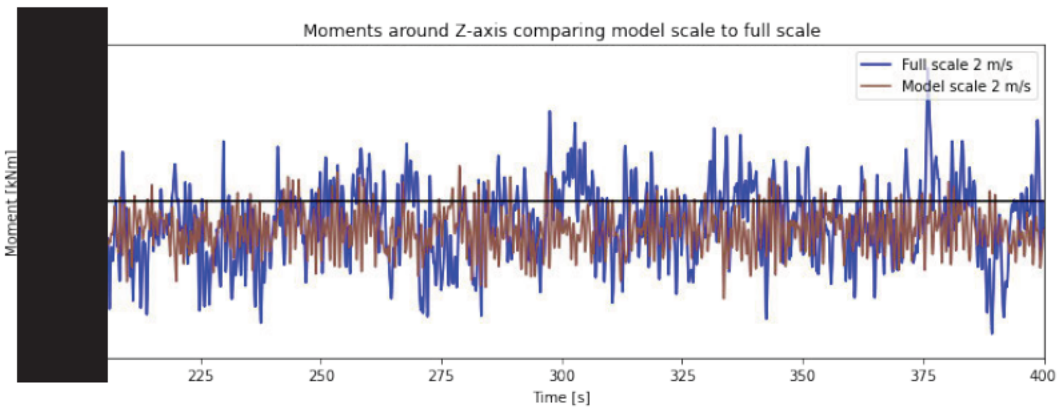

Figure 7.22: Moments around the Z-axis for lowering at scale at 2 m/s converted to full scale values.

Although the experiment is performed at a lower Reynolds number, meaning a larger drag coefficient and smaller fluctuations in the yawing moment, the result of the experimental test is comparable to full scale. As shown in Section 7.3, high frequent fluctuations are damped by the system and therefore the result of the experimental test can be used to obtain the indication of the yawing moment.

The yawing moment is converted into rotations by dividing the moment by the rotational stiffness in the experiments from Figure 5.3b. The results are shown in Figure 7.23, which can be compared to the result of flat with a velocity of 2 m/s in the experimental test in Figure 5.6a. The order of magnitude corresponds well, which validates the experiment.

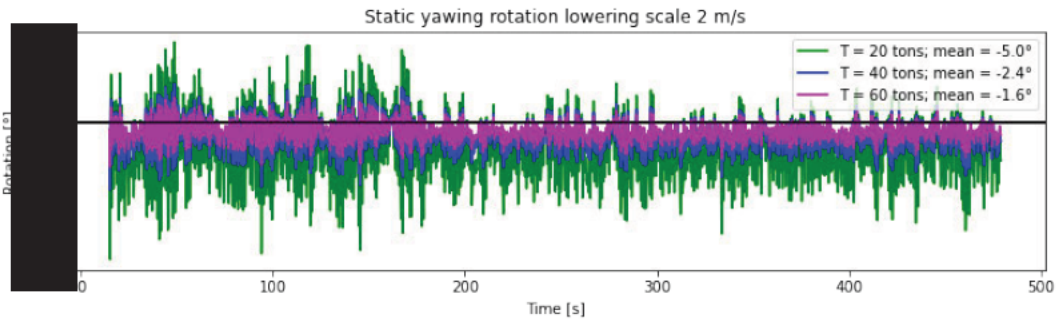

Figure 7.23: Static yaw rotations for lowering at scale at 2 m/s for the three tensions tested in the experimental test.

The experiment tested the system with an initial pitch angle upwards and downwards respectively. Downwards did not result in noticeable differences. However, pitching upwards resulted in a positive rotation during lowering and a larger negative yaw rotation while hoisting, compared to a flat frame. Concluding from both the CFD analysis and the experimental test is that small roll and pitch angles of the system, can result in large differences in yaw rotations.

7.5. Energy consumption

An important parameter in the evaluation of the mechanical lifting system is the energy consumption, which can be calculated for transporting at 2 and 3 m/s. The energy consumption of transporting the nodules by means of hydraulic lifting, is calculated by JM van Wijk (2016) [50]. For a water depth of 5000 m, the average dry solids production for hydraulic lifting is estimated to be 111 kg/s, using an average hydraulic power of 4.9 MW [50]. Per ton of dry nodules, the energy consumption is

$$1000/111 \cdot \frac{1}{3600} \cdot 4.9 = 0.0123 \text{ MWh} = 12.2 \text{ kWh}. \tag{7.5}$$

For the mechanical lifting system in this thesis, the power can be calculated by

$$P = F_L \cdot v, \tag{7.6}$$

with
P as the power [kW],
F_L as the total lifting force, calculated by $F_L = W_{sub} \cdot 9.81 + F_{drag}$ [kN],
v as the transport velocity [m/s].

The lifting force and power are summarised in Table 7.1. The energy consumption per operation can be calculated by

$$E = P \cdot D, \tag{7.7}$$

with
E as the energy consumption [kWh],

D as the duration [h].

The energy consumption per operation and per ton of nodules is summarised in Table 7.1. One cycle includes hoisting, offloading and lowering. [redacted]

	[redacted]	[redacted]
[redacted]	[redacted]	[redacted]
[redacted]	[redacted]	[redacted]
[redacted]	[redacted]	[redacted]
[redacted]	[redacted]	[redacted]

[redacted]

*calculated in the analytical analysis, as no CFD simulation has been performed for hoisting at 3 m/s.

The energy per ton of nodules for the mechanical lifting system while operating at 3 m/s, is only slightly larger compared to operating at 2 m/s. Therefore, it can be concluded that the drag does not take up a large share in the energy consumption of the system and thus operating at 3 m/s is beneficial in terms of energy consumption and production capacity. This is expected, as the gravity of the container filled with nodules is much higher compared to the drag force. In the calculation of the energy consumption for the mechanical lifting system, no losses are taken into account. The calculation on hydraulic lifting by JM van Wijk [50] does take into account the efficiency and performance of the pumps. Therefore the two transport systems cannot directly be compared. However, the energy consumption for mechanical lifting is in the order of magnitude, compared to hydraulic lifting and therefore not a showstopper.

8
Conclusion

This thesis presents a study into the yaw stability of a mechanical lifting concept for the vertical transportation of polymetallic nodules, which is a crucial factor to operate reliably. The uncertainties have to do with rope entanglement, durability and scale-ability: whether or not the needed production capability can be obtained to make the design feasible. The question is answered by presenting a concept, consisting of 2 alternating containers which are being transported vertically by lifting and guidance wires, and analysing its yaw stability. The question to answer in this thesis is: *Can the combined system of the container and the cursor frame, for the vertical transportation of polymetallic nodules by means of mechanical lifting, stably be transported?*

[redacted]

8.1. Analytical analysis

First an analytical analysis is performed to understand the phenomena and estimate the forces and moments acting on the container and cursor frame during lowering and hoisting. The analysis is divided into the restoring moment due to the guidance wires and the yawing moment due to the external forces. Due to the guidance wires, the rotational stiffness in the middle of the water column is [redacted]. The rotational stiffness is smallest in the middle of the water column and this location assessed in further analysis. The lifting wires contribute inconsiderable to the restoring moment and are therefore neglected. Due to the self-weight and drag the container will roll and pitch, especially while lowering as the container is empty, which could induce a yawing moment while the system is being transported. [redacted]

An experimental test and CFD analysis are performed to further analyse the problem. The experimental test includes the dynamics of the system, while the CFD analysis studies the fluid mechanics to take away the uncertainties and unknowns: the drag force, the yawing moment and the fluctuation magnitudes and frequencies.

8.2. Experimental test

The experiment is performed according to Froude scaling with a scaling factor of 100 and simulates the container and cursor frame transporting in the middle of the water column, as this is the location where the rotational stiffness is smallest. Four configurations were tested: A flat and conical top of the container, and an initial pitch angle upwards and downwards. The tests were performed transporting at a converted full scale velocity of 2 and 2.5 m/s.

The experiment shows small yaw rotations, in the order of -4° to -5°, when lowering and hoisting as the concept states. The conical top and an initial pitch upwards result in a positive yaw rotation while lowering. When hoisting no significant difference can be obtained. Between the two velocities no significant difference can be obtained as well. The experiment is validated by an analytical time-integration, that shows that the test tube is long enough to develop yaw rotations. By means of decay tests and an analytical integration in time, an estimation of the damping coefficient is made, which is [redacted] simulation of the system at model scale is done, which shows that the flow field at model scale is similar to the flow field at full scale and thus the obtained yawing moments at model scale are in the order of magnitude as at full scale.

8.3. CFD analysis

In the CFD analysis six simulations are carried out: Lowering at 2 and 3 m/s, lowering with an inclined system, due to self-weight and drag, including current at 2 and 3 m/s, hoisting at 2 m/s and lowering at model scale at 0.2 m/s. The current can be from various directions. However, as the analytical analysis shows that a current from the negative Y-direction results in the largest negative yawing moment and the experiment shows negative rotations, this is chosen to be simulated in the CFD analysis. Hoisting did not include an initial roll and pitch angle, as the container is full while being hoisted and thus the roll and pitch angles are small. The outcomes of the CFD analysis are summarised by the following:

- The static mean yaw rotation, calculated by dividing the yawing moment by the rotational stiffness, for all full scale simulations presented in this research are lower than the stability criterion of 45°: lowering with 2 and 3 m/s, lowering with 2 and 3 m/s with an inclined system including the current, and hoisting with 2 m/s. Lowering with the inclined system and including current at 3 m/s results in the largest static mean yaw rotation, which is -40°. The static maximum yaw rotation of the same simulation is larger than the stability criterion and therefore the safety limit is exceeded.

[redacted]

- The yaw rotation is almost fully caused by the asymmetrical cursor frame.

From the CFD analysis and the experimental test can be concluded that small roll and pitch angles, can result in large differences yawing moments. This is shown by pitching the cursor frame upwards and downwards in the experimental test. Pitching upwards, results in a positive rotation angle, while flat and pitching downwards result in negative yaw rotations. In the CFD analysis, the simulations for 3 m/s substantiate this. The simulation with no roll pitch and current results in a mean yaw rotation of -7°, while in the simulation with a roll angle of -0.57°, a pitch angle of 1.38° and the current, the mean yaw rotation is increased to -29°.

[redacted]

[redacted]

8.4. Dynamic response

The CFD analysis shows fluctuations in the forces and moments acting on the system. The dynamic response of the container and cursor frame to the yawing moment, including momentum, kinetic energy and damping, is calculated for the simulations lowering at 2 m/s for the flat system without current and the inclined system including the current. The high frequent fluctuations (f < 0.075 Hz) are damped by the system and the fluctuations with lower frequencies are not damped and will cause excitation in the system. The dynamic response is calculated at various depths, as the rotational stiffness and natural frequency change over the depth. The largest response occurs in the middle of the water column and the dynamic response is smaller compared to the static response for both simulations. Therefore, at 2 m/s, the container and cursor frame can stably be transported.

8.5. Research question

It can be concluded that mechanical lifting has high potential. The combined system of the container and cursor frame, for the vertical transportation of polymetallic nodules by means of mechanical lifting, can stably be transported at 2 m/s, as the static and dynamic responses are well within the safety limits. Therefore, mechanical lifting shows high potential. The largest response occurs in the middle of the water column, as the rotational stiffness is the smallest at that location. The dynamic response is smaller compared to the static response, as the high frequent fluctuations (f > 0.075 Hz) are damped. Rope entanglement will not occur during normal operation at 2 m/s. However, critical situations due to incidental events can arise, including a winch failure, friction or a sudden high current. This has not been evaluated in this research and therefore stability cannot be guaranteed.

Hoisting at 3 m/s is not investigated and the dynamic response analysis for lowering at 3 m/s is not performed in this thesis. As lowering at 3 m/s with an inclined system and including the current results in a static maximum yaw rotation larger than the safety limit, the stability cannot be guaranteed for operating at 3 m/s.

9

Recommendations

The recommendations for future research are divided into modelling assumptions and continuation concept.

Modelling assumptions

In this thesis assumptions have been made, which should be investigated in further research. This is summarised by the following list:

1. Although the dynamic response is calculated, the evaluation in the CFD analysis in this thesis is static. The container and cursor frame are fixed in position, meaning that the water is flowing instead of the container and cursor moving. The effect of the response of the system on the excitation forces and moments is therefore not included.

[redacted]

3. [redacted]

4. Design optimisation is not included in this thesis, meaning the design of the container to reduce drag and increase the production capacity as much as possible. Expanding to multiple containers per lowering and hoisting operation could be an option. The design of the cursor frame could be optimised as well. In this research, the frame consists of circular pipes with a diameter o[redacted] m. This is a first estimate and should be optimised for its stiffness, strength and drag.

Continuation concept

The following list summarises the recommendations for the further developments of the concept, found by this research.

1. In this thesis, the system is evaluated transporting at 2 and 3 m/s respectively. More research into the dynamic response at 3 m/s is necessary to assess if the system can operate safely at 3 m/s. Statically, at 3 m/s the safety limit can not be guaranteed, as presented in the conclusion, whereas it can when transporting at 2 m/s. It must be further investigated at what velocity between 2 and 3 m/s the limit is reached or how the yaw rotation can be prevented.

2. This thesis focuses on the yawing stability of the container and cursor frame itself. However, the movements of the system result in forces and moments at [redacted]

3. When a full container is hoisted to the vessel, the container cannot be lifted out of the water, as the weight in air is too heavy for the lifting wires. Besides, forces are exerted on the system in the splash zone that are not included in this thesis. The container could be lifted by a separate system attached to the vessel or offloaded underwater, which should be further investigated.

4. Wearing of the ropes due to the transportation is not included in this thesis and should be investigated for continuation of the concept.

5. As mentioned in the conclusion, critical situations due to incidental events can arise, including a winch failure, friction or a sudden high current. This has not been evaluated in this thesis and should be further investigated.

6. Understanding the environmental impact is crucial in order to start deep sea mining. By using mechanical lifting, the environmental impact in the form of the energy consumption and the returning sediment plume could be reduced, compared to for instance hydraulic lifting. Further investigation is necessary to estimate the reduction, including the energy losses in the lifting system.

Bibliography

[1] Thao P. Fabregas Kirsten Hund, Daniele La Porta, Tim Laing, and John Drexhage. Minerals for climate action: The mineral intensity of the clean energy transition. 2020.

[2] DEME. Metal-rich nodules collected from seabed during important technology trial, 2021.

[3] Marta Iglesias-Émbil, Alicia Valero, Abel Ortego, Mar Villacampa, Josep Vilaró, and Gara Villalba. Raw material use in a battery electric car – a thermodynamic rarity assessment. *Resources, Conservation and Recycling*, 158:104820, 2020.

[4] Micheal Lodge. The international seabed authority and deep seabed mining, 2016.

[5] David S. Cronan. Manganese nodules. In J. Kirk Cochran, Henry J. Bokuniewicz, and Patricia L. Yager, editors, *Encyclopedia of Ocean Sciences (Third Edition)*, pages 607–614. Academic Press, Oxford, third edition edition, 2019.

[6] John L. Mero. *The Mineral Resources of the Sea*. Elsevier Publishing Company, 1965.

[7] Stuart G. Kingan. Manganese nodules of the cook islands. 1998.

[8] World Ocean Review. Manganese nodule treasures, 2014.

[9] Boskalis. Boskalis: Company profile, 2022.

[10] Daan Kusters. An analysis of a deep-sea mining nodule mining system: Vertical transportation by means of mechanical lifting. 2020.

[11] GRID-Arendal Micheal Wiedicke-Hombach. Variability in nodule abundance within the clarion-clipperton zone, 2014.

[12] Blue Nodules. Blue nodules summary - deep sea mining. `https://blue-nodules.eu/`, 2020.

[13] Sissel Eriksen Bente Jarandsen. Teknologirapport havbunnsmineraler. 2021.

[14] Peter Davies, Damien Durville, and Thanh Do Vu. The influence of torsion on braided rope performance, modelling and tests. *Applied Ocean Research*, 59:417–423, 2016.

[15] DSM. Technical brochure: Dyneema in marine and industrial applications, 2021.

[16] DSM. Dyneema, the world's strongest fiber, 2013.

[17] Mohammed Mawat. Simulation of cylindrical body structure subjected to flow in different reynolds number regimes. *Muthanna Journal of Engineering and Technology*, 6:45–51, 10 2018.

[18] Jorge Antonio Ricardo Jr and Davi Santos. *Aerodynamic Modeling of Bluff Hulls for Flight Control of Small Multi-Rotor Airships*. PhD thesis, 03 2020.

[19] Yong Bai and Qiang Bai. Chapter 24 - viv and wave fatigue of risers. In Yong Bai and Qiang Bai, editors, *Subsea Pipelines and Risers*, pages 423–436. Elsevier Science Ltd, Oxford, 2005.

[20] Sumer and Fredsoe. Hydrodynamics around cylindrical structures. 1997.

[21] Oriol Colomes. 7.1 introduction to fluid-structure interaction in offshore engineering. *Introduction to Computational Dynamics for Offshore Structures*.

[22] Hanjun Pu et al. Analysis for dynamic characteristics in load-lifting system of the crane. *Procedia Engineering*, 16:586–593, 2011. International Workshop on Automobile, Power and Energy Engineering.

[23] Jovan Vladic, Radomir Đokić, Milan Kljajin, and Mirko Karakašić. Modelling and simulations of elevator dynamic behaviour. *Tehnicki Vjesnik*, 18:423–434, 09 2011.

[24] Keum-Shik Hong and Umer Hameed Shah. Vortex-induced vibrations and control of marine risers: A review. *Ocean Engineering*, 152:300–315, 2018.

[25] A.D. Trim, H. Braaten, H. Lie, and M.A. Tognarelli. Experimental investigation of vortex-induced vibration of long marine risers. *Journal of Fluids and Structures*, 21(3):335–361, 2005. Marine and Aeronautical Fluid-Structure Interactions.

[26] J.R. Morison, J.W. Johnson, and S.A. Schaaf. The Force Exerted by Surface Waves on Piles. *Journal of Petroleum Technology*, 2(05):149–154, 05 1950.

[27] O.M. Faltinsen. *Sea Loads on Ships and Offshore Structures*. 1990.

[28] R. D. Young, J. R. Fowler, E. A. Fisher, and R. R. Luke. Dynamic Analysis as an Aid to the Design of Marine Risers. *Journal of Pressure Vessel Technology*, 100(2):200–205, 05 1978.

[29] Subrata K. Chakrabarti and Ralph E. Frampton. Review of riser analysis techniques. *Applied Ocean Research*, 4(2):73–90, 1982.

[30] J.M. Niedzwecki and P.-Y.F. Liagre. System identification of distributed-parameter marine riser models. *Ocean Engineering*, 30(11):1387–1415, 2003.

[31] S.I. Sagatun, K. Herfjord, and T. Holmas. Dynamic simulation of marine risers moving relative to each other due to vortex and wake effects. *Journal of Fluids and Structures*, 16(3):375–390, 2002.

[32] M.L. Facchinetti, E. de Langre, and F. Biolley. Coupling of structure and wake oscillators in vortex-induced vibrations. *Journal of Fluids and Structures*, 19(2):123–140, 2004.

[33] R. Violette, E. de Langre, and J. Szydlowski. Computation of vortex-induced vibrations of long structures using a wake oscillator model: Comparison with dns and experiments. *Computers Structures*, 85(11):1134–1141, 2007. Fourth MIT Conference on Computational Fluid and Solid Mechanics.

[34] Narakorn Srinil and Hossein Zanganeh. Modelling of coupled cross-flow/in-line vortex-induced vibrations using double duffing and van der pol oscillators. *Ocean Engineering*, 53:83–97, 2012.

[35] T.L. Nguyen, K.D. Do, and J. Pan. Boundary control of two-dimensional marine risers with bending couplings. *Journal of Sound and Vibration*, 332(16):3605–3622, 2013.

[36] Ying-fei et al. Zan. Experimental and numerical investigations on the hydrodynamic characteristics of the planar motion of an open-frame remotely operated vehicle. *Journal of Marine Science and Technology*, 2020.

[37] Li et al. Numerical modelling and experimental testing of the hydrodynamic characteristics for an open-frame remotely operated vehicle. *Journal of Marine Science and Engineering*, 8(9), 2020.

[38] Zhandong Li, Jianguo Tao, Hao Sun, Yang Luo, Liang Ding, and Zongquan Deng. Hydrodynamic calculation and analysis of a complex-shaped underwater robot based on computational fluid dynamics and prototype test. *Advances in Mechanical Engineering*, 9(11):1687814017734500, 2017.

[39] Zhang. Using cfd software to calculate hydrodynamic coefficients. *Journal of Marine Science and Application*, 9(2):149–155, June 2010.

[40] A. van Bergen. A dynamic design and analysis of the flexible hose of the deepsea mining system. 2022.

[41] Oriol Colomes. 6.1 introduction to geometrically nonlinear structures. *Introduction to Computational Dynamics for Offshore Structures*.

[42] Orcina. Orcaflex – world-leading software that goes beyond expectation.

[43] Pepijn de Jong. Lecture slides: Offshore hydromechanics module 1, real flows part 1.

[44] Rui Zhao and Chao Yan. Detailed investigation of detached-eddy simulation for the flow past a circular cylinder at re=3900. *Applied Mechanics and Materials*, 232:471–476, 11 2012.

[45] Philippe Spalart, Sebastien Deck, Michael Shur, Kyle Squires, Michael Strelets, and A. Travin. A new version of detached-eddy simulation, resistant to ambiguous grid densities. *Theoretical and Computational Fluid Dynamics*, 20:181–195, 07 2006.

[46] Sauro Succi. Finite-volumes i: Structured, 2015.

[47] OpenFOAM. Openfoam: User guide v2112: Backward time scheme.

[48] Ideal Simulations. Courant number.

[49] P. Welch. The use of the fast fourier transform for the estimation of power spectra: A method based on time averaging over short, modified periodograms. *Audio Electroacoust*, 15, 1967.

[50] JM van Wijk. Vertical hydraulic transport for deep sea mining: A study into flow assurance. 2016.

[51] Peter Davies, Yvan Reaud, Loic Dussud, and Patrice Woerther. Mechanical behaviour of hmpe and aramid fibre ropes for deep sea handling operations. *Ocean Engineering*, 38(17):2208–2214, 2011.

[52] John Flory, Stephen Banfield, and David Petruska. Defining, measuring, and calculating the properties of fiber rope deepwater mooring lines. 05 2004.

[53] Roland Verreet. The rotation characteristics of steel wire ropes. 2018.

[54] Van Beelen. Van beelen netting ropes twines d12 sk78, 2021.

[55] Eurocable Belgium. Steel wire ropes catalogue, 2021.

[56] EU. E.u. copernicus marine service information: Global ocean ensemble physics reanalysis.

[57] EU. E.u. copernicus marine service information: Global ocean 1/12° physics analysis and forecast updated daily.

[58] Joel T Park and Angelo Olivieri. Ittc recommended procedures: Fresh water and sea water properties. *International Towing Tank Conference*, 2011.

[59] S. F. Hoerner. *Fluid-Dynamic Drag*. 1965.

[60] Det Norske Veritas. Dnvgl-rp-n103: Modelling and analysis of marine operations. 2017.

[61] Jeff Scott. Aerospaceweb: Rocket nose cones and altitude, 2003.

[62] NTNU. Tmr7 experimental methods in marine hydrodynamics: General modelling and scaling laws, 2021.

[63] Frank M. White. *Viscous Fluid FLow*. McGraw-Hill, Inc., 1991.

[64] Eric Loth, John Tyler Daspit, Michael Jeong, Takayuki Nagata, and Taku Nonomura. Supersonic and hypersonic drag coefficients for a sphere. *AIAA Journal*, 59(8):3261–3274, 2021.

C
Site specifications

C.1. Temperature

Figure C.1a shows the monthly mean temperatures over the depth for the time period 01-01-2017 to 01-01-2020. In the middle of the water column the temperature is around 1.6 °C. Figure C.1b shows the mean temperature at the seafloor between 01-01-2020 and 01-01-2022. For the Penrhyn Basin the temperature is around 0.95 °C and for the CCZ the temperature is between 1.1 and 1.2 °C.

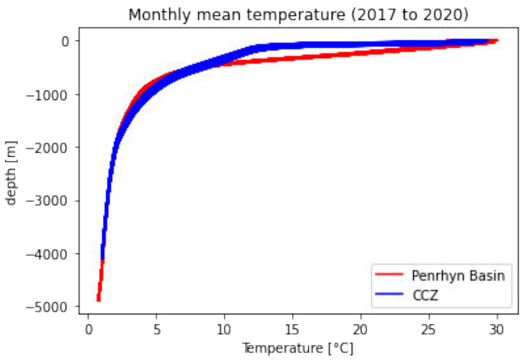

(a)

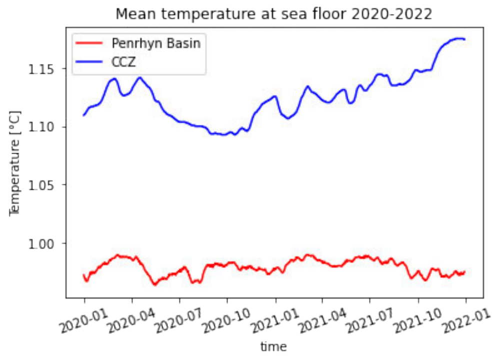

(b)

Figure C.1: Temperature seawater over depth [56] (a) and at the seafloor [57] (b).

C.2. Salinity

The salinity of the two fields are plotted in Figure C.2. In the middle of the water column (at a depth of 2750 m), the salinity for both areas is roughly equal at 34.7 g/kg.

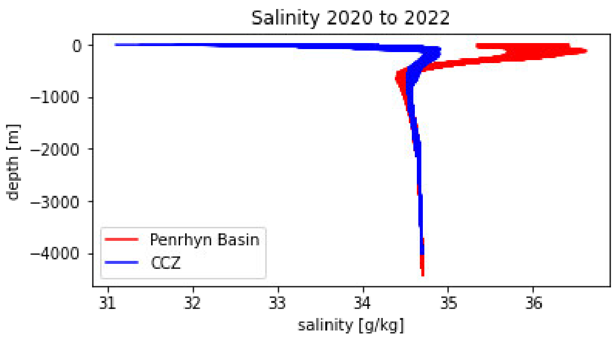

Figure C.2: Salinity over the depth at the CCZ and the Penrhyn Basin [57].

C.3. Density

The density of seawater for a temperature between 0 and 30 °C, is between 1028 and 1021 kg/m^3 as shown in Figure C.3a. Therefore, in this research, the density for the two fields is set to be 1025 kg/m^3.

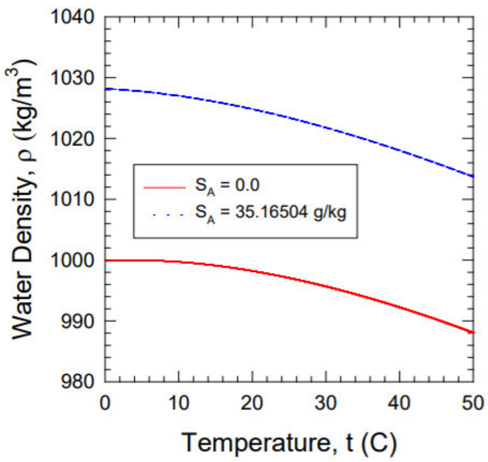

(a)

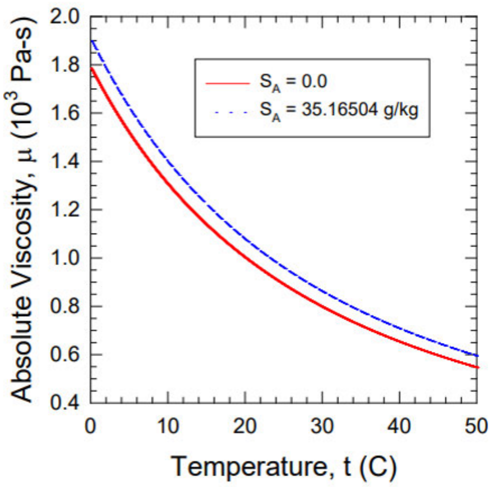

(b)

Figure C.3: Water density (a) and the absolute viscosity (b) dependent on the water temperature [58].

C.4. Kinematic viscosity

The kinematic viscosity is calculated by taking the absolute viscosity divided by the density. The absolute viscosity of a fluid is a value that represents a fluid's resistance to flow freely, caused by shearing stresses. In Figure C.3b the absolute viscosity per temperature is shown for a salinity of 35.2 g/kg. Here it can be seen that the absolute viscosity increases with the temperature decreasing. As the temperature at a depth of 2750 m is 1.6 °C, the viscosity for that temperature is listed in Table C.1.

Table C.1: The absolute and kinematic viscosity at 1.6 °C [58].

Temp (T)	Absolute viscosity μ	Kinematic viscosity $\nu = \frac{\mu}{\rho}$
1.6 °C	$1.81 \cdot 10^{-3}$ Pa·s	$1.76 \cdot 10^{-6}$ m^2/s

The salinity at the nodule fields is estimated to be 34.7 g/kg, as shown in the section above, which is a 0.5 g/kg difference. The assumed higher salinity, gives a higher density and thus a slightly lower estimated kinematic viscosity.

C.5. Current

Figure C.4 and C.6 show the maximum and mean current velocities and Figure C.5 and C.7 show the current direction of the two fields. The current for a depth between -1000 m to the seafloor is considered constant in this thesis at 0.1 m/s. The current is increasing to 0.2 m/s from -1000 m to -200 m, and to 0.6 m/s at sea level. The current direction varies not only in time, but also over the depth. Therefore all directions should be considered.

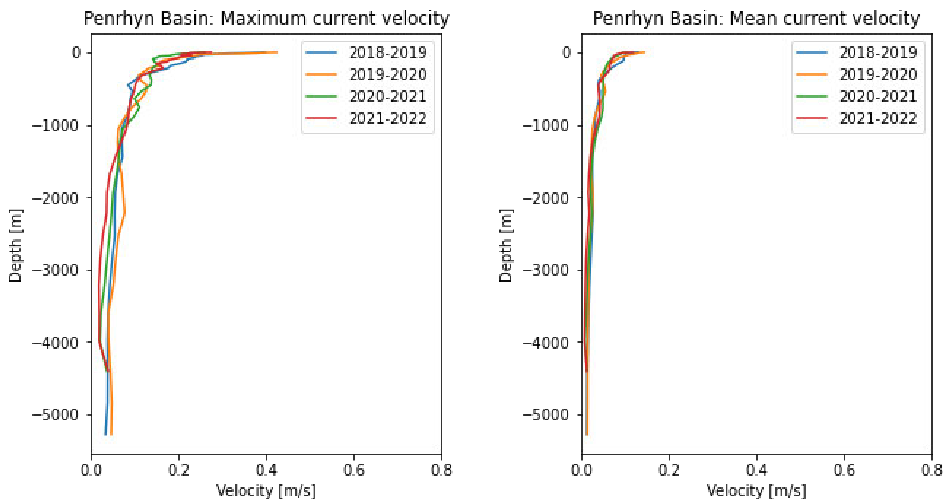

Figure C.4: Maximum and mean current velocity at the Penrhyn Basin [56, 57].

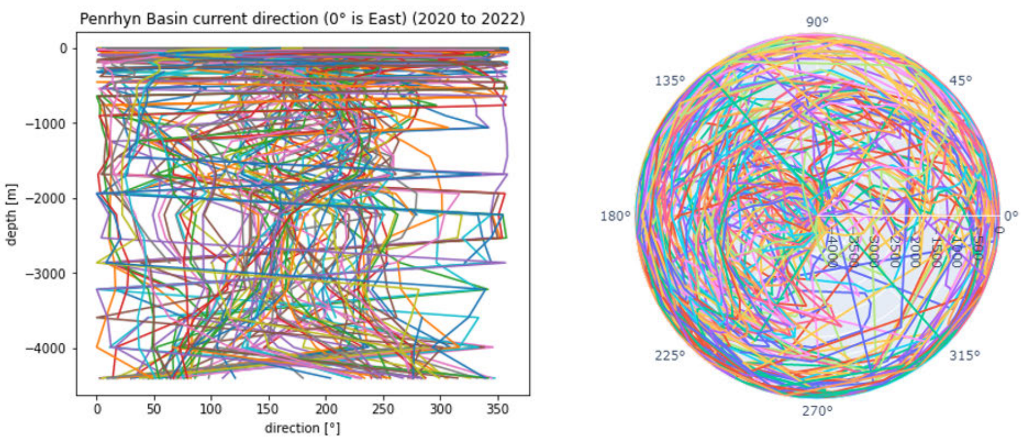

Figure C.5: Current direction at the Penrhyn Basin [56, 57].

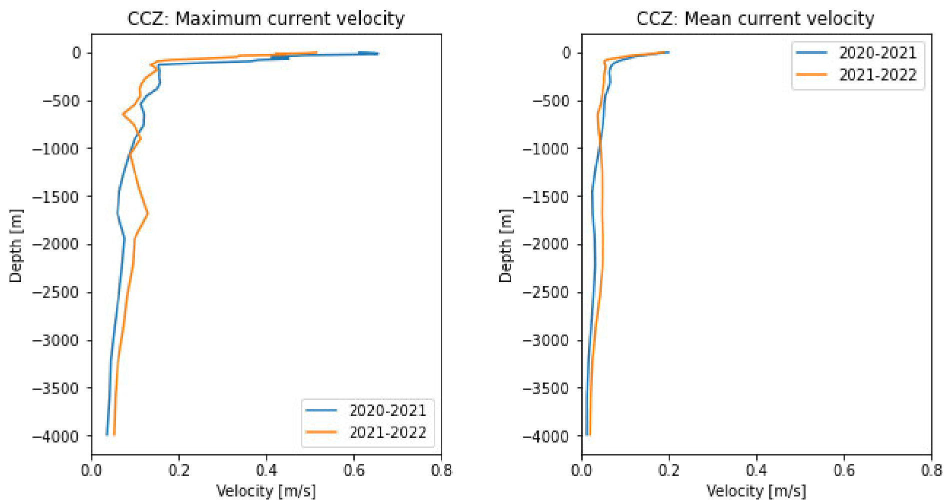

Figure C.6: Maximum and mean current velocity at the CCZ [57].

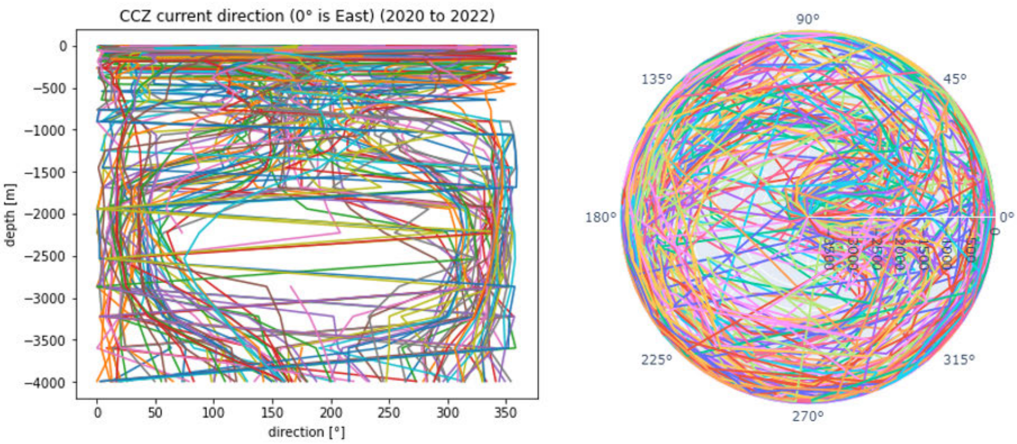

Figure C.7: Current direction at the CCZ [57].

F

Coefficients

F.1. Drag coefficients

F.1.1. Cylinder

Figure F.1: Drag coefficient curve for a cylinder in a flow normal to the axis [59].

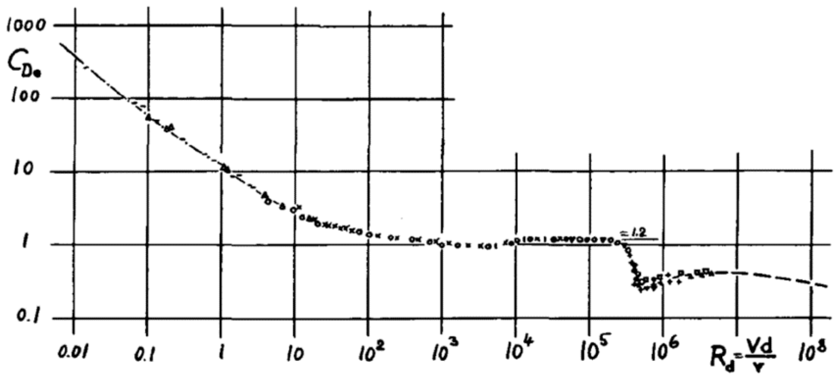

Figure F.2: Drag coefficient curve for a cylinder in axial flow [59].

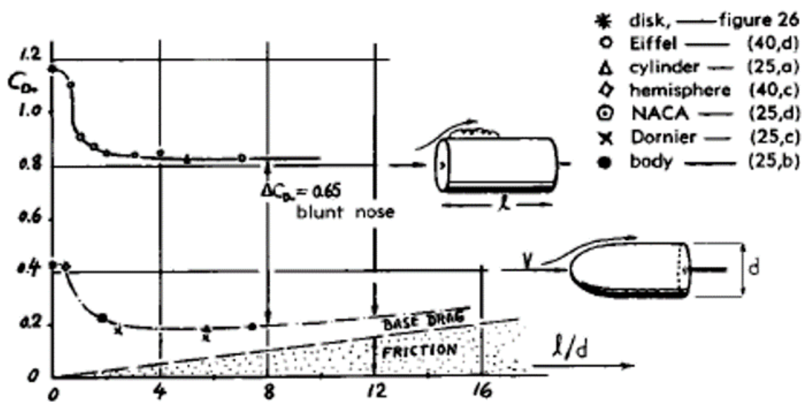

F.1.2. Cone

Figure F.3: Drag coefficient curve for a cone in axial flow [59].

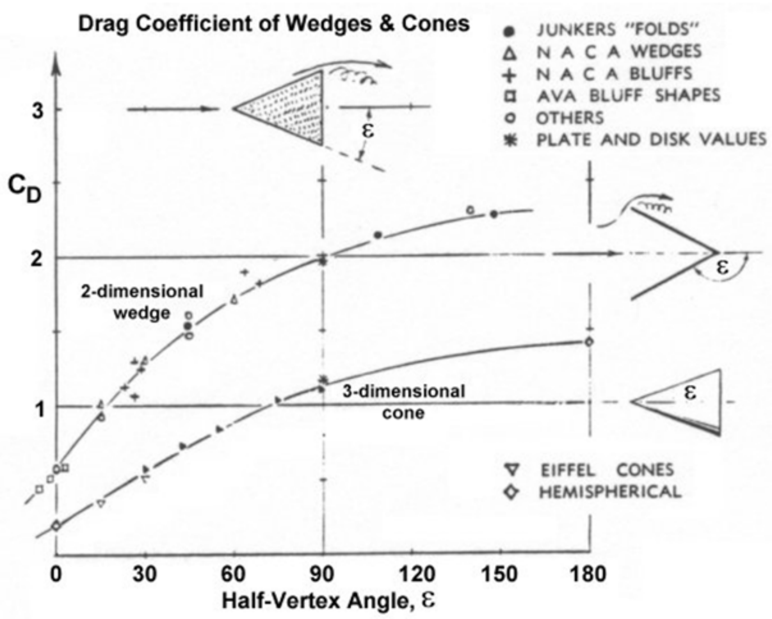

F.1.3. Blunt Cone

Figure F.4: Drag coefficient various nose shapes [59].

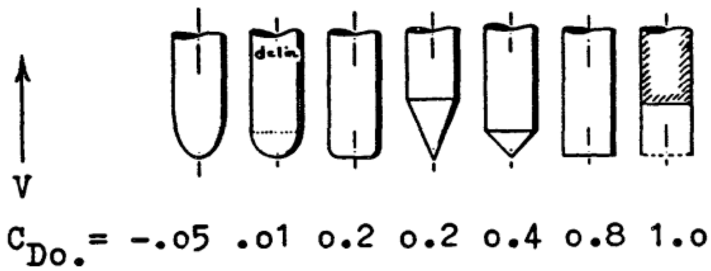

Figure F.5: Drag coefficient reduction for various nose shapes [61].

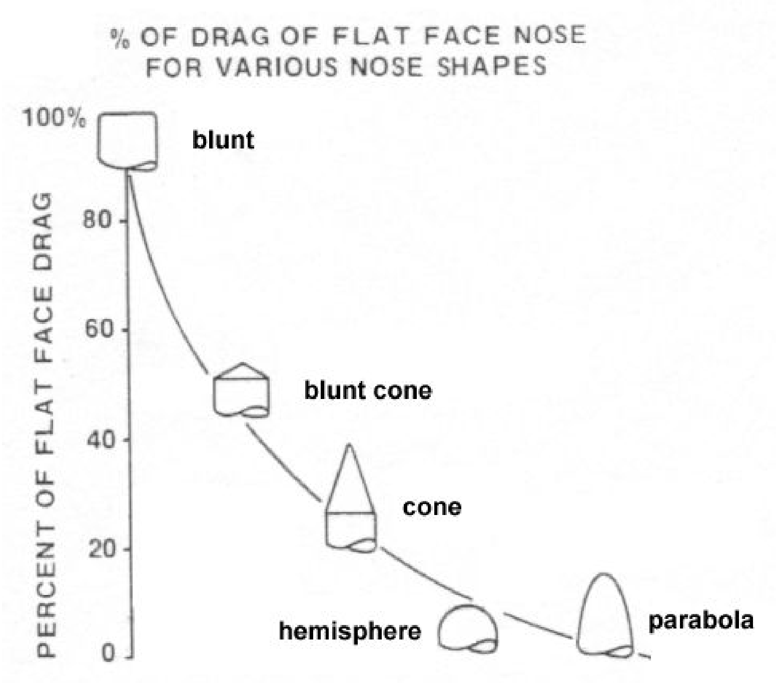

F.2. Added mass coefficients

F.2.1. Circular Disc

Figure F.6: Added mass coefficients for a circular plate [60].

Body shape	*Direction of motion*	C_A	V_R
Circular disc 	Vertical	$2/\pi$	$\frac{4}{3}\pi a^3$

F.2.2. Circular Cylinder

Figure F.7: Added mass coefficients for a cylinder [60].

Right circular cylinder	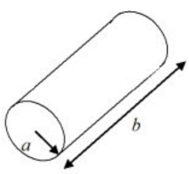	Vertical	$b/2a$	C_A	$\pi a^2 b$
			1.2	0.62	
			2.5	0.78	
			5.0	0.90	
			9.0	0.96	
			∞	1.00	

The flow around the 2D container is visualised in Figure H.18 at t = 30, 50, 100 and 180 s. The colour map indicates the magnitude of the flow velocity and is equal for all images. In the first image the flow is starting to form around the cylinder, and later eddies are generated behind the cylinder.

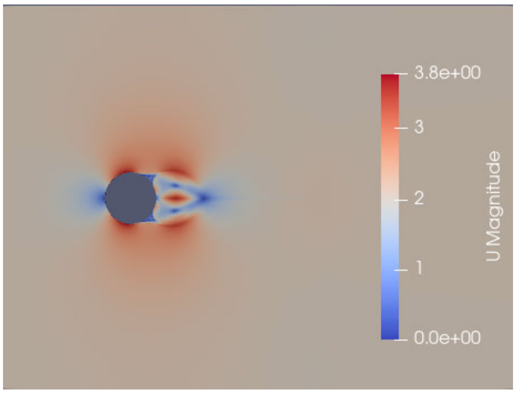

(a) t = 30 s

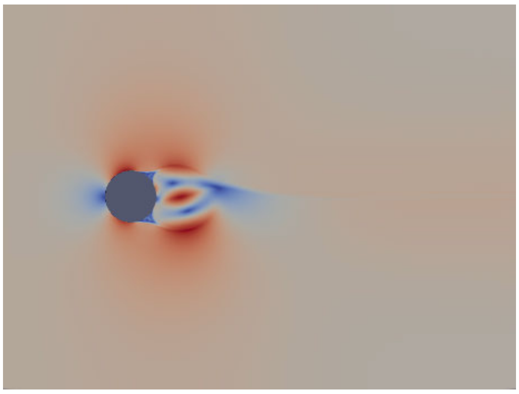

(b) t = 50 s

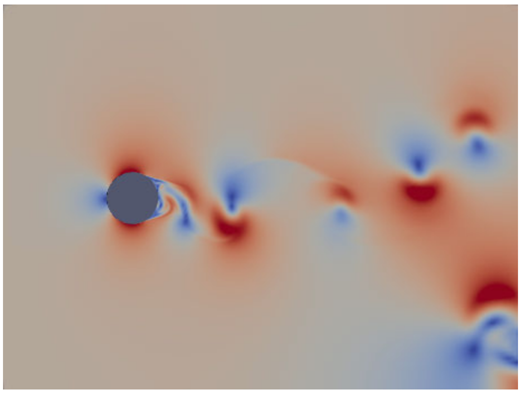

(c) t = 100 s

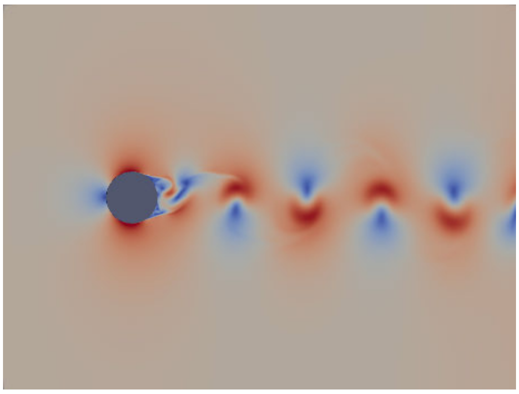

(d) t = 180 s

Figure H.2: Representation of the flow of 2 m/s around the cylinder in 2D at different times.

The forces on the cylinder are plotted in Figure H.3a, from 50 to 200 s. The left image shows the forces in the x-direction, which is the flow direction. At the start, the force oscillates randomly and after t = 120 s a more harmonic oscillation is obtained. This implies that the flow reaches steady state. The force is dominated by the pressure force, compared to the viscous force. In Figure H.3b the corresponding force coefficients are shown. These are calculated by

$$C_d = \frac{F_x}{(\frac{1}{2} \cdot A \cdot \rho \cdot U^2)}. \tag{H.2}$$

Figure H.4a shows the forces in y-direction, which is perpendicular to the flow direction. The force oscillates around zero, which corresponds to the eddies visible in Figure H.2. The flow is alternating the two sides of the cylinder, which induces a force. The oscillating force in y-direction induces a moment on the cylinder in z-direction, which is visible in Figure H.4b. Again, after t = 120 s the flow reaches steady state. The period of the oscillating force after t = 120 s is 14.5 s, which is a frequency of 0.069 Hz. The Strouhal number is

$$St = \frac{f \cdot D}{U} = \frac{0.069 \cdot 10}{2} = 0.34. \tag{H.3}$$

The relation between the Strouhal number and Reynolds number in Figure 3.14, matches well with the calculated Strouhal number for this simulation.

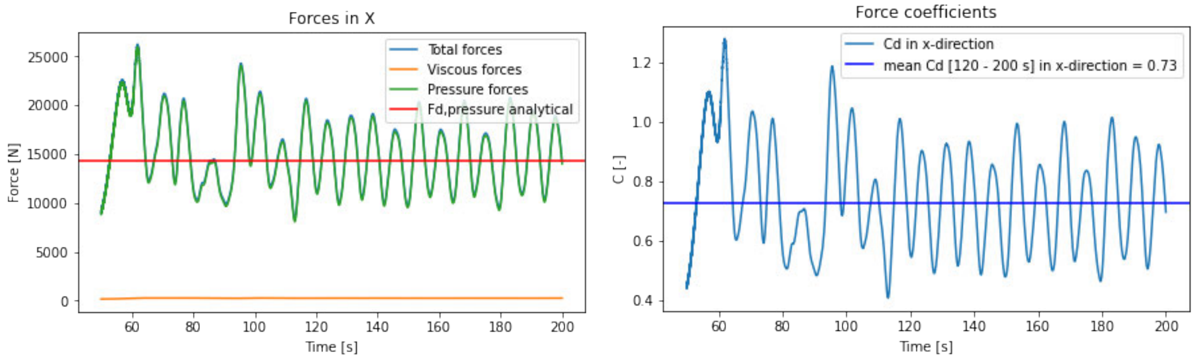

(a) (b)

Figure H.3: Force in X-direction (a) and the corresponding force coefficients (b) for the cylinder in 2D at 2 m/s.

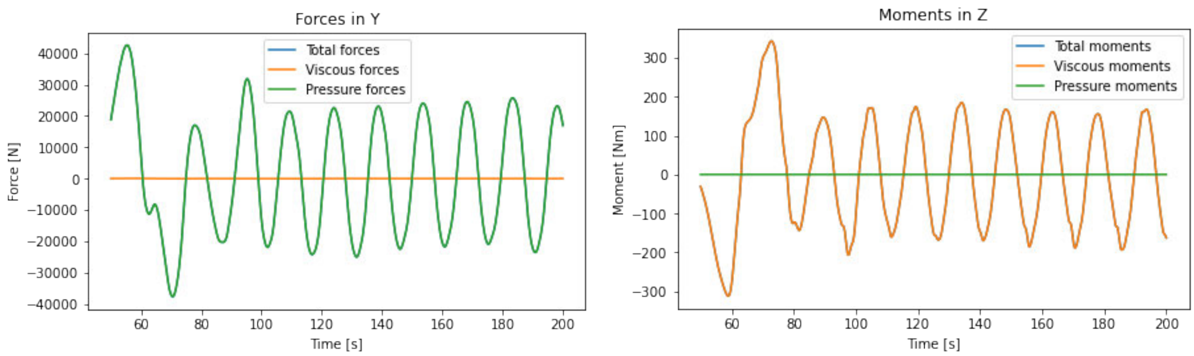

(a) (b)

Figure H.4: Force in Y-direction (a) and the moment around the Z-axis (b) for the cylinder in 2D at 2 m/s.

H.1.1. Verification

The mean and maximum Courant number (CFL) for each time step is shown in Figure H.5. The CFL is below 1 and therefore the criterion is satisfied.

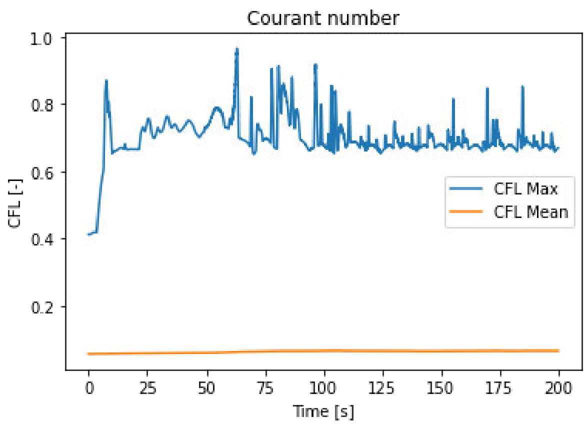

Figure H.5: Courant number for the cylinder in 2D at 2 m/s.

The residuals for the velocities in X- and Y-direction are shown in Figure H.6. The residuals for the pressure and nuTilda are shown in Figure H.7.

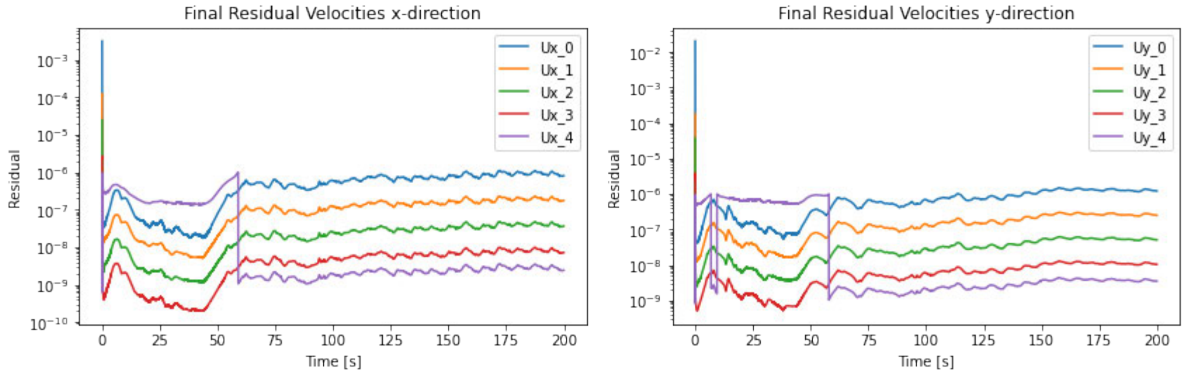

Figure H.6: Residuals velocities for the cylinder in 2D at 2 m/s.

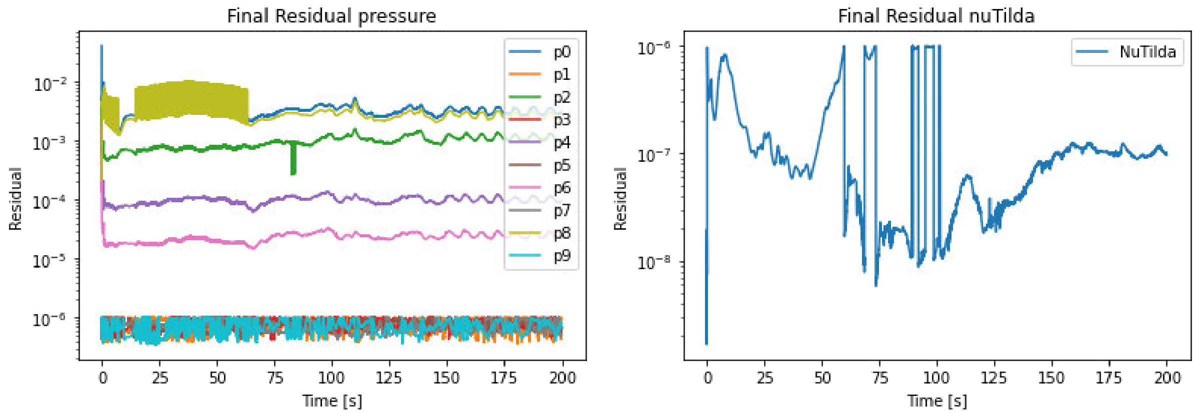

(a) (b)

Figure H.7: Residuals pressure (a) and nuTilda (a) for the cylinder in 2D at 2 m/s.

H.1.2. Validation

To validate the results an analytical estimate to the case is calculated. The Reynolds number for this case is

$$Re = \frac{U \cdot D}{\nu} = \frac{2 \cdot 10}{1.76E - 06} = 1.14E + 07. \tag{H.4}$$

For a cylinder with the a Reynolds number in the order of 10E+07, the drag coefficient for the pressure drag force can be estimated to be 0.7 [59]. The pressure drag force in x-direction is

$$F_{d,pressure,x} = \frac{1}{2} \cdot C_d \cdot A \cdot \rho \cdot U^2 = \frac{1}{2} \cdot 0.7 \cdot (10 \cdot 1) \cdot 1025 \cdot 2^2 = 14350\,\mathrm{N}. \tag{H.5}$$

The result is shown in Figure H.3a, which corresponds well with the CFD results.

H.2. Case 2: Uniform flow 2 m/s sphere 3D

The second case to verify the physics behind the numerical model, is a uniform flow of 2 m/s around a sphere with a diameter of 6 m. Three mesh sizes are presented, M, L and XL, with their specifics in Table H.1.

Table H.1: Mesh sizes for the sphere in 3D at 2 m/s.

	Domain (X Y Z)	Cells	Faces sphere
M	(36 36 45)	1439104	6168
L	(36 36 38)	1738264	24376
XL	(40 40 40)	2890936	24376

Figure H.8 shows the force in Z-direction and the corresponding force coefficients for mesh size XL. The force for the mesh sizes L and XL match well. However, mesh size M shows a higher force.

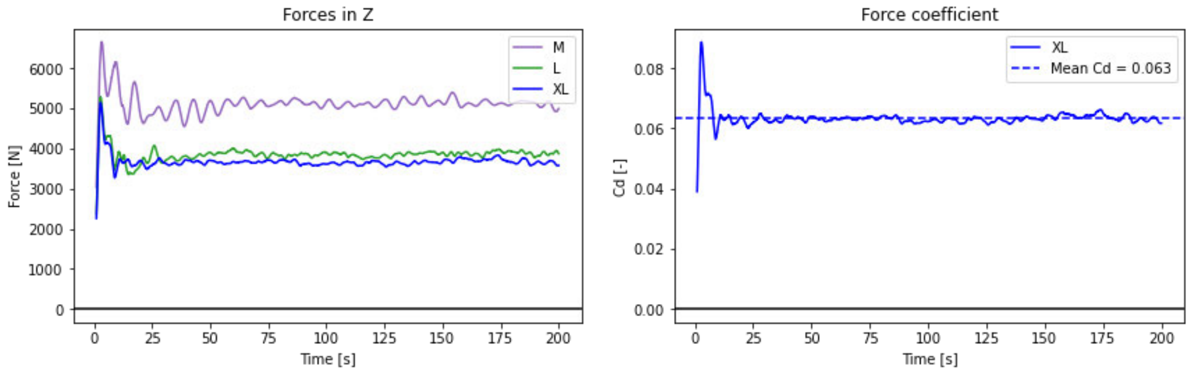

(a) (b)

Figure H.8: Force in Z-direction (a) and the corresponding force coefficients (b) for the sphere in 3D at 2 m/s.

To understand the change in the force in Z-direction between mesh size M and XL, a representation of the flow at t = 120 s for the mesh sizes M and XL are shown in Figure H.9. Here we see that the wake in mesh size XL is more narrow compared to mesh size M, causing the decrease in force in Z-direction. As the mesh size in XL is finer, the flow is better represented.

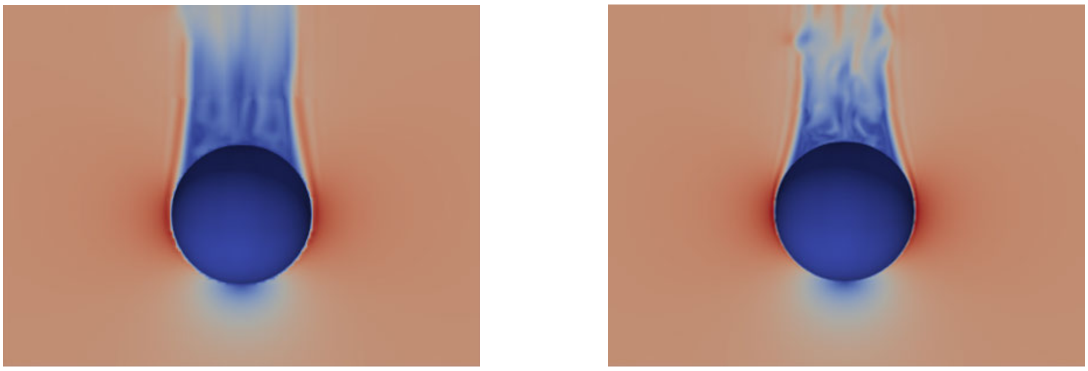

(a) (b)

Figure H.9: Representation of the flow at t = 120 s for mesh size M (a) and XL (b) for the sphere in 3D at 2 m/s.

Figure H.10 shows the forces in X- and Y-direction. The forces oscillate around zero, which is expected as the sphere is symmetrical. The three mesh sizes M, L and XL match well. Figure H.11 shows the moments around the X- and Y-axis and Figure I.4 shows the moment around the Z-axis. The moments are small and oscillate around zero. Again all mesh sizes match well.

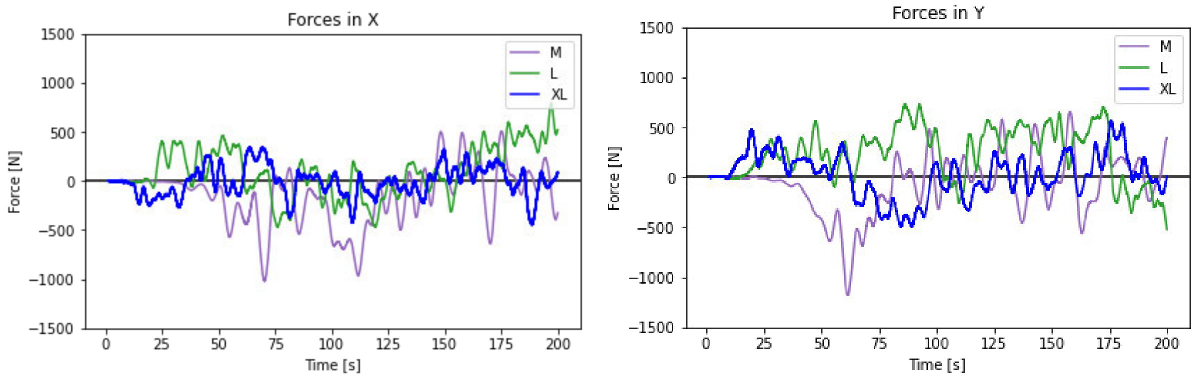

(a) (b)

Figure H.10: Force in X-direction (a) and Y-direction (b) for the sphere in 3D at 2 m/s.

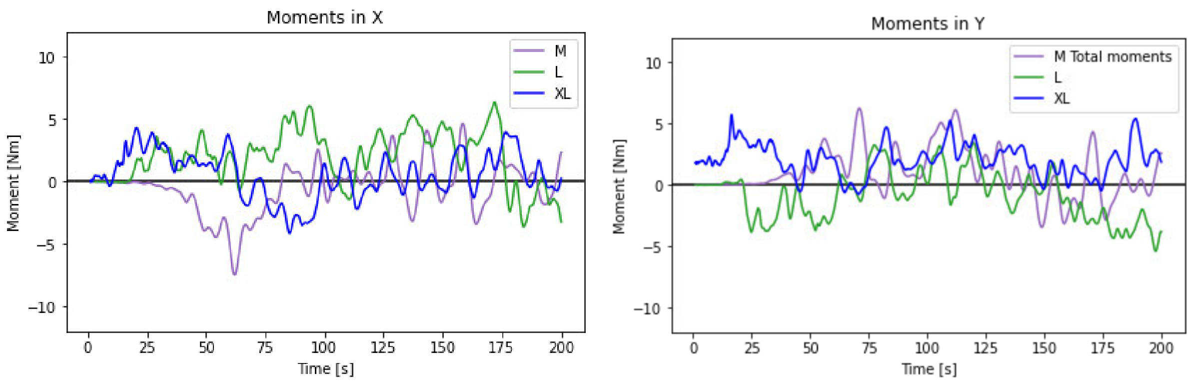

(a) (b)

Figure H.11: Moments around the X-axis (a) and Y-axis (b) for the sphere in 3D at 2 m/s.

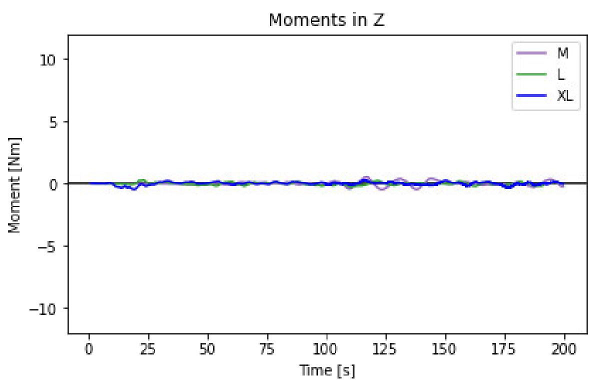

Figure H.12: Moments around the Z-axis for the sphere in 3D at 2 m/s.

H.2.1. Verification

Figure H.13a shows the mean and maximum Courant number for the simulation with mesh size XL. The maxmimum Courant number is below 1, which suffices the criterion. Figure H.13b to H.15b shows the residuals for the velocities, pressure and nuTilda. After t = 50 s all residuals have converged.

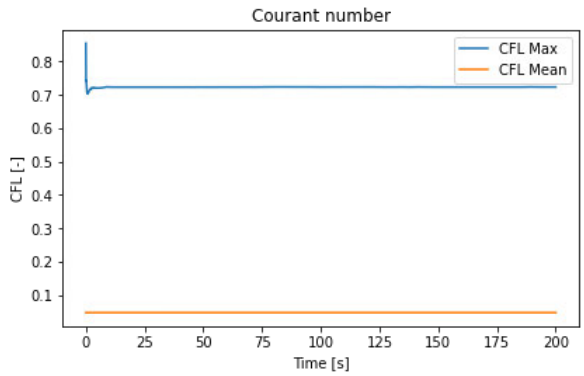

(a)

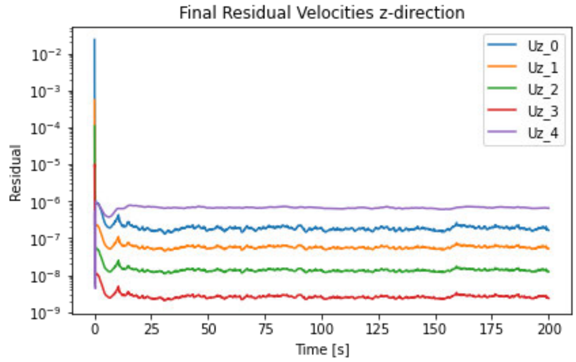

(b)

Figure H.13: Courant number (a) and residuals of the velocity in Z-direction (b) for the sphere at 2 m/s.

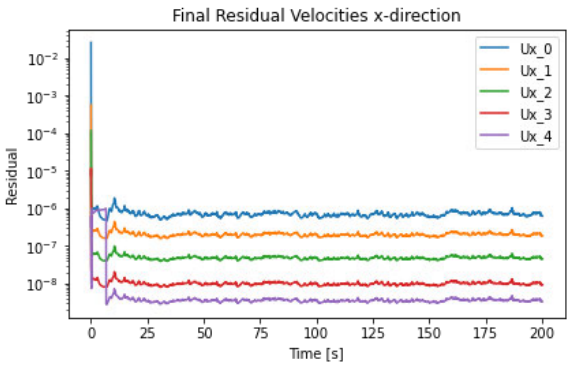

(a)

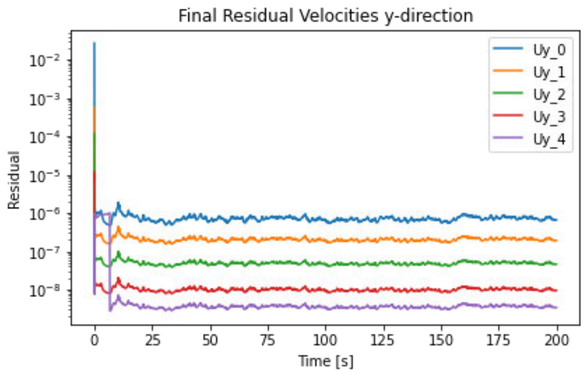

(b)

Figure H.14: Final residuals of the velocity in X-direction (a) and Y-direction (b) for the sphere at 2 m/s.

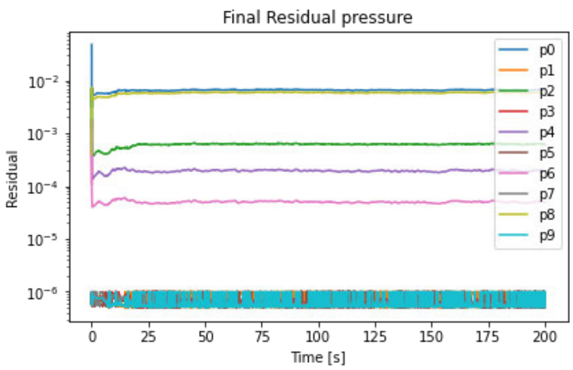

(a) Residual velocities pressure

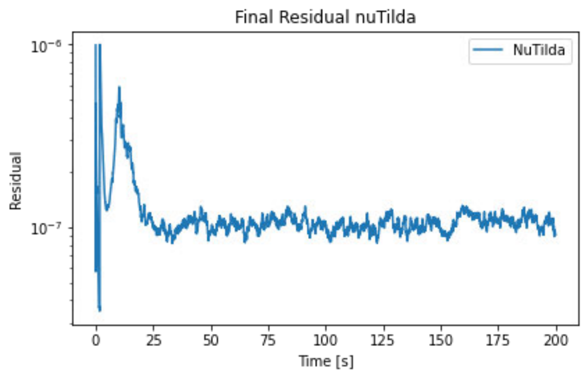

(b) Residual velocities nuTilda

Figure H.15: Final residuals of the pressures (a) and nuTilda (b) for the sphere in 3D at 2 m/s.

H.2.2. Validation

The Reynolds number for the sphere is calculated by

$$Re = \frac{U \cdot D}{\nu} = \frac{2 \cdot 6}{1.76\text{E-06}} = 6.82\text{E+06}. \tag{H.6}$$

The results are compared to literature by White [63] and Hoerner [59] in Figure H.16. The purple cross is the result of the CFD simulation. The drag coefficient from the CFD analysis is in the expected region in the graph, although it is slightly lower than expected. However, little literature is available about a sphere with a Reynolds number higher than 1E6 and therefore no thorough comparison can be made.

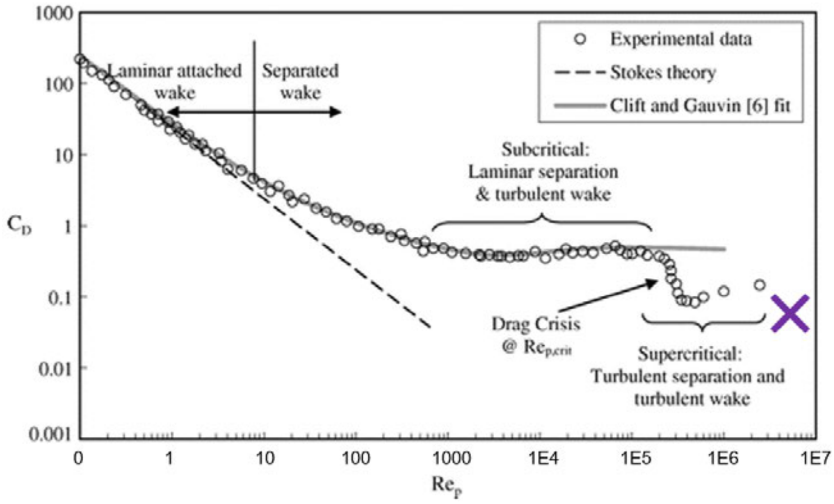

Figure H.16: Drag coefficient for a sphere [64] with experimental data by White [63] and Hoerner [59].

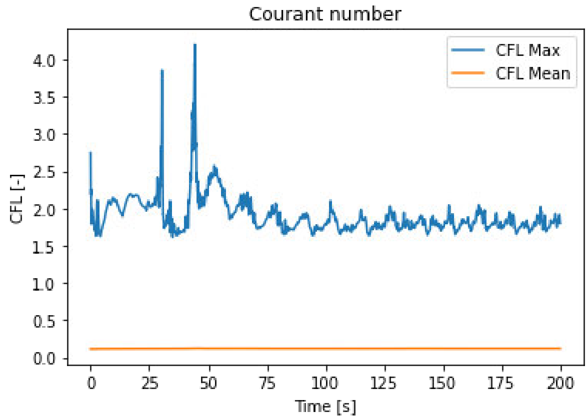

Figure H.21: Courant number for the container in 2D at 2 m/s.

The residuals for the velocities in X- and Z-direction are shown in Figure H.22. The residuals for the pressure and nuTilda are shown in Figure H.23.

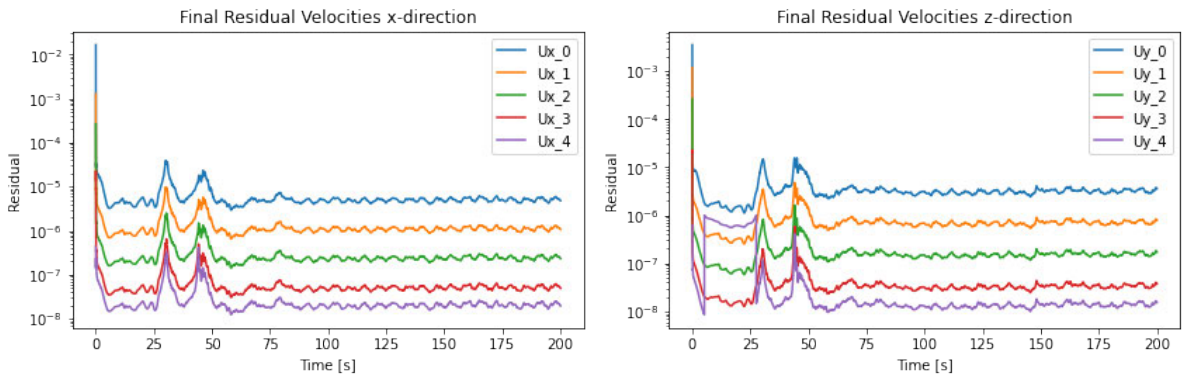

Figure H.22: Residuals velocities for the container in 2D at 2 m/s.

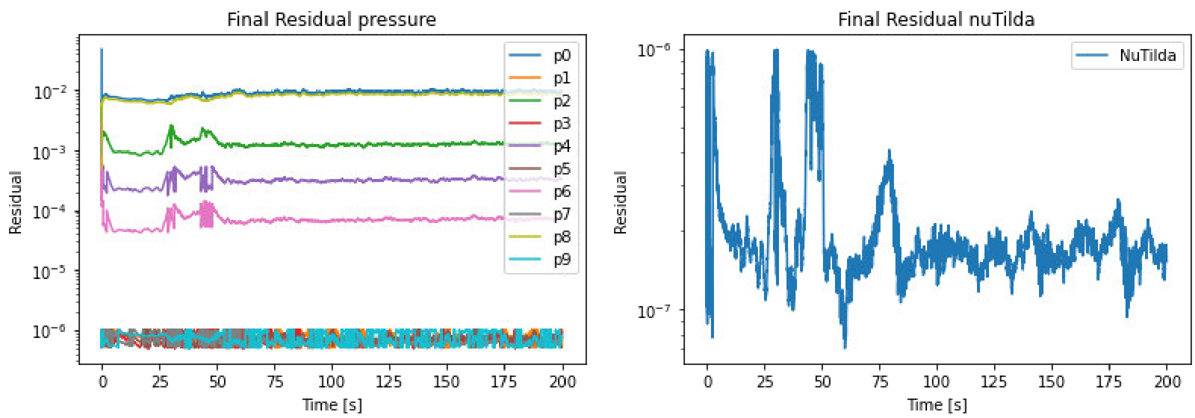

(a) (b)

Figure H.23: Residuals pressure (a) and nuTilda (b) for the container in 2D at 2 m/s.

J

Verification CFD simulations

J.1. DSM 2 m/s lowering

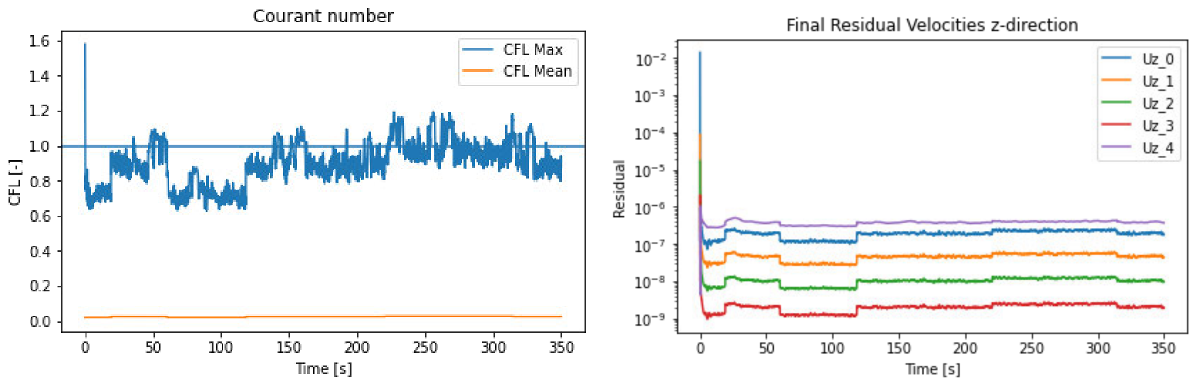

(a) (b)

Figure J.1: Courant number (a) and final residuals velocities in Z-direction (b) for lowering the DSM system at 2 m/s.

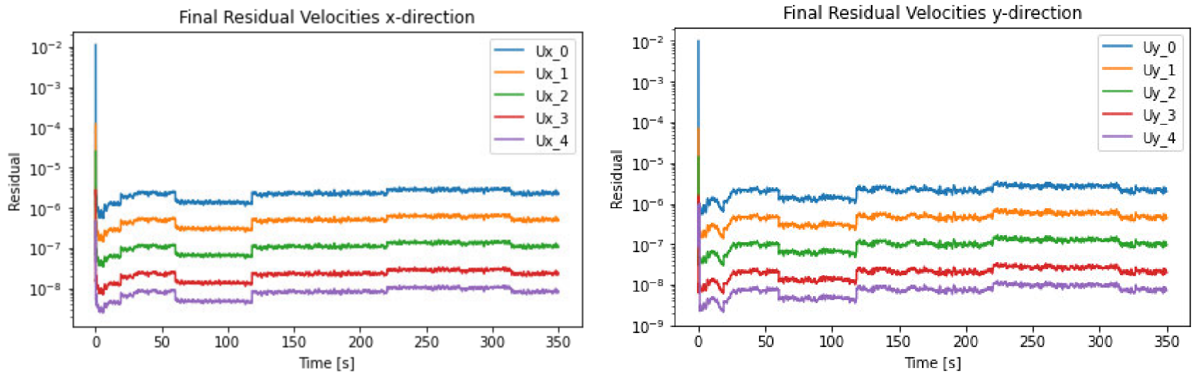

(a) (b)

Figure J.2: Final residuals velocities in X-direction (a) and Y-direction (b) for lowering the DSM system at 2 m/s.

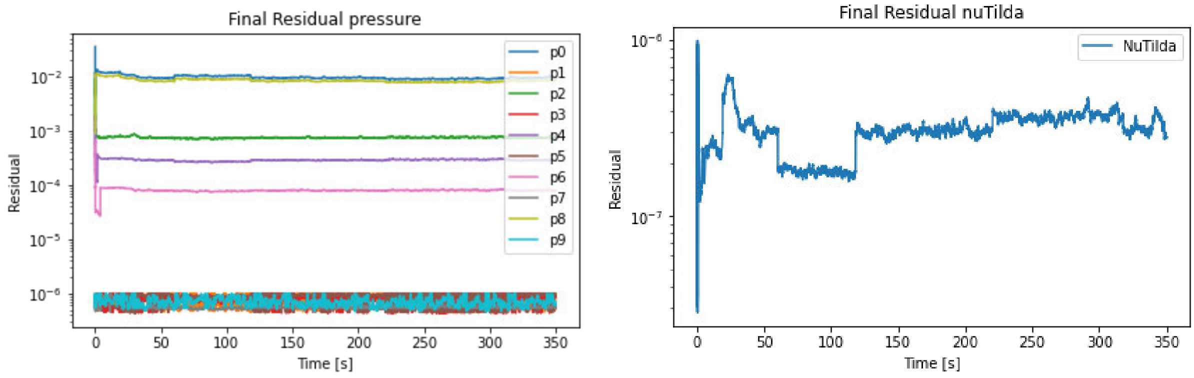

(a) (b)

Figure J.3: Final residuals pressure (a) and nuTilda (b) for lowering the DSM system at 2 m/s.

J.2. DSM 3 m/s lowering

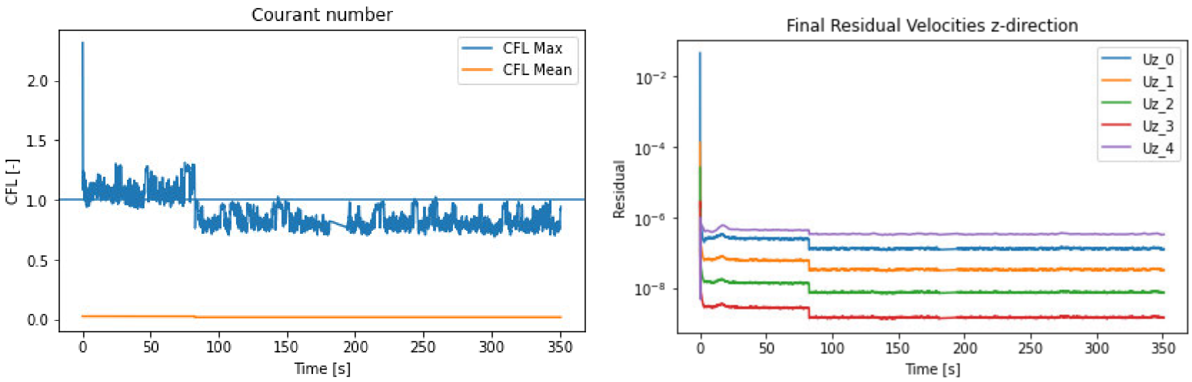

(a) (b)

Figure J.4: Courant number (a) and final residuals velocities in Z-direction (b) for lowering the DSM system at 3 m/s.

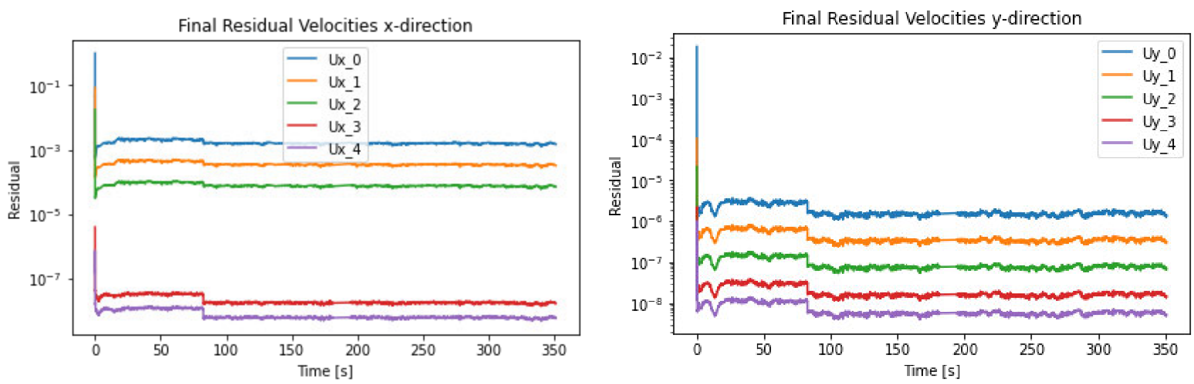

(a) (b)

Figure J.5: Final residuals velocities in X-direction (a) and Y-direction (b) for lowering the DSM system at 3 m/s.

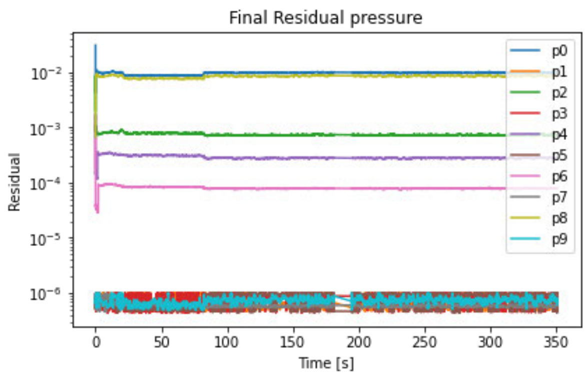

(a)

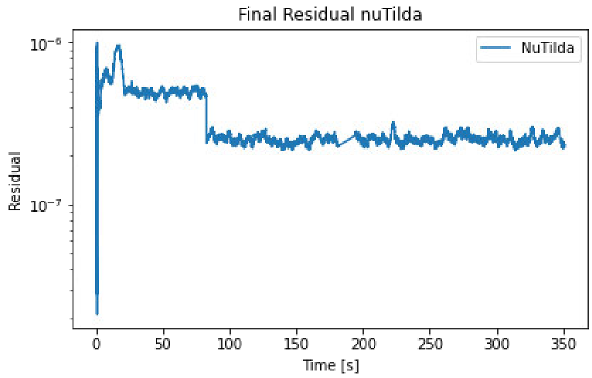

(b)

Figure J.6: Final residuals pressure (a) and nuTilda (b) for lowering the DSM system at 3 m/s.

J.3. DSM 2 m/s lowering inclined including current

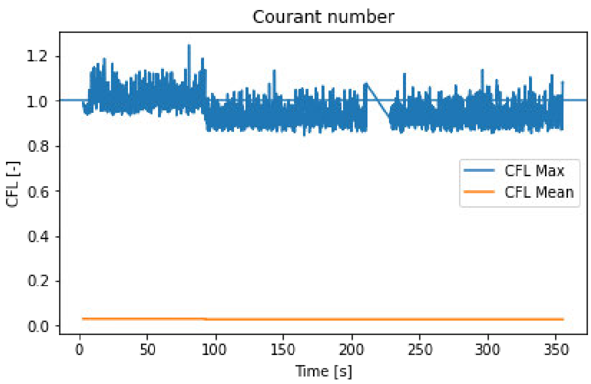

(a)

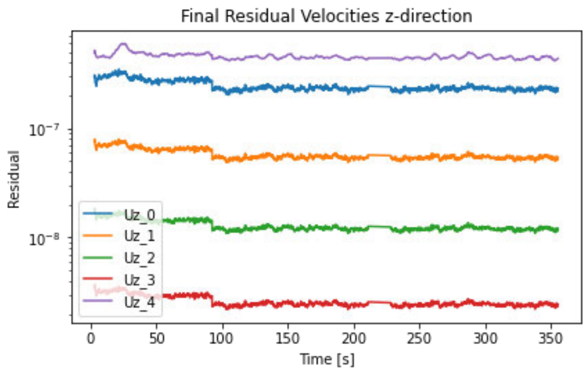

(b)

Figure J.7: Courant number (a) and final residuals velocities in Z-direction (b) for lowering the inclined system including current at 2 m/s.

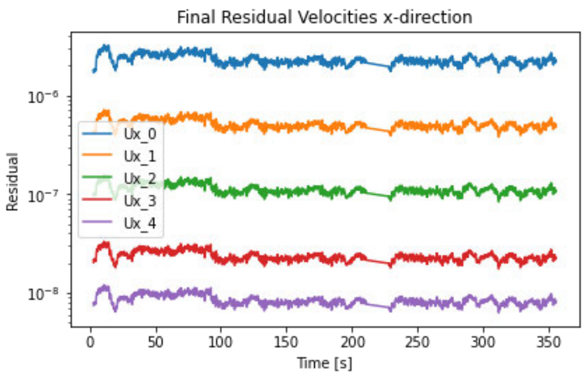

(a)

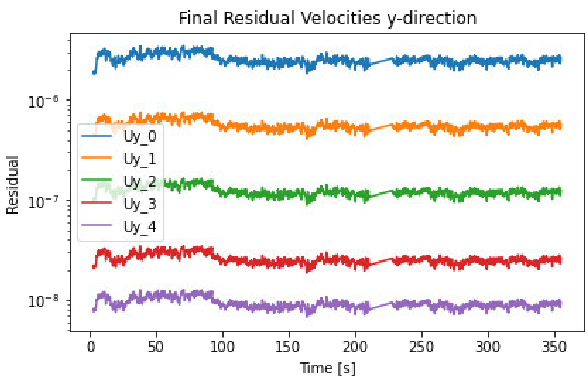

(b)

Figure J.8: Final residuals velocities in X-direction (a) and Y-direction (b) for lowering the inclined system including current at 2 m/s.

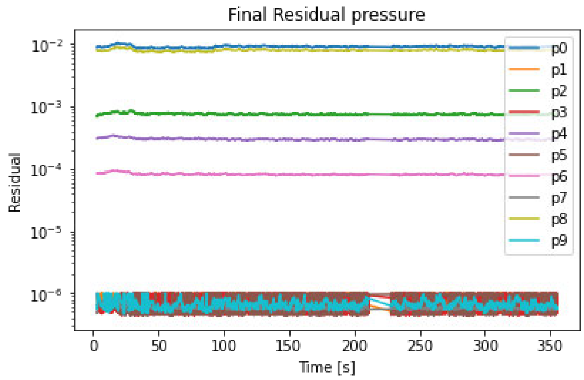

(a)

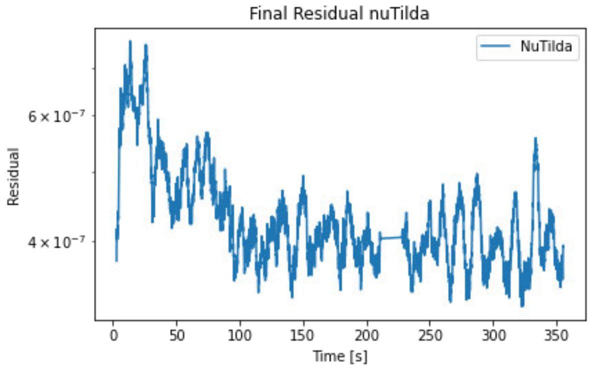

(b)

Figure J.9: Final residuals pressure (a) and nuTilda (b) for lowering inclined including current at 2 m/s.

J.4. DSM 3 m/s lowering inclined including current

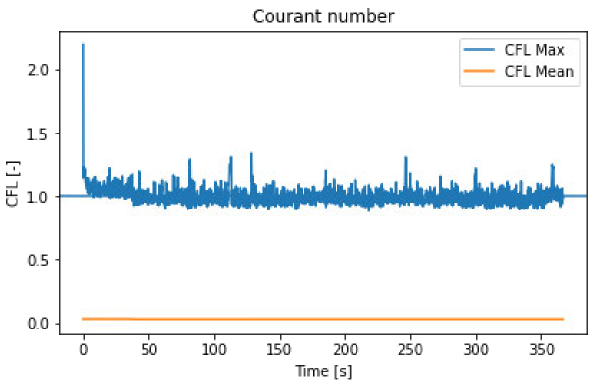

(a)

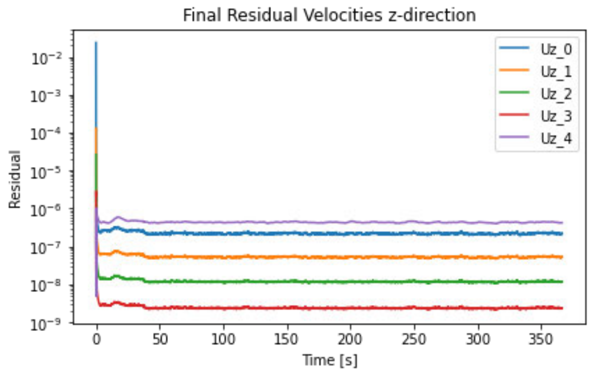

(b)

Figure J.10: Courant number (a) and final residuals velocities in Z-direction (b) for lowering the inclined system including current at 3 m/s.

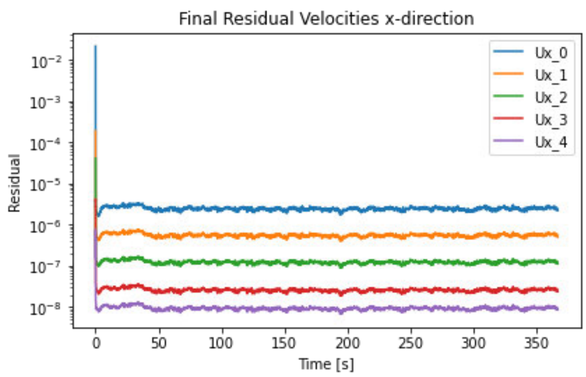

(a)

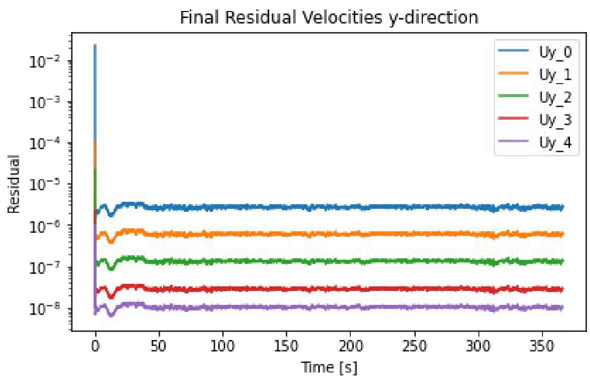

(b)

Figure J.11: Final residuals velocities in X-direction (a) and Y-direction (b) for lowering the inclined system including current at 3 m/s.

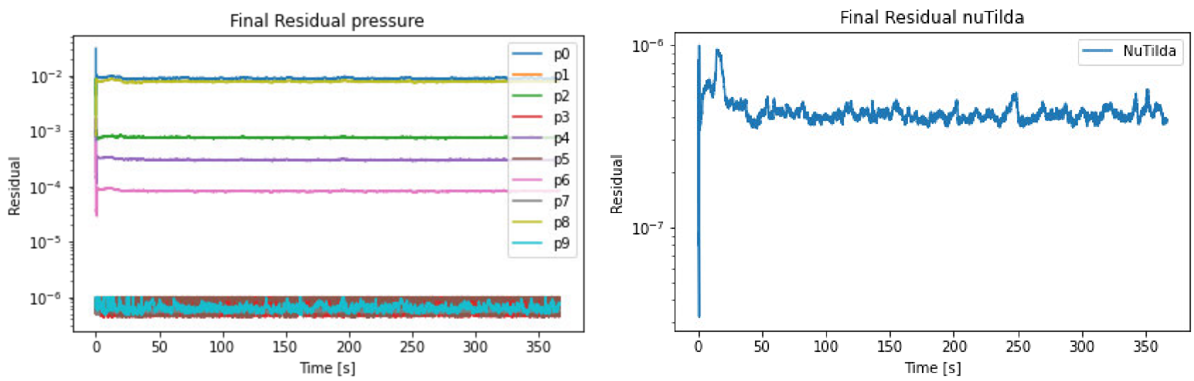

(a) (b)

Figure J.12: Final residuals pressure (a) and nuTilda (b) for lowering the inclined system including current at 3 m/s.

J.5. DSM 2 m/s hoisting

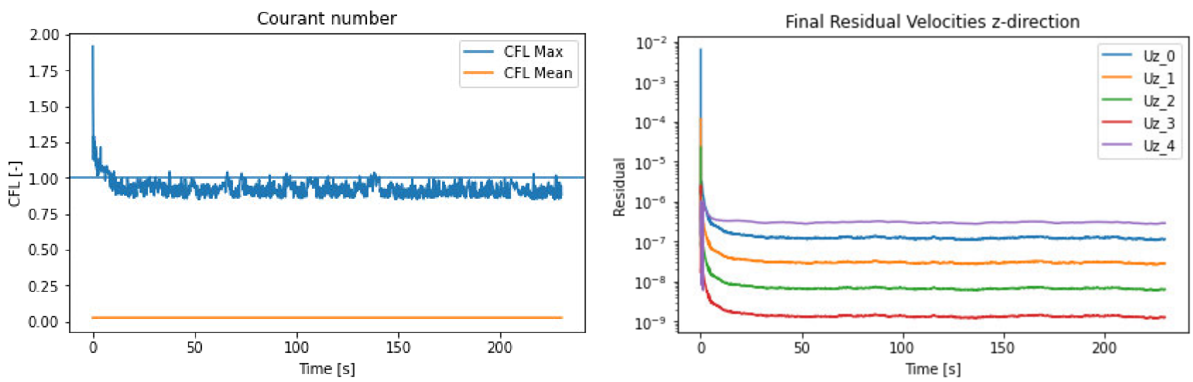

(a) (b)

Figure J.13: Courant number (a) and final residuals velocities in Z-direction (b) for hoisting the DSM system at 2 m/s.

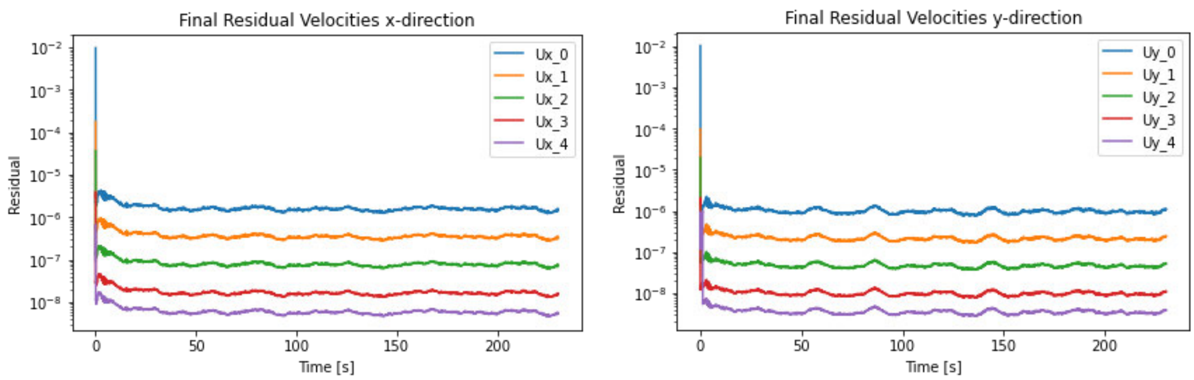

(a) (b)

Figure J.14: Final residuals velocities in X-direction (a) and Y-direction (b) for hoisting the DSM system at 2 m/s.

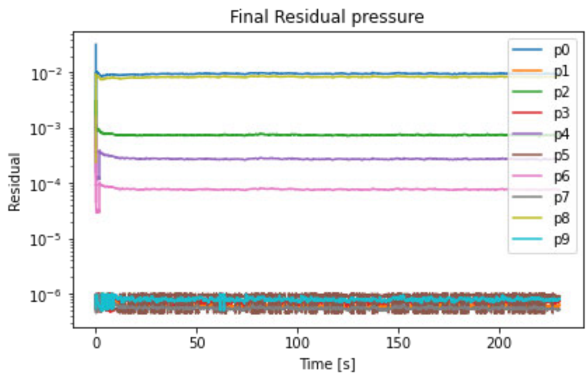

(a)

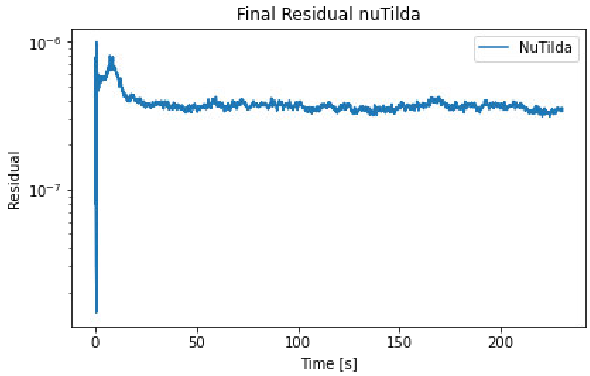

(b)

Figure J.15: Final residuals pressure (a) and nuTilda (b) for hoisting the DSM system at 2 m/s.

J.6. DSM 0.2 m/s lowering at model scale

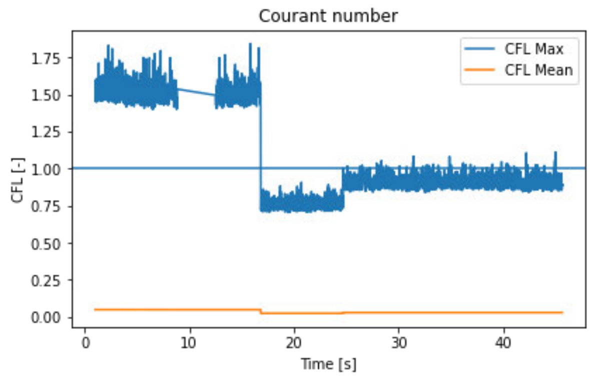

(a)

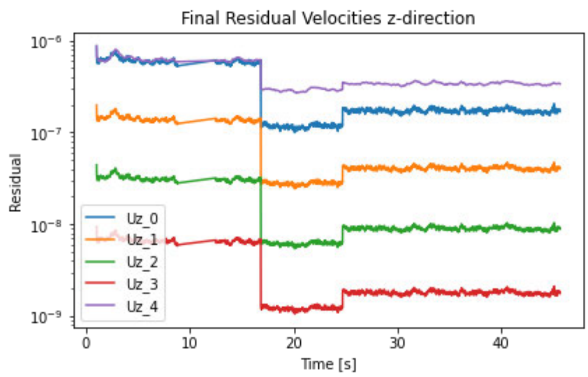

(b)

Figure J.16: Courant number (a) and final residuals velocities in Z-direction (b) for lowering the DSM system at model scale at 0.2 m/s.

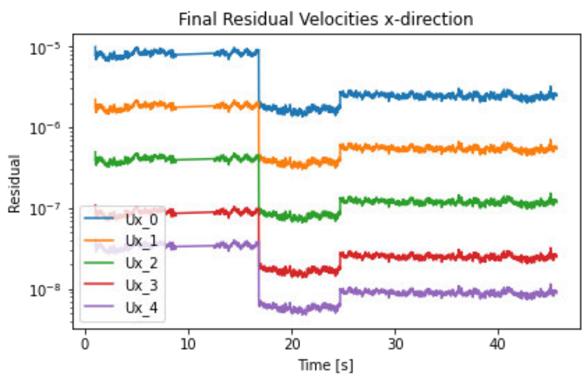

(a)

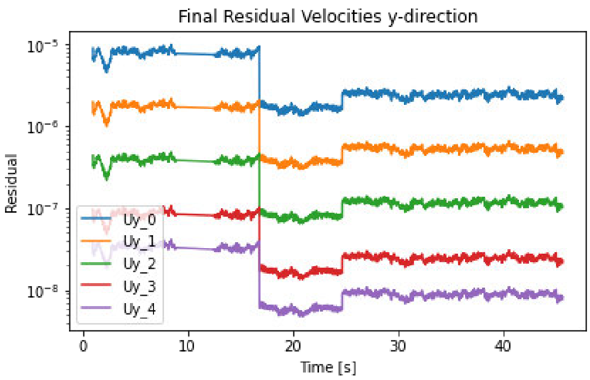

(b)

Figure J.17: Final residuals velocities in X-direction (a) and Y-direction (b) for lowering the DSM system at model scale at 0.2 m/s.

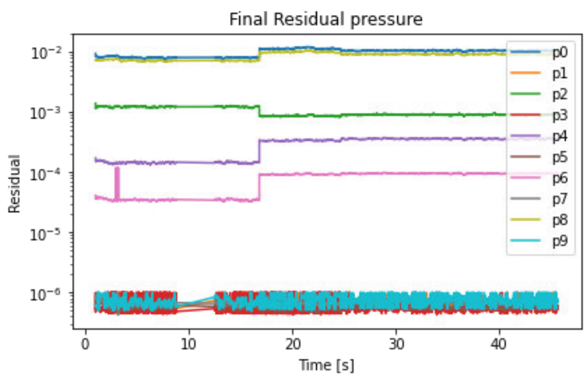

(a)

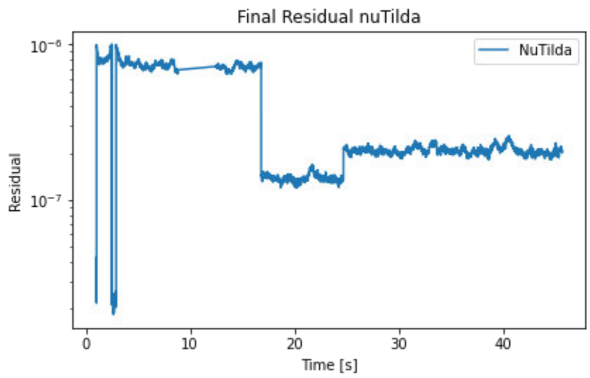

(b)

Figure J.18: Final residuals pressure (a) and nuTilda (b) for lowering the DSM system at model scale at 0.2 m/s.

TU Delft Boskalis